A Search for Extra Neutral Gauge Boson in the Dielectron Channel with the DØ Detector in $p\bar{p}$ Collisions at $\sqrt{s} = 1.96$ TeV

by

Mingcheng Gao

Submitted in partial fulfillment of the

requirements for the degree

of Doctor of Philosophy

in the Graduate School of Arts and Sciences

COLUMBIA UNIVERSITY

2003

ABSTRACT

A Search for Extra Neutral Gauge Boson

in the Dielectron Channel with the DØ Detector

in $p\bar{p}$ Collisions at $\sqrt{s} = 1.96$ TeV

Mingcheng Gao

We have searched for evidence of a new particle, known as the extra neutral gauge boson (Z'), using data collected with the DØ detector in the Tevatron $p\bar{p}$ collisions at $\sqrt{s} = 1.96$ TeV during 2002-2003. In the absence of a Z' signal, we set a 95% confidence level upper limit on the production cross section times the branching ratio of Z' decaying into dielectrons as a function of Z' mass. We exclude the existence of a Z' of mass less than 719 GeV/c^2 at the 95% confidence level, assuming standard model couplings to quarks and leptons.

Contents

List of Figures

List of Tables

Acknowledgements

The data collected at the DØ experiment are the product of the efforts of hundreds of people, and I would like to thank all my colleagues whose contributions made the experiment a success.

I would specially thank my advisor, Mike Tuts, who has showed me the way to high energy physics and has been providing constant support throughout these years. The skills and knowledge that I have learned from him will continue to benefit me a lot in my future.

A lot of colleagues have made direct contributions to this analysis. I would like to thank Tom Diehl, Marco Verzocchi, Georg Steinbrueck, Greg Landsberg and Gustaaf Brooijmans for their careful directions and their effective organization on preparing analysis tools as well as data sample. I would like to thank members of the Editorial Board, Stefan Soldner-Rembold, Ursula Bassler and Gregorio Bernardi, whose critical suggestions contributed immensely to the accuracy of this analysis. I would also thank Steve Muanza for helping me on using PYTHIA and Junjie Zhu for sharing his code with me.

As a member of the calorimeter group, I have spent countless happy hours with the DØ detector. I would like to thank project manager Mike Tuts, "super expert" Dean Schamberger, Leslie Groer, Nirmalya Parua and Shaohua Fu, for having taught me so much in detector hardware and for working shoulder to shoulder for the past four years. I am also sincerely grateful to John Womersley and Tom Diehl for their kind and numerous helps with my academic career.

Finally, I would like to thank Fu, who has helped me significantly by cross-checking results, debugging codes and doing editorial work. Her efforts have made this analysis come into shape sooner.

To my parents ...

Chapter 1

Introduction

Elementary-particle Physics is the study of the basic nature of matter, of force, of time and of space. We seek to discover the simplest constituents of matter, which are called elementary particles, and we seek to understand the basic forces that operate between them. Above all, we seek the unifying laws that will give us a rational and predictive picture of the world around us.

1.1 A Revolution in Particle Physics

The belief in fundamental particles dates back to 5^{th} century BC, when the Greek philosopher Democritus proposed that everything on earth was composed of small invisible entities — atoms. Throughout human history, mankind has tried to explain the world as made up of some basic kinds of matter. The classical Greeks believed in four elements: earth, air, fire and water. In subsequent centuries, alchemists and philosophers added aether, mercury, sulfur, salt, and so on. After Mendeleev published the periodic table of elements in 1872, the basic types of matter were thought to be the almost 100 different chemical elements [1].

Sixty years ago, ordinary matter was proved to consist of protons, neutrons and electrons. Experiments were under way to probe the sub-structures of these particles and the forces between them. Better detectors were designed and more powerful accelerators such as the alternating gradient synchrotron were widely used. During decades of experiments, physicists not only discovered numbers of new particles, but also successfully classified them. For example, the *positron* is a "positively-charged" electron and belongs to the antiparticle family predicted by Relativistic Quantum Mechanics. *Muons* and *neutrinos* are electron-like structureless particles, called *leptons*. There are more than a hundred *hadrons*, such as π^o, K^+, Λ, etc, which are produced by the *strong* force (the same one that holds the nucleus together) and decay by the *weak* force (the one that accounts for beta decay). It became clear that the proton, the neutron and the other hadrons are composite systems made up of much smaller particles called *quarks*. Leptons and quarks are thought to be elementary particles.

On the theory side, four basic interactions (i.e. the strong, weak, electromagnetic and gravitational force) were established. A unified theory of the weak and

Time	Event
1897	Electron was discovered by Thomson, implying an inner structure of atoms.
1905	Einstein's theory of relativity brought us a new understanding of time and space.
1911	Rutherford's atom model: a "positively-charge" nucleus and electrons orbiting around it.
1913	Bohr devised the first successful quantitative model for atomic structure.
1928	Dirac introduced relativistic quantum mechanics and predicted antimatter.
1932	Anderson discovered the positron, the long-awaited antiparticle of electron.
1934	Enrico Fermi proclaimed the existence of the weak force.
1937	The muon was discovered. Its behavior is identical to electron's but it is 200 times heavier.
1948	Quantum electrodynamics (QED) was developed by Feynman, Schwinger and Tomonaga.
1955	The neutrino was discovered.
1961	SU(3) group and the eight-fold way was proposed by Gell-Mann and Ne'eman.
1964	Gell-Mann and Zweig came up with Quark Model. Up, down and strange quarks were named.
1965	Quarks carried a new type of charge: color (red, green and blue).
1967	Weinberg, Glashow and Salam developed unified electroweak theory.
1970s	In early 1970s, Quantum Chromodynamics (QCD) was developed to describe the strong interactions.
1974	The discovery of J/ψ particle proved the existence of a fourth quark: the charm quark.
1975	A "superheavy" electron, the tau, was discovered.
1977	The bottom quark was discovered at Fermilab.
1983	Gauge bosons (W, Z) are discovered at CERN.
1995	Top quark was discovered by Dzero and CDF at Fermilab.
1998	The Super-Kamiokande collaboration found evidence of non-zero neutrino mass.
2000	Fermilab reported the first direct observation of tau neutrino.

Table 1.1: *An Annotated Chronology of Particle Physics.*

electromagnetic forces now exists. *Quantum Chromodynamics* (QCD), which is analogous to *Quantum Electrodynamics* (QED), was developed in the early 1970s and successfully described the strong interactions. Except for the gravitational force, the strong, weak and electromagnetic interactions are now well described by similar mathematical theories called *gauge theories*. The collection of these theories is called the *Standard Model*.

An annotated chronology of modern particle physics is given in Table 1.1 [2].

1.2 Motivation for this Research

Although experimental results so far agree well with predictions of the Standard Model, it is widely felt to be incomplete. For example, gravitation is left outside the framework; strong and electroweak interactions are not unified; it does not tell us what determines the basic properties of quarks and leptons, such as their masses. Moreover, it has a serious problem known as the “hierarchy” problem. For these reasons, physicists have been motivated to search for physics beyond the Standard Model.

Many prospective theories beyond the Standard Model predict an extra neutral gauge boson, denoted by Z'. The discovery of such a particle would provide a direct test of the Standard Model and an important probe of underlying physics at much higher mass scales. In this dissertation, we present the results of a direct-search for the Z' in the di-electron channel through $p\bar{p}$ collisions ($p\bar{p} \rightarrow Z' \rightarrow e^+e^-$) at a center-of-mass energy of $\sqrt{s}$ =1.96 TeV. The data were collected with the upgraded DØ detector during 2002-2003 using the upgraded Tevatron Collider at the Fermi National Accelerator Laboratory in Batavia, IL.

Chapter 2

The Standard Model and Beyond

2.1 Elementary Particles and Forces

According to the Standard Model (SM), there are three families of fundamental particles that interact via four basic forces. The Standard Model successfully describes three of the four forces of nature: the electromagnetic, the weak, and the strong force. The gravitational force is not incorporated into the SM. The fundamental particles are the quarks, leptons and the force-carrying particles (gauge bosons). The leptons and quarks are both spin 1/2 fermions, which must obey Fermi-Dirac statistics [1]. Gauge bosons have spin 1 and obey Bose-Einstein statis-

[1]Fermi-Dirac statistics require that no two particles within a given system be in the same state, e.g. have the same energy and quantum numbers.

tics [2]. For each particle, there also exists an anti-particle[3] with the same mass and spin, but with opposite values for some other properties, such as electric charge. All matter is constructed from leptons and quarks, which interact via the exchange of gauge bosons [3].

There are six flavors of leptons: the electron (e), the muon (μ), the tau (τ), and their corresponding neutrinos (ν_e, ν_μ and ν_τ). The leptons are grouped into 3 generations (e, ν_e), (μ, ν_μ) and (τ, ν_τ). Each generation has similar properties, except that the masses increase with each successive generation. The charged leptons interact via the electromagnetic and weak forces, while the uncharged neutrinos interact only via the weak force. Experimentally, the masses of the neutrinos are constrained to be quite small, and the SM assumes that they are massless. Table 2.1 shows the properties of the leptons [4].

There are also six flavors of quarks: up (u), down (d), charm (c), strange (s), top (t) and bottom (b). Unlike the leptons, they possess fractional electric charge — either -1/3e or +2/3e, where e is the charge of the electron. In addition, quarks also possess an internal degree of freedom called *color*, which can take on three possible values: red, blue and green. In strong interactions, colors play a role similar to the role of the electric charge in electromagnetic interactions. Quarks interact via the strong force as well as the electromagnetic and weak forces.

[2] Bosons can be brought together without restriction, i.e. they can occupy the same state.
[3] Some particles are their own anti-particles.

The quarks are also grouped into three generations (u, d), (c, s), and (t, b), with each generation having similar properties, except that the masses of the quarks increase with each successive generation. Table 2.1 also shows the properties of the quarks [4]. The gauge bosons are the mediators of the forces between different

Generation	Leptons (spin=1/2)			Quarks (spin=1/2)		
	Flavors	Charge ($\|e\|$)	Mass (GeV/c^2)	Flavors	Charge ($\|e\|$)	Mass[4] (GeV/c^2)
1	ν_e	0	$< 3 \times 10^{-9}$	u	$+2/3$	$1 - 5 \times 10^{-3}$
	e	-1	5.11×10^{-4}	d	$-1/3$	$3 - 9 \times 10^{-3}$
2	ν_μ	0	$< 1.9 \times 10^{-4}$	c	$+2/3$	$1.15 - 1.35$
	μ	-1	0.106	s	$-1/3$	$0.075 - 0.175$
3	ν_τ	0	< 0.018	t	$+2/3$	$174.3^{+5.1}_{-5.1}$ or $168.2^{+9.6}_{-7.4}$
	τ	-1	1.78	b	$-1/3$	$4.0 - 4.4$

Table 2.1: *Fermions in the Standard Model.*

particles. The Standard Model treats each interaction as a field and interprets the excitations in the field as particles. An interaction between two particles is viewed as a process in which these two particles exchange a virtual gauge boson. The main properties [4] of the forces and their force-carriers are summarized in Table 2.2 .

The electromagnetic force is an interaction between particles having electric charge. It has an infinite range and is responsible for the attraction between elec-

[4]Due to *quark confinement* (Section 2.2), free quarks are not to be found in nature; hence, their masses cannot be determined precisely. The measurements depend on the energy probes used and the hadronic systems that the quarks are in. The two masses of the top quark are measured through the direct observation of top events and through the Standard Model electroweak fit respectively.

Type of Force	Gravity	Electromagnetic	Weak	Strong
Gauge bosons	Graviton	Photon(γ)	$W^{\pm}, Z$	gluon(g)
Mass (GeV/c^2)	0	0	$W^{\pm} = 80.4$ $Z = 91.2$	0
Acts on	all	electrically charged particles	leptons, quarks	quarks, gluons
Relative Strength	10^{-38}	1/137	10^{-5}	1
Range	∞	∞	$< 10^{-18}\ m$	$< 10^{-15}\ m$

Table 2.2: *The four basic forces and their force-carrying particles.*

trons and the atomic nuclei. It is mediated by the photon (γ), and is described by Quantum Electrodynamics (QED). Any two charged particles interact by coupling to the photon.

The weak interaction has a very short range and exists between any of the leptons and quarks. It is responsible for things like radioactive β decays. It is mediated by the $W^{\pm}$ and Z bosons. In the Standard Model, electromagnetic and weak interactions have been unified in the Glashow-Salam-Weinberg (GSW) model, known as Electroweak theory.

The strong interaction is a short-range force that affects particles carrying color charge. It is responsible for binding quarks together and building nucleons and mesons. It is mediated by gluons and is described by Quantum Chromodynamics (QCD). There are a total of eight gluons, which couple to particles possessing color charge (these particles are the quarks and the gluons themselves).

2.2 Electroweak Theory and QCD

The Standard Model is a *Quantum Field Theory* based on the idea of local gauge invariance [5]. The gauge symmetry group of the SM is

$$SU(3)_C \times SU(2)_L \times U(1)_Y$$

where "C" refers to the color charge, "L" to the weak isospin and "Y" to the weak hypercharge. SU$(3)_C$ is the symmetry group of the strong interactions, and SU$(2)_L\times$U$(1)_Y$ is the symmetry group describing the unified weak and electromagnetic interactions. SU$(2)_L$ symmetry group corresponds to the weak interactions. At low energy ($< 250GeV$) the SU$(2)_L\times$U$(1)_Y$ symmetry is broken into the U$(1)_{em}$ group which corresponds to electromagnetic (EM) interactions.

EM interactions are described by Quantum Electrodynamics (QED) [6]. In QED, the free-particle Lagrangian is invariant under a U(1) rotation of the field operators, which can be related to the conservation of charge. The negative energy states are interpreted as anti-particles. In particular, local gauge invariance requires that the force act through the exchange of an appropriate gauge boson, the photon. This requirement also applies to weak and strong interactions, where the relevant gauge bosons are $W^{\pm}$, Z and gluons respectively.

While the weak and EM interactions appear unrelated at low energies, they become unified at higher energy scales (i.e. $q^2 \approx M_W^2$, where q is the momentum transfer of the interaction). The Glashow-Salam-Weinberg (GSW) theory [7] is based on the symmetry group $\mathrm{SU}(2)_L \times \mathrm{U}(1)_Y$. The fundamental vector bosons of the group are massless isovector triplets W_μ^i ($i = 1, 2, 3$) for the $\mathrm{SU}(2)_L$ group and a massless isosinglet B_μ for the $\mathrm{U}(1)_Y$ group. The Higgs mechanism (*spontaneous symmetry breaking*) is used to break the symmetry of the group at low energies and to give mass to the vector bosons. Two of the W_μ^i acquires a mass and become the $W^\pm$; one linear combination of W_μ^3 and B_μ becomes the Z, while another becomes the photon. This mechanism requires the introduction of a new particle into the Standard Model — the Higgs boson (H). The Higgs is an isospin doublet of scalar mesons that generates the particle masses as a result of self-interaction. If the SM is correct, the Higgs should appear as a real particle. To date, however, the Higgs boson has not been observed.

Quantum Chromodynamics (QCD) [8] is based on the $\mathrm{SU}(3)_C$ symmetry group, where the symmetry is based on the three quark colors (hence the ‘chromo’ in the name of the theory). Local gauge invariance for this symmetry requires eight gauge bosons, i.e. gluons. In QCD, the color symmetry is not broken, so the gluons remain massless. The main feature that differentiates QCD from the electroweak theory is that gluons themselves are colored objects, and participate in the strong force. Due to this gluon-gluon interaction, the strong force increases with distance. As two quarks move apart from each other, the increasing force will either bind the quarks together, or lead to the creation of quark-antiquark pairs, which results in two separate hadrons. This implies that physical particles must be color singlets (i.e. no overall color). This explains the absence of free quarks (*quark confinement*), as well as the structure of hadrons: mesons are made of a quark-antiquark color-anticolor pair; baryons are made up of three quarks, one of each color. The gluon-gluon interaction also results in a running strong coupling constant, i.e. the coupling strength is dependent on the distance between the interacting particles. At relative large distances, the strength is large; at very short distances (less than the size of a proton) the strength is quite small and quarks behave like free particles (*asymptotic freedom*).

2.3 Beyond the Standard Model

The Standard Model (SM) has been enormously successful in explaining a wide variety of Physics from microscopic phenomena to the early universe. At present, aside from a few two or three standard deviation effects, the SM is in good agreement with the experimental data. However, it is far from the ultimate theory of fundamental particles and their interactions that we are seeking.

First, it is incomplete. Gravitation, the most important force in the macroscopic world, is not included in the Standard Model. No one has yet succeeded in developing an experimentally verifiable theory of quantum gravity. The strong and electroweak interactions cannot be unified under its framework. It is natural to suppose that in the ultimate fundamental theory, all four basic interactions are in fact different manifestations of one underlying force.

Second, it is not satisfactory. Many parameters in the Standard Model, mostly masses and weak mixing decay angles, are not predicted but must be determined by experiment. There are many features that are not explained in the SM, such as why there are generations and only three generations, why charge is quantized, etc. The introduction of Higgs mechanism also seems *ad hoc*, and the existence of Higgs has not been confirmed yet.

Finally, there exists the so-called *hierarchy problem*, which arises from the huge differences in the energy scales of the various interactions: the QCD scale is of order 1 GeV ($\sim M_{Meson}$); the electroweak scale is of 100 GeV ($\sim M_{W,Z}$); the scale of grand unification (GUT) is around 10^{16} GeV (when $GM_{GUT}^2/\hbar c \sim 1$); while the "Plank mass" scale is about 10^{19} GeV ($M_{Plank} = \sqrt{\hbar c}/G$). The Higgs mechanism also brings another problem, known as the *fine-tuning* problem. The Higgs mass is quadratically divergent: $m_H^2 = m_0^2 + \delta m_H^2 \approx m_0^2 - g^2\Lambda^2$ to lowest order in perturbation theory, where m_0 is the "bare" Higgs mass, g is a dimensionless coupling constant and Λ is the energy scale. Most recent bounds [9] on m_H are on the order of the electroweak scale (10^2 GeV). If $g^2 \approx 1$ and Λ is around the

GUT or Plank scale (10^{16} GeV or 10^{19} GeV), then m_0 must be adjusted so that $m_0^2 - g^2\Lambda^2 \approx m_H^2$. This requires a precise adjustment of the SM parameters to 23 decimal places.

To overcome the above difficulties, many new theories have been developed beyond the Standard Model , such as *Grand Unified Theories* (GUTs), *Supersymmetric Theories* (SUSY), *String Theory*, *Left-Right Symmetric Model*, etc. The existence of extra neutral gauge bosons (Z') is predicted by some of these prospective theories. We will briefly review them in the next chapter.

Chapter 3

Z' Models and Phenomenology

One of the simplest extensions to the Standard Model (SM) is the existence of extra neutral Z' bosons associated with extra $U(1)$ gauge symmetries. They arise in extended gauge theories including Grand Unified theories, Superstring theories, and Left-Right Symmetric models, etc.

3.1 Models of Extra Gauge Bosons

Although in most extended gauge theories, the symmetry-breaking scale is at such a high energy that the associated extra bosons are beyond the reach of present and planned colliders [10], many models allow light ($\sim$ TeV) Z' bosons that are detectable at current experiments. We will briefly review these Z' models here. More details can be found in the original references provided.

Left-Right Symmetric Model

One of the earliest of these extensions was the addition of a right-handed gauge group to the electroweak sector giving $SU(2)_R \times SU(2)_L \times U(1)_{B-L}$. This is referred to as the *Left-Right Symmetric Model* (LRM) [11]. In the Standard Model, the W and Z only interact with "left-handed" quarks and leptons, but not with "right-handed" quarks and leptons. However, interactions of gluons and photons do not contain any handedness bias. This suggests that a right-handed version of the weak interactions might exist. In effect, the LRM model restores parity or mirror symmetry at higher energy. One of the attractive features of this model is that once right-handed neutrinos are stipulated in $SU(2)_R$, the generator of $U(1)$ becomes B-L, baryon minus lepton number, which is a physical observable. A second attractive feature of the left-right model is that the theory would naturally accommodate a small mass for left-handed neutrinos. The Z' of this model is often denoted as Z_{LRM}.

Grand Unification

The largest set of extended gauge theories are those based on *Grand Unified Theories* (GUTs) [12]. GUTs propose a single interaction to describe the electromagnetic, weak and strong interactions which have a single coupling at some unification scale ($M_{GUT} \sim 10^{16}$ GeV). They postulate a new spontaneous symmetry breaking analogous to the one already present in electroweak theory to account for the different couplings seen in nature (at a much lower energy scale). The simplest of GUTs is based on the $SU(5)$ symmetry group which incorporates the $SU(3)$, $SU(2)$ and $U(1)$ symmetry groups within it. However, the $SU(5)$ group has been ruled out because it predicts that protons will decay with a half-life which has been excluded by experiment. Other popular examples of GUTs are the $SO(10)$ and E_6 groups.

The $SO(10)$ GUT contains an extra $U(1)$ as can be seen from its maximal subgroup: $SO(10) \to SU(5) \times U(1)_\chi$. Similarly, the E_6 GUT contains the subgroup: $E_6 \to SO(10) \times U(1)_\psi$. Their corresponding neutral gauge bosons are denoted as Z_χ and Z_ψ [13].

Superstring Theory

Superstring Theory [14] is a supersymmetric version of String Theory.

Supersymmetric Theories (SUSY) [15] postulate a relation between the bosons and fermions in the Standard Model. Each SM particle has a superpartner (called a *sparticle*) with a spin differing by $\frac{1}{2}\hbar$, but with all other quantum numbers remaining the same. Thus the SM bosons have fermion superpartners and the SM fermions have boson superpartners. One important feature of the existence of superpartners is that they cancel the quadratic divergences in the masses of the

SM particles, thus yielding finite results to calculations without fine-tuning.

String Theory [16] is the only current theory that can incorporate gravity. It describes all matter particles as one dimensional strings, rather than the zero dimensional points of field theory. Strings can generate all types of fundamental particles found in nature including the graviton, the mediator of the gravitational force. It also predicts an additional six or seven dimensions beyond the four observed space-time dimensions. Such extra dimensions could exist if, for example, they are curled in on themselves, rather than extending linearly in the manner of the familiar dimensions.

E_6 is the simplest unifying group compatible with Superstring Theory. The linear combination $\sqrt{3/8}Z_\chi - \sqrt{5/8}Z_\psi$ corresponds to the extra Z' arising in some superstring models [17], and is denoted as Z_η.

"Sequential" Standard Model

In this model, the extra gauge boson Z'_{SM} is assumed to have the same couplings to quarks and leptons as the Standard Model Z boson, and decay only to three known families of fermions. There is no theoretical model for a Z' of this type since it is not a gauge invariant model. This model is traditionally used in experiments and for purposes of comparison [17].

The Z' decay width is set equal to the width of the SM Z boson scaled by a factor of $M_{Z'}/M_Z$ as in previous searches [18]-[22]. For $M_{Z'} > 350$ GeV, decay channels involving the top quark, unavailable for the SM Z boson, are now open.

There are a number of other models that predict extra gauge bosons, such as Alternative Left-Right Model (ALRM) [23], un-unified Standard Model (UN-SM) [24], the BESS model [25] and models of Composite Gauge Bosons [26]. But most theoretical and phenomenological interests relate to the models discussed above.

3.2 Previous Z' Searches

Experimental constraints on the existence of a Z' are obtained either indirectly from fits to high precision electroweak data, or from direct searches at operating collider facilities.

Indirect Constraints: Because of the presence of extra gauge groups, the Standard Model Z will mix with the Z' after symmetry breaking. This $Z-Z'$ mixing shifts the values of some observables and parameters expected from the SM. Precise measurements from experiments, such as Z-pole observables, W mass and weak neutral-current parameters, set bounds on these values, which then translate into constraints on the $Z-Z'$ mixing and thus on the Z' mass [27].

Direct-search constraints: High-energy experiments have searched for on-

Z′ models	Mass (95% CL)	Exp/Author	Comments
Z_{SSM} Sequential SM	> 1500 GeV	K. Cheung	precise electroweak
	> 690 GeV	CDF	$p\bar{p}; ee, \mu\mu$ combined
	> 670 GeV	DØ	$p\bar{p}; ee$ channel
Z_{LR} Left-Right Sym. Model	> 860 GeV	K. Cheung	precise electroweak
	> 630 GeV	CDF	$p\bar{p}; ee, \mu\mu$ combined
Z_χ $SO(10) \to SU(5) \times U(1)_\chi$	> 680 GeV	K. Cheung	precise electroweak
	> 595 GeV	CDF	$p\bar{p}; ee, \mu\mu$ combined
Z_ψ $E_6 \to SO(10) \times U(1)_\psi$	> 350 GeV	DELPHI	e^+e^-; Z-Z' mixing
	> 590 GeV	CDF	$p\bar{p}; ee, \mu\mu$ combined
Z_η E_6 models	> 619 GeV	G.Cho	precise electroweak
	> 620 GeV	CDF	$p\bar{p}; ee, \mu\mu$ combined

Table 3.1: *Current mass limits for various Z'.*

shell Z' production and decay. Searches can be classified by the initial state of which the Z' is produced (e.g. hadron colliders, e^+e^- colliders and ep colliders), and the final state into which the Z' decays (e.g. di-electron, di-muon channels).

For a light Z' ($M_{Z'} < M_Z$), direct searches in e^+e^- colliders have ruled out any Z' unless it has extremely weak couplings to leptons. For a heavy Z' ($M_{Z'} \gg M_Z$), the best limits come from $p\bar{p}$ colliders via Drell-Yan production and subsequent decay to charged leptons. CDF quotes limits on $\sigma(p\bar{p} \to Z' + X) \cdot Br(Z' \to \ell^+\ell^-) < 0.04\ pb$ at 95% C.L. for $\ell = e + \mu$ combined [22]. However, if the Z' has suppressed or no couplings to leptons (i.e. *leptophobic*), then these experimental limits will be much weaker.

The present Z' mass limits [28] for the models discussed in Section 3.1 are summarized in Table 3.1.

3.3 This Study

The signal of Z' from $p\bar{p}$ collisions at Tevatron consists of the Drell-Yan production of lepton pairs with high invariant mass via

$$p\bar{p} \longrightarrow Z' \longrightarrow l^+l^- \tag{3.1}$$

where $l = e, \mu$ are often used as the final states. The branching ratio is $\sim 3.2\%$ for each leptonic channel.

Although Z' decays nearly 72% of the time to hadrons, the hadronic decays of Z' are difficult to distinguish from other copious sources of hadronic final states. The dilepton final states have far smaller backgrounds. Thus, although the rate is low, the signal to background ratio is much better.

In this dissertation, we present the direct search for Z' in the dielectron final state: $p\bar{p} \to Z' \to e^+e^-$. After reconstruction of the dielectron invariant mass, the expected Z' signal would be a Breit-Wigner peak (Z' resonance) superimposed on the invariant mass spectrum expected in the Standard Model arising from Z and Drell-Yan production.

The Z' Monte Carlo events in this study are generated based on the "sequential" Standard Model, where the Z' is assumed to have standard model couplings. However, in [20] it was found that the experimentally obtained limits on $(\sigma B)_{Z'}$

is insensitive to the choice of coupling strength and the Z' decay width used in Monte Carlo. Hence, the $(\sigma B)_{Z'}$ limit can be used for purposes of comparison with any realistic Z' models, as long as the width $\Gamma_{Z'}$ is less than $2\Gamma_{Z'_{SM}}$ for $M_{Z'} > 120$ GeV, where $\Gamma_{Z'_{SM}}$ is the width assuming the SM couplings.

Chapter 4

Experimental Apparatus

4.1 Overview

One of the most important elements in a high energy physics experiment is a particle accelerator capable of producing a beam with sufficient energy to create the particles of interest. After a beam of particles has been accelerated to the desired energy, it can be used in: 1. Fixed target mode, in which the beam is directed onto various targets to produce a wide range of secondary particles; 2. Collider mode, in which the circulating beams are strongly focused and then collide at specific interaction points where detectors are built to collect the resultant debris of the collision. The advantage of the collider mode is that much higher

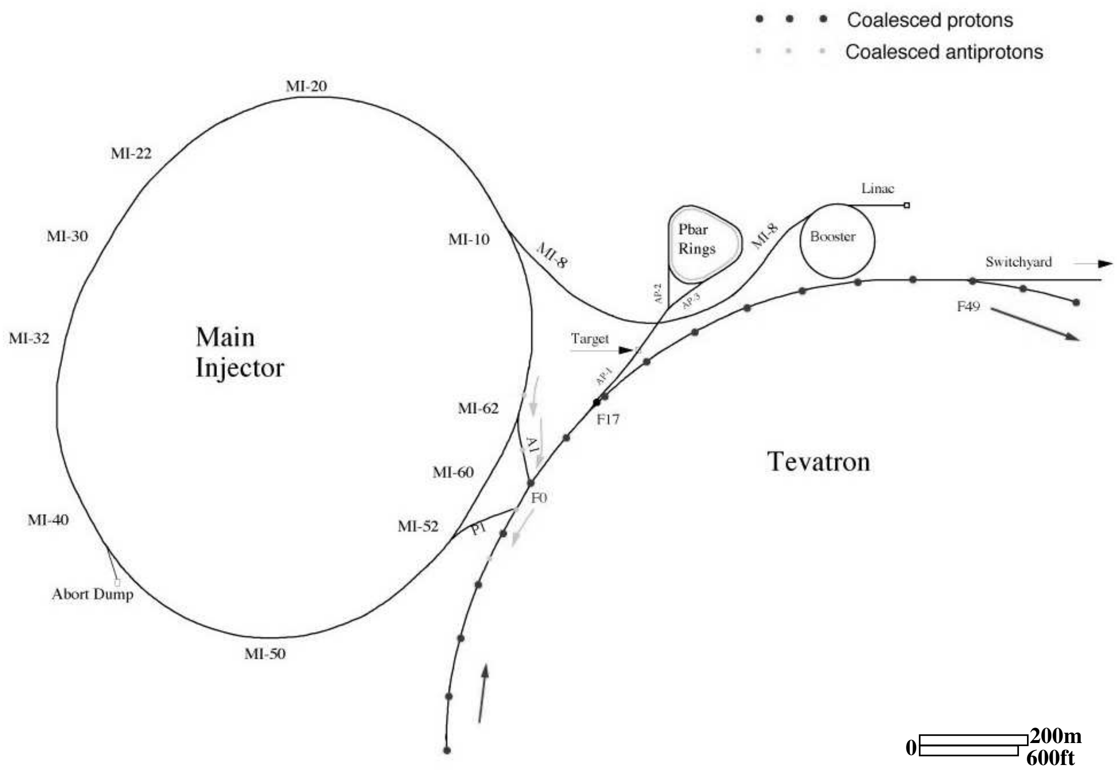

Figure 4.1: *Fermilab Tevatron Collider complex.*

center-of-mass energy is available[1].

The Tevatron proton-antiproton Collider (Figure 4.1), located at the Fermi National Accelerator Laboratory (Fermilab) in Batavia IL, is the highest-energy particle collider currently operational anywhere in the world. The first $p\bar{p}$ collisions in the Tevatron occurred in 1985. During Run I (1992-96), the Tevatron operated at a center-of-mass energy of 1.80 TeV and delivered an integrated luminosity of $\sim$140 pb^{-1}. In Run II (2001-), the upgraded Tevatron has increased the center-of-

[1] In a collision, the really "useful" part of the beam energy E is the center-of-mass energy, which is proportional to $\sqrt{E}$ in fixed target mode and proportional to E in collider mode.

mass energy to 1.96 TeV, which provides an effective increase in cross section for many physics processes. The major upgrades include the construction of a new accelerator, the Main Injector, and a new antiproton storage ring, the Recycler, within a common tunnel [2]. The upgraded Tevatron is designed to provide 10-100 times more luminosity.

There are now two collider detectors at Tevatron Collider: the DØ detector and the Collider Detector at Fermilab (CDF). Both detectors have also undergone comprehensive upgrades for Run II.

4.2 The Tevatron Collider

A schematic view of various accelerators used to produce the final colliding beams are shown in Figure 4.2. A detailed description of the Tevatron can be found in [29].

The origin of the beam is in a bottle of pressurized hydrogen gas. The hydrogen atoms are ionized by the addition of electrons, forming H^- ions. These H^- ions are accelerated to an energy of 750 keV by an electrostatic Cockroft-Walton accelerator. Once at 750 keV, the ions are injected into the Linac. The Linac is a 150 m long linear accelerator, which raises the energy of the ions to 400 MeV.

[2] One advantage of $p\bar{p}$ collider is that the same system can be used to accelerate both types simultaneously since proton and antiproton have same mass but opposite charge.

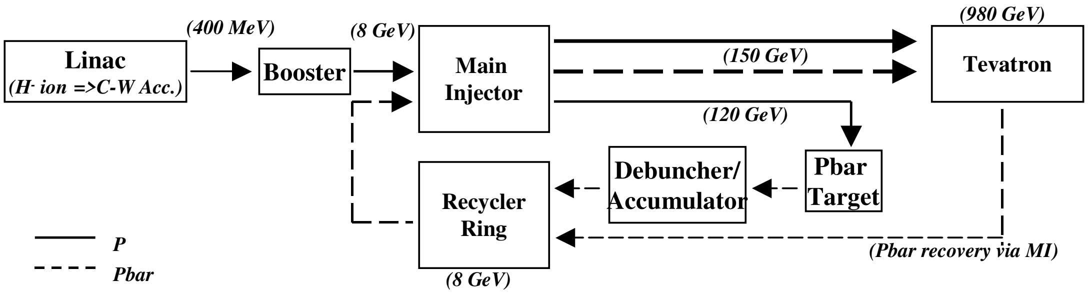

Figure 4.2: *A schematic view of the Tevatron operation.*

Once the ions emerge from the Linac, they pass through a carbon foil which strips off the electrons, thus creating protons. The protons are then steered into the Booster, a 151 m diameter synchrotron. Operating with a cycle time of 15 Hz, the Booster raises the energy of the protons to 8 GeV. Protons are then delivered from the Booster to the Main Injector in a batch of 84 bunches with an intensity of 5-6 $\times 10^{10}$ protons per bunch.

The Fermilab Main Injector (FMI) is a large aperture, rapid cycling, proton synchrotron. The FMI is seven times the circumference of the Booster and slightly more than half the circumference of the Tevatron. When the Tevatron is in collider mode, the FMI has four major operating modes[3]:

1) *Antiproton Production.* A single Booster batch containing 5×10^{12} protons is injected into the FMI at 8 GeV. These protons are accelerated to 120 GeV and extracted in a single turn for delivery to the antiproton production target.

[3]In fixed target mode, FMI also provides highly intensive proton beams at 120 GeV (MI Fixed target) and at 150 GeV (Tevatron fixed target).

2) *Collider Proton preparation.* Coalesces and accelerates 5-11 bunches of protons delivered from the Booster into one coalesced bunch at 150 GeV in the Tevatron. A total of 36 coalesced bunches are required for normal operation.

3) *Collider Antiproton preparation.* In one cycle, Coalesces and recaptures four bunches of antiprotons provided by the Recycler at 8 GeV, and accelerates them to 150 GeV, and delivers them to the Tevatron in a direction opposite to that of the proton beam. Nine cycles are required to inject 36 coalesced bunches.

4) *Antiproton Deceleration.* As a part of antiproton recovery, FMI accepts 4 antiproton bunches at 150 GeV from the Tevatron, decelerates them to 8 GeV, and then transfers them to the Recycler. This process is repeated nine times.

The production of antiprotons (called *pbar stacking*) begins when 120 GeV proton bunches are dumped on a nickel/copper target (in the Target Hall) and antiprotons are collected from the resultant debris. These antiprotons vary greatly in their angular divergence and energy spectrum. So they are first focused using a lithium lens; Then, a magnetic field is used to select 8 GeV antiprotons. The production rate is around twenty antiprotons for every million protons that are sent to the Target Hall. Qualified antiprotons are collected and injected into the Debuncher where they are reduced in size by a process known as *stochastic cooling*. This process runs continuously until the next bunch of antiprotons arrives, about 1.5 s (a cycle time) later. At this point, the monochromatic antiproton beam of about 9×10^7 antiprotons is transferred to the Accumulator, where further cooling is applied and their density is further increased. The Debuncher and the Accumulator make up the Antiproton Storage Rings. The stacking rate is about $\sim 10^{11}$ antiprotons per hour. When the antiproton stack is large enough ($\sim 10^{12}$ antiprotons), they are transferred into the Recycler ring.

The Recycler is a fixed 8 GeV kinetic energy storage ring. It is located in the Main Injector tunnel, directly above the Main Injector beamline, near the ceiling. The Recycler can increase the number of antiprotons available for the Tevatron by a factor of at least two, which proportionally increases the luminosity. The first role of the Recycler is to act as a high reliability storage ring for antiprotons. It is able to store and cool as many as 3×10^{12} antiprotons. Its second role is to act like a post-Accumulator ring. As the stack size in the Accumulator ring increases, there comes a point when the stacking rate starts to decrease. By emptying the contents of the Accumulator into the Recycler periodically, the Accumulator is always operating in its optimum antiproton intensity regime. The third role of the Recycler (designed but not commissioned yet) is to act as a receptacle for antiprotons left over (about 75%) at the end of the previous Tevatron store. By cooling these antiprotons and re-integrating them into the Recycler stack, the effective stacking rate, and hence the luminosity, is more than doubled. The antiproton recovery goes as follows: first, the Tevatron decelerates antiprotons from

980 GeV to 150 GeV; then, the antiprotons are injected back to the Main Injector where they are decelerated to 8 GeV; and lastly, those recovered antiprotons are transferred to the Recycler stack. During antiproton extraction, four bunches of antiprotons (7×10^{10} per bunch) will be delivered at a time to the Main Injector and then to the Tevatron.

The Tevatron is a synchrotron composed of super-conducting magnets that operate at a temperature of 4.6 K and can produce magnetic fields of approximately 3 Tesla. Currently the Tevatron operates in a "36×36" mode, i.e. with 36 proton bunches and 36 antiproton bunches circulating in opposite directions. Electrostatic separators are used to separate the two beams. Once the Tevatron is loaded with all the bunches, both beams are ramped to the maximum energy of 980 GeV and are also highly focused. At desired interaction points (B0 and D0), the beams are made to collide through the use of quadrapole magnets. The stored luminosity will continually decrease from its initial value as a result of interactions. The beam lifetime of one store is typically 10-20 hours in Run II. The time interval between stores is about a few hours.

Table 4.1 lists some of the Tevatron operation parameters for Run II as well as those for Run I. Figure 4.3 shows the integrated luminosity delivered to DØ and recorded by the DØ detector. The average efficiency is about 73%. The loss is due to problems from detectors and the data acquisition systems during collision.

	Run Ib (1993-1995)	Run IIa (present)	Run IIb (plan)
Bunches	6x6	36x36	140x108
Protons/Bunch	2.3×10^{11}	2.7×10^{11}	—
Antiprotons/Bunch	5.5×10^{10}	7×10^{10}	—
Typical Luminosity ($\times 10^{32} cm^{-2} s^{-1}$)	0.16	0.25 [4]	5.2
Integrated Luminosity (pb^{-1}/week)	3.2	6.0	105
Energy (GeV)	900	980	980
Bunch Spacing (nsec)	3500	396	132
Interactions/Crossing	2.5	2.3	4.8

Table 4.1: *Tevatron operation parameters.*

This efficiency has been improved to 85-90% recently.

4.3 DØ Coordinate System

Before proceeding with a description of the DØ detector, it is necessary to define the coordinate system used in the experiment. DØ uses a right-handed coordinate system with the positive z-axis pointing in the direction of the proton beam, and the positive y-axis being vertical up. The angular coordinates (azimuthal ϕ and polar θ) are defined such as $\phi = 0$ coincides with the $+x$ direction and $\theta = 0$ with $+z$ direction. Radial distances are measured perpendicularly to the beam line. Instead of the angle θ, it is convenient to use the *pseudorapidity*,

[4] The currently achieved luminosity is smaller than the design value ($\sim 10^{32} cm^{-2} s^{-1}$), because the Tevatron (especially the Main Injector and the Recycler) is still under commissioning.

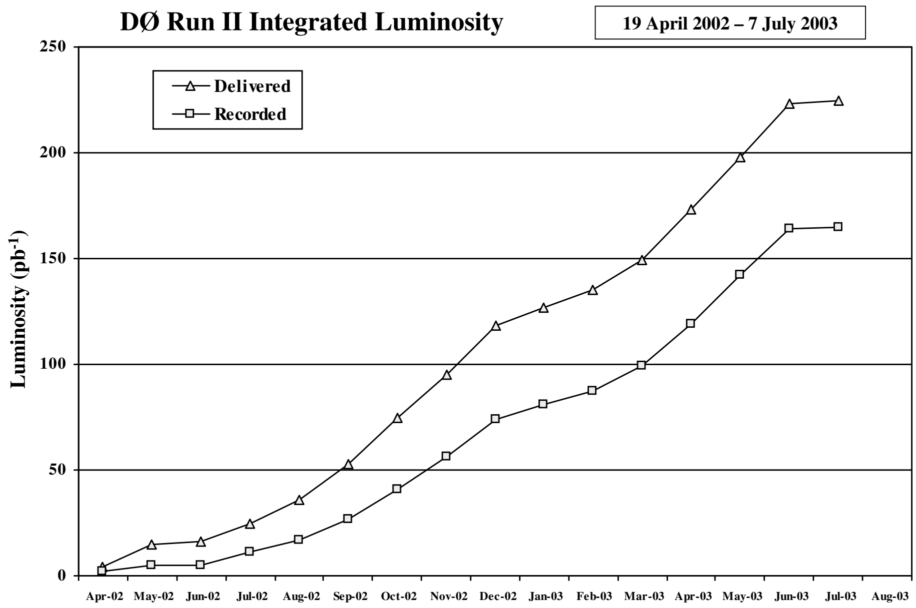

Figure 4.3: *Integrated luminosity delivered to DØ and recorded by the DØ detector.*

η, defined by

$$\eta \equiv -\ln[\tan(\theta/2)] = \tanh^{-1}(\cos\theta) \tag{4.1}$$

The pseudorapidity approximates the true rapidity of a particle,

$$y = \frac{1}{2}\ln(\frac{E+p_z}{E-p_z}) \tag{4.2}$$

in the limit that $m \ll E$, where m is the particle's rest mass. Because the rapidity is invariant under Lorentz transformations, by using the pseudorapidity, the shape of the particle distribution ($dN/d\eta$) is invariant under boosts along the z-axis.

In addition, "detector pseudorapidity", η_{det}, is also used. The η_{det} is computed with respect to an interaction point whose longitudinal position is set to $z = 0$. In reality, this interaction point is distributed around zero (Figure 4.4) thus causing a slight difference between η and η_{det} for any given particle.

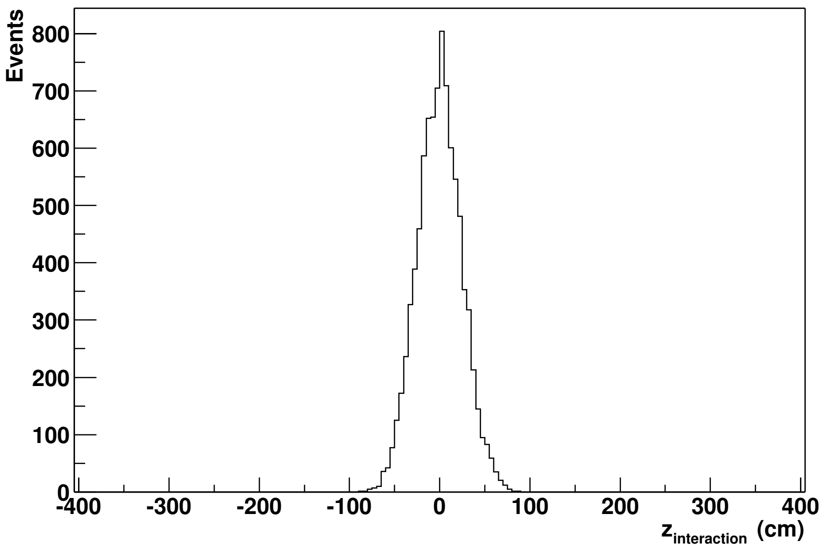

Figure 4.4: *Distribution of the interaction point in z-axis.*

In practice, it is also convenient to project the momentum vector of a particle onto a plane perpendicular to the beam line. This "transverse momentum" $p_T = p \sin\theta$ is useful due to the fact that in a $p\bar{p}$ collision, many products of the collision escape the detection by going down the beam pipe, thus making it impossible to measure the momenta accurately along the direction of the colliding beams. However, one can apply momentum conservation in the transverse plane. Similarly, one defines the "transverse energy" as $E_T = E \sin\theta$.

4.4 The DØ Detector

The DØ detector was first proposed in 1983 and completed in early 1992. It weighs 5500 tons and measures 13 m (height) x 11 m (width) x 17 m (length). Its design was optimized for the study of high p_T physics and high mass states. Based on the data taken in Run I (1992-96), DØ has published more than 120 papers and obtained lots of exciting results, such as the discovery of the top quark. A full description of Run I DØ detector can be found in [30].

Even before the DØ detector began its first data taking run, an upgrade project was proposed in the Fall of 1990 in order to prepare the detector for Run II. There were many new detector challenges to be met: the decrease of the bunch crossing time from 3.5 μs in run I to 396 ns in Run II requires much faster responses from its subsystems; the increasing radiation dosages calls for radiation-hard parts to prevent systems deterioration; large occupancies and event pile-up now become more serious, etc.

4.4.1 Overview of the Run II Upgrade

The upgrade builds on the strengths of DØ, full coverage in calorimetry and muon detection, while enhancing the tracking and triggering capabilities [31]. An overall view of the Run II DØ detector is shown in Figure 4.5 with the three primary detector systems indicated (i.e. central tracking, calorimeter and muon

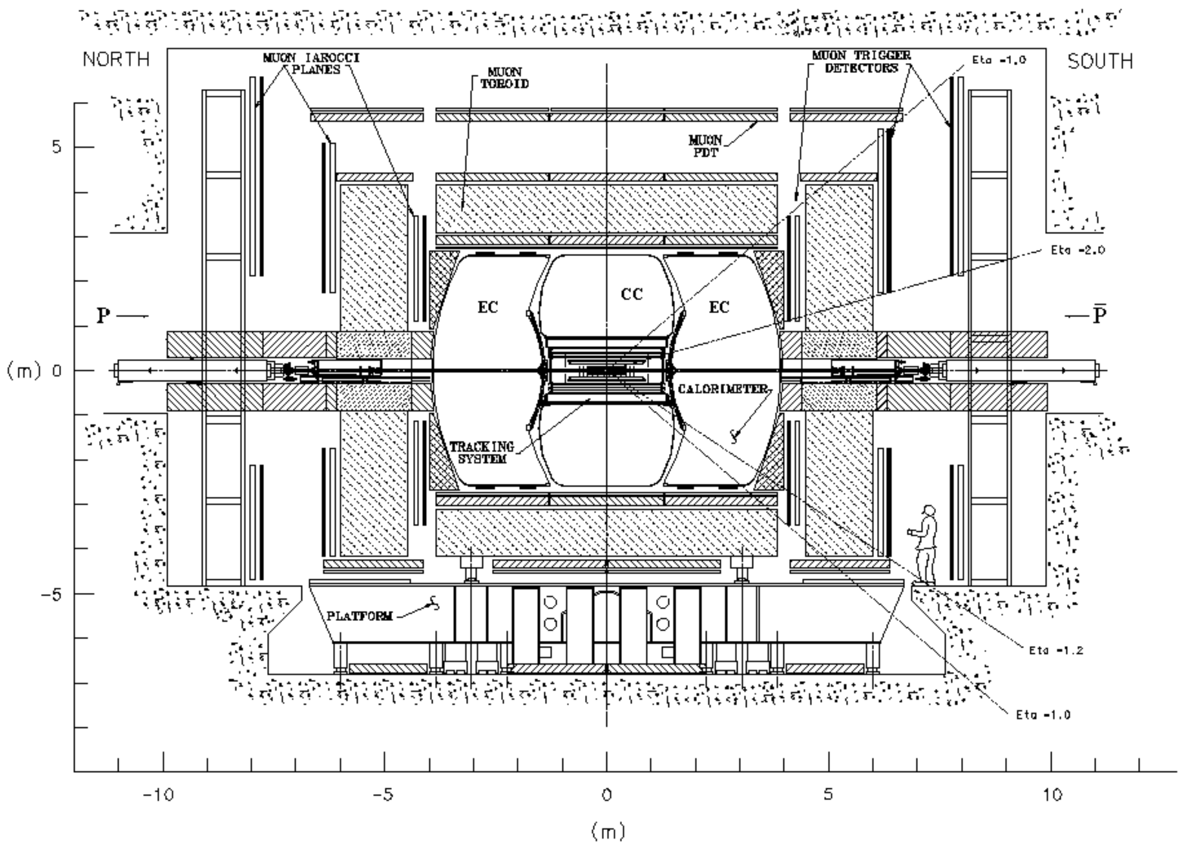

Figure 4.5: *Side view of the DØ upgraded detector in Run II.*

systems).

The calorimeter consists of three parts: the Central Calorimeter (CC) and two Endcap Calorimeters (EC). The upgrade of the calorimeter system is restricted only to its front-end electronics. No changes was made to the calorimeter itself.

A major element of the upgrade is the replacement of the inner tracking systems. The new tracking system consists of an inner silicon vertex detector, surrounded by eight "superlayers" of scintillating fiber tracker. These detectors are located inside a 2 Tesla superconducting solenoid. A scintillator based central preshower detector with wavelength shifter readout is located between the outer radius of the solenoid and the inner radius of the central calorimeter cryostat to provide electron identification and to compensate for energy losses in the solenoid. In the forward region, a preshower detector similar to the central one is installed on the faces of the endcap calorimeter cryostats. The higher event rates in Run II have led us to add new muon trigger detectors covering the full pseudorapidity range and the harsh environment of Run II has prompted us to replace the forward proportional drift tubes with mini-drift tubes. Electronic upgrades are driven by the need to handle a smaller bunch spacing and provide pipelining of the various front-end signals from the tracking, calorimeter, and muon systems. The front-end electronics for all these systems has been replaced. New trigger elements have been added and a new trigger system is used to reduce the raw event rates to a manageable level.

With the upgraded detector, the strengths of DØ are considerably enhanced. For example, b-tagging for top and Higgs events is now available by the use of the silicon detector; the forward-backward charge asymmetry of Z decays can now be studied with the addition of the magnetic field; the upgrades of muon systems and inner tracking systems have improved physics analyses involving muon final states.

In the following sections, we will briefly discuss different subsystems of the Run II detector with emphasis placed on those most relevant to this analysis.

4.4.2 Solenoid

In Run II, a 2 Tesla Superconducting Solenoid magnet [32] was added to the DØ detector in the bore of the CC calorimeter cryostat. Thus, the charge and momentum of a charged particle can be determined from its curvature by the new central tracking system in the bore of the solenoid. Its geometrical size is constrained by the fact that the solenoid, together with the central preshower detector on its outer surface, must fit in the existing inner bore of the CC calorimeter cryostat, while simultaneously preserving the largest possible tracking volume.

The solenoid is a 2.7 m long two-layer coil with a mean radius of 60 cm. The thickness of the coil plus its cryostat has been minimized in order to preserve good electromagnetic resolution (about 0.9 radiation lengths). The uniformity of the magnetic field inside the tracking volume is tested to be within 0.5% .

4.4.3 The Central Tracking system

The tracking system is designed to meet several goals: momentum measurement with the introduction of a magnetic field; good electron identification and e/π rejection; tracking over a large range in η ($\approx \pm 3$); secondary vertex measure-

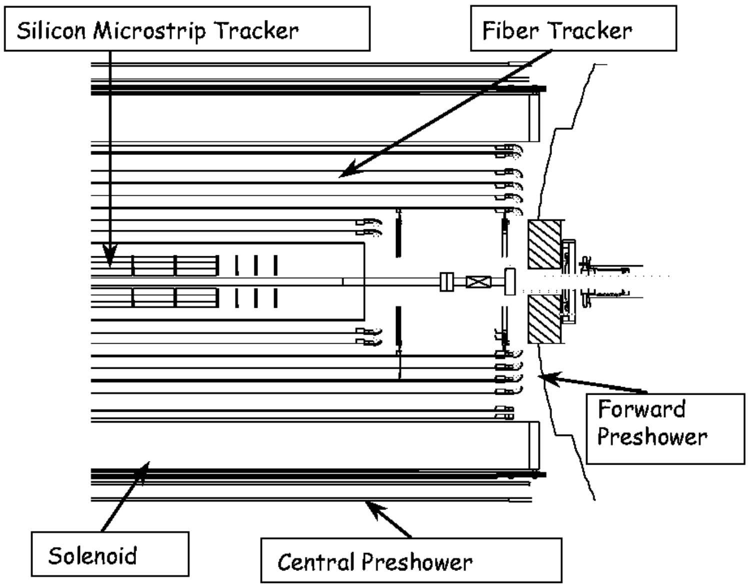

Figure 4.6: *One-half side view of the central tracking system.*

ment for identification of b-jets; hardware tracking trigger; fast detector response; and radiation hardness[5]. It consists of a silicon tracker in the center and a fiber tracker surrounding it, as shown in Figure 4.6.

The Silicon Microstrip Tracker

The Silicon Microstrip Tracker (SMT) [33] is the first set of detectors encountered by particles emerging from the collision. It provides for a 3-dimensional track reconstruction with a resolution of $\sim 10\ \mu m$. Because of the extended luminous region ($\sigma_z \approx 25\ cm$), it is difficult to deploy detectors such that particles traverse

[5]At DØ , detector components are designed to preserve good performance up to radiation doses corresponding to an integrated luminosity of 2-4 fb^{-1}.

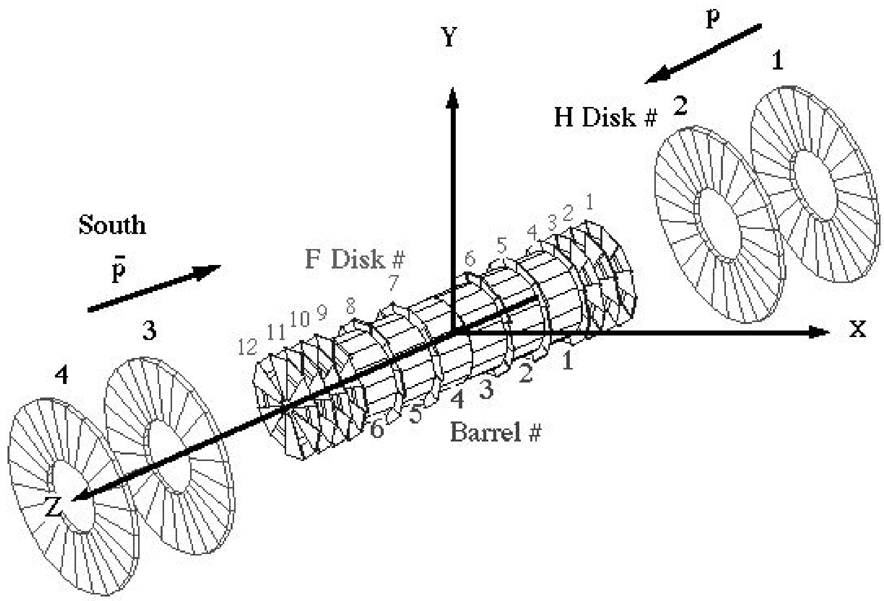

Figure 4.7: *The silicon microstrip tracker.*

them at near normal incidence. This motivated a barrel/disk system design: with the barrel detectors measuring primarily the $r - \phi$ coordinate and disk detectors measuring the $r - z$ as well as the $r - \phi$ coordinate. Therefore, tracks at low rapidity ($|\eta| < 1.5$) are measured in the barrel detectors while tracks at larger rapidity ($1.5 < |\eta| < 3.0$) are measured in the disks.

The SMT consists of six barrel modules with silicon sensors parallel to the beamline, twelve "F-disks" and four sets of "H-disks" with silicon sensors normal to the beamline (Figure 4.7). Each barrel, 12.4 cm in length, contains four concentric layers of silicon ladders with radii ranging from 2.6 cm to 10.0 cm. The four inner barrels include only double-sided ladders with spatial resolution in the range 8-12 μm. The two outer barrels have 50 μm pitch single-sided ladders in layers 1 and 3. The barrel-to-barrel gap is small (about 8 *mm* containing a F disk) in order to maintain a high acceptance for low rapidity tracking. The F-disks, which are interspersed with the barrels, consist of 12 double-sided wedges alternating around a thin cooling channel. There are four large area H-disks, 24 single-sided wedges, mounted at the extreme end of the tracking volume in order to maintain a uniform momentum resolution in the forward region.

The silicon sensors used in the SMT are AC coupled and radiation hard. Each sensor consists of thin silicon wafers implanted with very narrow, closely spaced conducting strips. When an ionizing particle passes through the sensor, electrons will be promoted into the conduction band of the semiconductor material and drawn to these strips by high electric fields. Thus, the strips will undergo a voltage drop proportional to the amount of the original ionization. This drop is read out by the SVX II [6] chips mounted on a so-called high density interconnect (HDI) circuit. The total number of channels in the SMT is about 793k.

Ladders and *wedges*, which are the basic SMT mechanical units in the barrels and in the disks respectively, are formed by putting the sensors and their readout electronics together with 400 μm thick beryllium substrates glued to the 300 μm thick silicon. The layout of a ladder is shown in Figure 4.8. In the wedges, the HDI is at the outer radius. These mechanical units not only provide a precise and

[6] SVX II is a 128-channel silicon strip readout chip including preamplifier, analog pipeline delay and analog to digital converter.

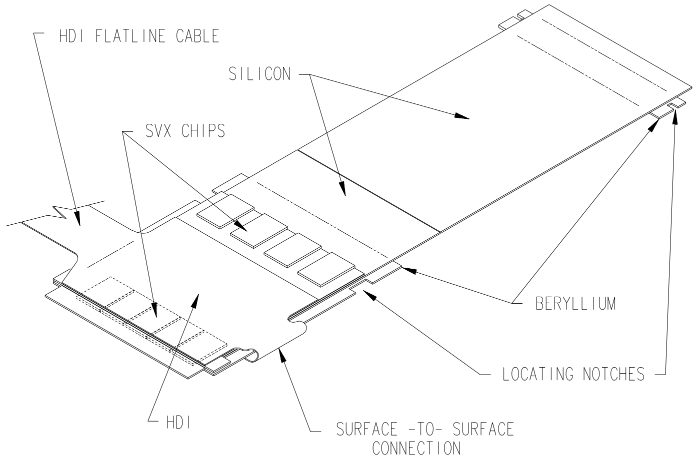

Figure 4.8: *Layout of the ladder.*

stable support, but also provide cooling. The operating temperature is 5-10 °C. During assembly, an accuracy in positioning of better than ± 20 μm was achieved.

The SVX II chips are controlled by a *port card* mounted on the detector platform through two metallic cables. The port card downloads parameters to the chips, interprets their readouts and sends the data over fiber optic cable to the DAQ (Data Acquisition) system as well as to the Level 2 STT (Silicon Track Trigger) system.

The Level 2 STT [34] utilizes information from the SMT barrels to reconstruct tracks with improved spatial and momentum resolutions, which allows the trigger system (Section 4.4.7) to select events from the decay of long-lived particles, such as B hadrons or tau leptons. The STT is presently being commissioned.

The Central Fiber Tracker

The Central Fiber Tracker (CFT) [35] serves two main functions: first, together with the silicon detector, it enables track reconstruction and momentum measurement in the range $|\eta| < 2.0$; second, it provides fast, "Level 1" track triggering in the range $|\eta| < 1.6$.

The CFT consists of approximately 77,000 scintillating fibers that completely cover 8 concentric support cylinders occupying the radial space from 20 to 50 cm (Figure 4.6). Two layers of fibers are formed into a "doublet" layer in such a way that one layer of the doublet is offset by one half of the fiber spacing with respect to its partner (Figure 4.9). This configuration compensates for the geometric gaps between adjacent fibers in a monolayer and provides near-unity detection efficiency per doublet. A fiber doublet layer oriented with the fibers in the axial direction (i.e. parallel to the beam line) is mounted on each of the cylinders. An additional doublet layer oriented in either the u or v stereo angle of approximately $2°$ is mounted on successive cylinders, so that from the smallest radius outward the orientations on the fibers are *xu-xv-xu-xv-xu-xv-xu-xv*.

Each scintillating fiber has a fluorescent polystyrene core surrounded by a thin acrylic cladding, which in turn is covered by another thin fluoro-acrylic cladding. The fiber's diameter is 835 μm and each cladding is 15 μm thick. It scintillates in the yellow-green part of the visible spectrum. The lengths of these fibers range

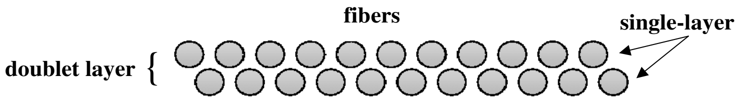

Figure 4.9: *A fiber doublet layer.*

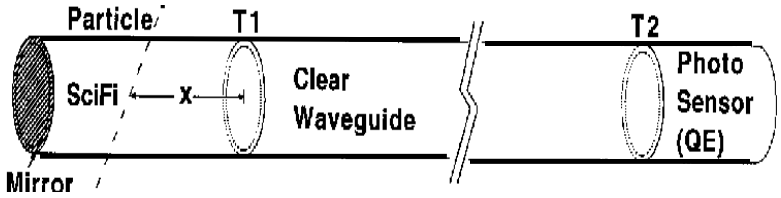

Figure 4.10: *Schematic of a fiber-tracking element. T1 and T2 are the optical interfaces between scintillating fiber, clear waveguide and the VLPC.*

from 166 to 252 *cm*.

The basic principle of scintillating fiber tracking is illustrated in Figure 4.10. Charged particles passing through the scintillating fiber volume will deposit energy by ionization, a portion of which is converted into scintillation light. A fraction of this light is optically trapped inside the fiber and travels to the opposite ends. At one end, there is an aluminum mirror coating that reflects the incoming light back into the fiber. At the other end, the scintillating fiber is mated, through an diamond-finished optical connector, to a clear waveguide fiber[7] which"pipes" the light over some distance (8-11 *m*) to the Visible Light Photon Counter (VLPC) outside of the central detector.

[7]The clear fiber is structurally and chemically identical to the scintillating fibers, but contains no fluorescent dyes.

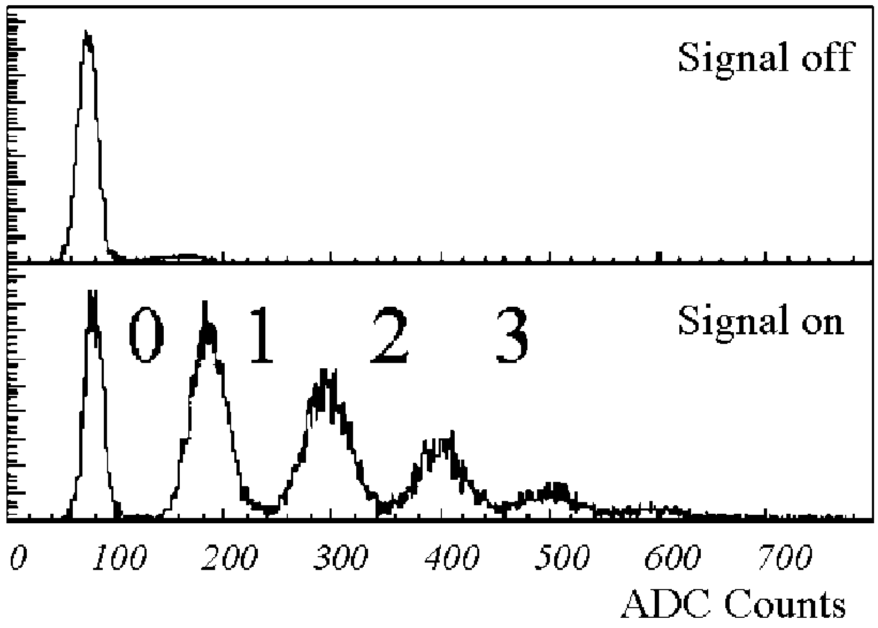

Figure 4.11: *Spectrum from a VLPC when there is no signal and when there are signals.*

The VLPC is a silicon-avalanche device that converts the light into electrical pulses. It has many superior characteristics such as a quantum efficiency of over 80%, a gain of 2000-5000, a rate capability of at least 10 MHz and a noise rate of less than 0.1%. The VLPCs, situated in cryostats on the detector platform, require a cryogenic operating temperature of 6-15K to achieve low noise performance. Figure 4.11 shows the observed spectrum from a VLPC when there is no signal and when there are signals. There is clean separation between the pedestal (no signal), first, second and third photoelectron peaks.

The CFT readout electronics is almost identical to that of the SMT, except that a special "precursor" chip is added between the VLPC and the SVX II for triggering purposes. The Level 1 hardware trigger is implemented using field programmable gate arrays (FPGA). First, only signals from axial layers are used as hits. Coincidences between eight hits form a track. Finally, the tracks are combined with central preshower clusters to form an electron trigger, and with muon detectors to form a muon trigger. On a Level 1 trigger accept, fibers of all layers will then be readout. In order to perform this operation quickly, the tracker is divided into 80 equal azimuthal sectors for parallel processing.

A cosmic ray test of a large-scale CFT prototype was carried out from 1994 to 1995 [36]. The system operated stably during the test and the results were consistent with expectations. The doublet position resolution is found to be about 100 μm as shown in Figure 4.12.

4.4.4 The Preshower Detectors

The Preshower Detectors are designed to aid electron identification and triggering and to correct the electromagnetic energy for losses in the solenoid. The detectors function as a calorimeter by providing an "early" energy sampling and as a tracker by providing precise position measurements.

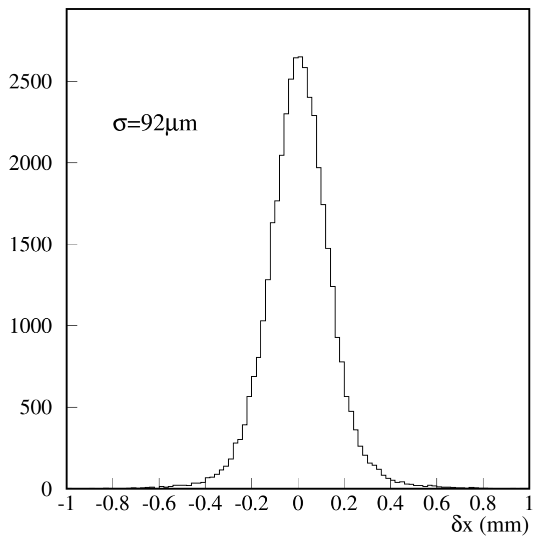

Figure 4.12: *Position resolution for the fiber doublet from cosmic ray tests.*

Central Preshower

The Central Preshower Detector (CPS) [37] is placed in the 51 mm gap between the solenoid coil and the central calorimeter cryostat at a radius of 72 cm, and covers the pseudorapidity region $-1.2 < \eta < 1.2$. The detector consists of three layers of scintillating strips arranged in axial and stereo ($\pm 23^{\circ}$) views with a wavelength-shifting (WLS) fiber readout. Each layer is made into eight octants of ~ 270 *cm* long. A lead absorber before the preshower is tapered along z so that the solenoid plus the lead have a total of two radiation lengths for all particle trajectories. Cross-sectional end and side views of the CPS are shown in Figure 4.13.

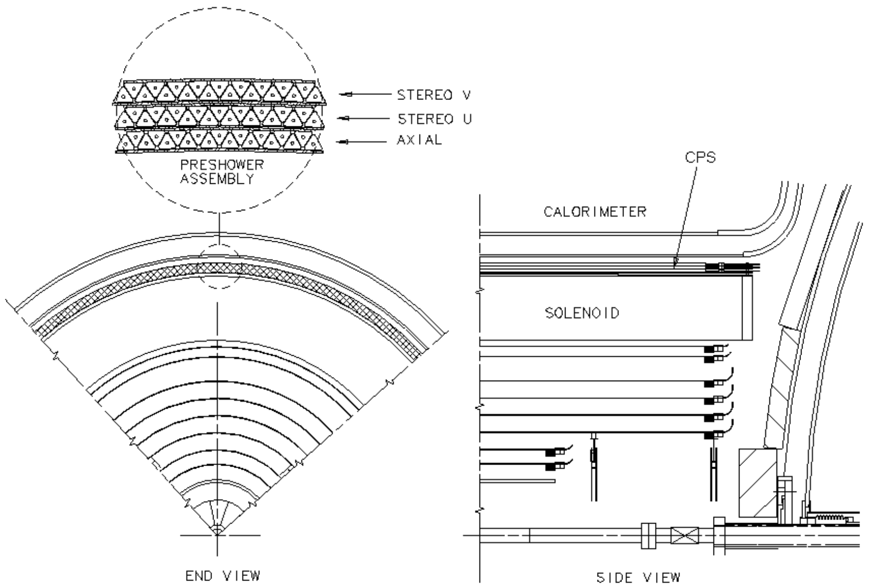

Figure 4.13: *Cross-sectional end view (*left*) and side view (*right*) of the Central Preshower detector.*

The scintillating strips have an equilateral triangular cross section with a 7 mm base and a 1 mm diameter hole in the center to house the WLS fiber. The WLS fibers are split at $z = 0$ and connected to the clear fibers, which transport the scintillation light from the preshower detector to the VLPCs, at both ends of each octant. The fiber splitting at $z = 0$ effectively halves the occupancy for each channel and therefore makes the detector less vulnerable to high rates. There are 24 octants, 48 bundles of clear fibers and a total of 7680 readout channels in the CPS.

The readout electronics is again based on the SVX II chips. Before the VLPC signals are sent to the SVX II for amplification and digitization, they are split

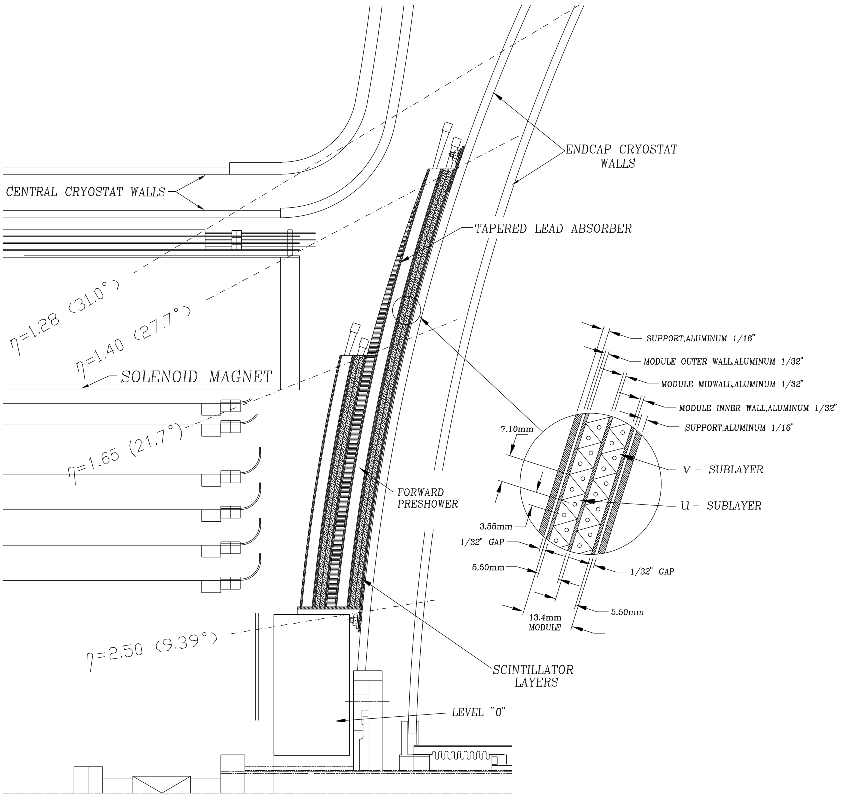

Figure 4.14: *One quarter view of the Forward Preshower detector.*

into two channels to allow for a fast trigger pick-off and to effectively extend the dynamic range of the readout system. The readout for the axial layer is integrated with the CFT readout as a ninth layer and is used in the Level 1 electron trigger.

Forward Preshower

The two Forward Preshower Detectors (FPS) [38] are mounted on the inner face of the two end calorimeter cryostats, as shown in Figure 4.14. In order to make the most effective use of the limited amount of available space in the region, the detectors are made to conform to the outer shell of the cryostats. The same technology as in the central preshower is used for the FPS. The detector is composed of a two radiation length thick lead absorber sandwiched between two active scintillator planes, with each plane consisting of one u and one v sublayer. The FPS has a total of 16,000 channels.

The outer scintillator plane covers the range $1.4 < |\eta| < 2.5$. Since particles traversing the magnet solenoid ($1.4 < |\eta| < 1.6$) are likely to shower upstream of the FPS, the inner scintillator plane in front of the lead absorber is not needed in this region. Therefore, the inner plane covers $1.6 < |\eta| < 2.5$ instead. In that region, the lead is also tapered to equalize the amount of material traversed as a function of η.

Every FPS layer is made of eight azimuthal $45°$ wedges or modules. The central $22.5°$ of each module consists of active scintillator volume and the remaining $\sim 11°$ on either side provides space and mechanical support for routing the WLS fibers. The module positions in successive layers will be staggered by $22.5°$ in order to cover the full azimuthal angle. The clear fibers are routed about the circumference of the FPS and down to the platform below the detector, where the VLPCs are housed.

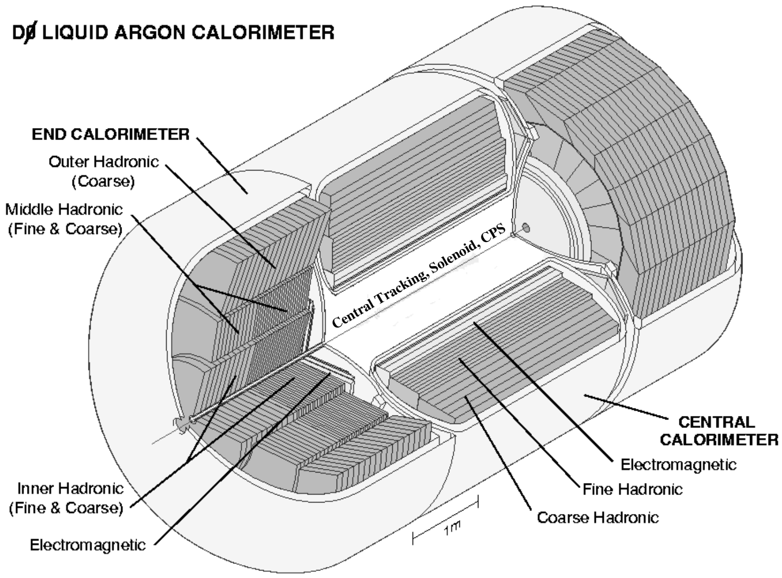

Figure 4.15: *The DØ calorimeter.*

4.4.5 The Calorimeter

The calorimeter is the most important part of the DØ detector. It plays a vital role in the identification of most final states particles by providing kinematic information about electrons, photons and jets. DØ has a sampling calorimeter [30], with liquid argon as the active medium to sample the ionization and with uranium as a dense absorbing material. When passing through the uranium, a particle will interact to produce low energy secondary particles (a process known as *showering*). Its energy is measured by means of measuring the ionization produced by these charged particles in the shower.

High energy electrons and photons produce electromagnetic showers. They interact primarily with the uranium plates in complementary processes: pair production ($\gamma \rightarrow e^+e^-$) and bremsstrahlung ($e \rightarrow e\gamma$). For each successive interaction the number of secondary particles (particle multiplicity) increases and the average energy per particle decreases. These are known as electromagnetic (EM) showers. The energy of the original particle is expected to drop exponentially:

$$E(x) = E_0 e^{-x/X_0} \quad (4.3)$$

where X_0 is known as the radiation length of the material. For uranium $X_0 \approx 3.2\ mm$.

In contrast to electromagnetic particles, high energy hadrons interact with the uranium nuclei with inelastic collisions proceeding via the strong nuclear force. These collisions produce secondary particles, about 1/3 of which are π^0's. While the π^0's produce electrons and photons which interact electromagnetically, the rest of the secondary particles also interact strongly. This type of shower is known as a hadronic shower, and develops more slowly (over longer distance and also larger) than electromagnetic showers. For hadronic showers, the analog to the radiation length in Equation 4.3 is the nuclear interaction length λ_0, which is 10.5 cm for uranium.

Calorimeter Design

In order to retain access to the central sub-detectors, the calorimeter, shown in Figure 4.15, consists of one Central Calorimeter (CC) covering the region $|\eta| < 1.2$, two Endcap Calorimeters (EC) extending the coverage to $|\eta| \approx 4$, and the Inter-cryostat Detector (ICD) to cover their overlapping region $1.1 < |\eta| < 1.4$,. The use of liquid argon requires a containment vessel (cryostat), where the argon is kept at a temperature of $78K$.

The calorimeter is highly modular, and finely segmented in the transverse and longitudinal shower directions. Three distinct types of modules are used in the CC and EC: an electromagnetic section (EM) with relatively thin and closely spaced uranium absorber plates, a fine hadronic section (FH) with thicker and widely spaced uranium plates and a coarse hadronic section (CH) with thick copper or stainless steel plates. Each module consists of a row of alternating absorber plates and signal readout boards, as shown in Figure 4.16. The 2.3 mm gap separating adjacent absorber plates and signal boards is filled with liquid argon. The signal boards consist of a copper pad with two separate 0.5 mm thick G-10 sheets laminated at each end. The outer surfaces of the boards were coated with a highly resistive epoxy. An electric field is established by grounding the absorber plate while applying a positive potential ($\approx$ 2.0 kV) to the resistive surfaces of the signal boards. Incident particles shower in the absorber plates, and the resulting shower particles ionize the liquid argon in the adjacent gap. The liberated electrons drift to the signal boards (the drift time is $\sim 450\ ns$), and induce a signal on the copper pad. Signals from several signal boards in the same η and ϕ region are ganged together in depth to form a *readout cell*.

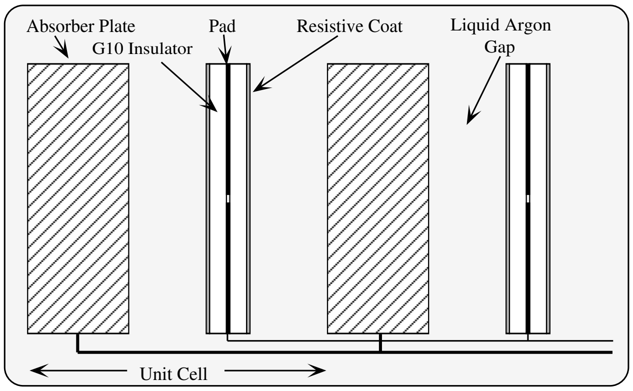

Figure 4.16: *Schematic view of a calorimeter cell.*

The pattern and sizes of the readout cells were determined from considerations of shower sizes. The transverse dimensions of the readout cell were chosen to be similar to the transverse sizes of showers: $\sim$ 1-2 cm for EM showers and $\sim 10\ cm$ for hadronic showers. Furthermore, longitudinal segmentation within the EM, FH and CH layers helps in distinguishing and separating electrons from hadrons. The design was chosen to be *pseudo-projective*: the centers of the cells lie on lines which project back to the center of the detector, but the cell boundaries are aligned perpendicular to the absorber plates. This is clearly illustrated in Figure 4.17.

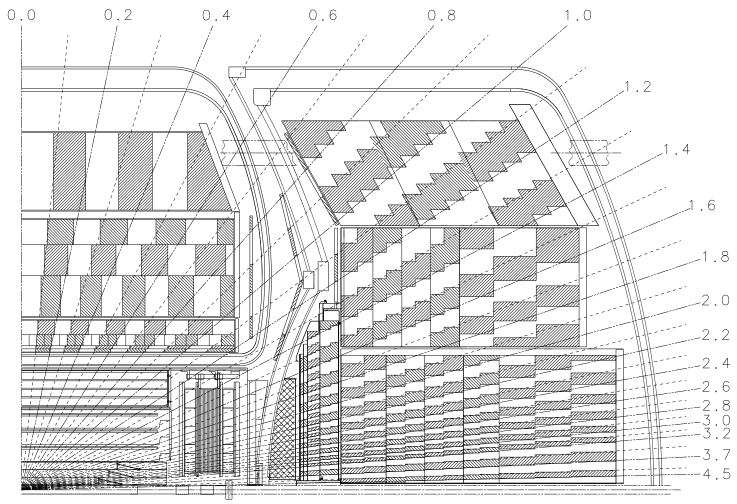

Figure 4.17: *Side view of one quandrant of the calorimeter. Shown values are the η segmentation.*

The calorimeter was tested and calibrated using test beam in its final stages of assembly [30]. The calorimeter was not modified for Run II.

The Central Calorimeter

The Central Calorimeter (CC) is composed of three cylindrical concentric shells (EM, FH and CH) parallel to the beam axis with about 18k channels in total.

The first four inner layers of the CC provide measurement of the EM showers at depths of 2, 4, 11, and 21 radiation lengths[8]. Taken together these layers comprise

[8]These are distances in the calorimeter not taking into account the 2 radiation lengths due to the solenoid and lead absorber added in Run II. As a result, the showering is expected to start earlier in Run II than designed for Run I. It is also true in the EC.

0.76 nuclear absorption lengths. The first, second and fourth layers have a cell segmentation of 0.1×0.1 in $\eta \times \phi$. The maximum of the shower development occurs in the third layer, so the segmentation in that layer is increased to 0.05×0.05 for a more precise measurement of the location and shape of the shower.

Beyond the EM layers are the three Fine Hadronic (FH) layers at depths of 1.3, 1.0 and 0.9 nuclear absorption lengths. All three layers have a cell segmentation of 0.1×0.1. After the FH is the Coarse Hadronic (CH) layer, providing a single readout layer having a depth of 3.2 nuclear absorption lengths.

The Endcap Calorimeters

The Endcap Calorimeters (EC) are located on either side of the CC, covering the region $1.0 < |\eta| < 4$. There are about 36k channels in the two EC's.

The EM readout layers have a thickness 0.3, 2.6, 7.9 and 9.3 radiation lengths comprising about 0.75 nuclear absorption lengths. For $|\eta| \leq 2.6$, the cell segmentation is the same as in the CC. For $2.6 < |\eta| < 3.2$, the segmentation in the third layer is decreased to 0.1×0.1. For $|\eta| \geq 3.2$, segmentation in all layers is decreased to 0.2×0.2 and continues to decrease until it is 0.4×0.4 for $|\eta| \approx 4$.

In the EC are three hadronic modules. Closest to the beam pipe is the inner hadronic module consisting of four fine hadronic (IFH) layers and one coarse hadronic (ICH) layer. The middle hadronic module surrounds the inner module in ϕ and has four fine hadronic (MFH) layers and a single coarse hadronic (MCH) layer. The outermost module is the outer hadronic (OH) module consisting of three coarse hadronic layers. In the range $0.7 < |\eta| < 1.1$, the EM and FH modules are in the CC while the CH module is in the EC.

The Inter-cryostat Detectors

Due to the structure and support system of the calorimeter cryostats there exists a gap in the coverage between the CC and EC Calorimeters. The gaps span approximately $1.1 < |\eta| < 1.4$, with the result that there is only partial instrumentation of the EM and FH sections. This partial coverage creates a lack of uniformity in the energy response and acceptance within this region. The region has a substantial amount of absorption material with no energy sampling in the first radiation length. To supplement coverage in the region, two different types of detectors are adopted. The Inter-cryostat Detector (ICD) [39] consists of a single layer of scintillating tiles positioned on the inner walls of the EC cryostat to provide energy sampling in this region. The light signals, picked up by wavelength shifting fibers in the tile, are transported along 8 m clear fibers to the photo detection readout located outside the region of magnetic field in the inter-cryostat region. Additional coverage is provided by the Massless Gaps (MG). These are detectors consisting of a readout cell having a signal board embedded

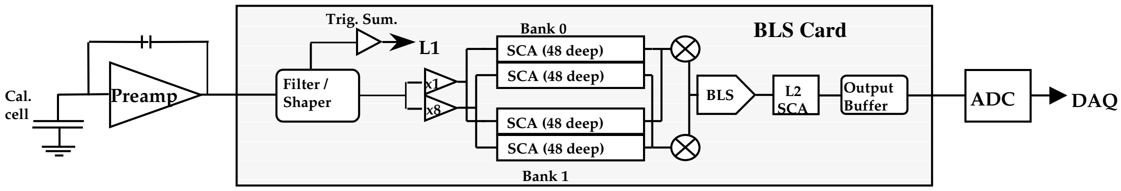

Figure 4.18: *Schematic of the calorimeter readout electronics.*

in liquid argon positioned inside both the CC and EC cryostat walls to provide full coverage in ϕ.

Calorimeter Readout

The upgrade of the calorimeter system is restricted only to its front-end electronics to accommodate the reduced crossing time and increased luminosity [40]. Figure 4.18 shows the schematic of the upgraded calorimeter readout system. The calorimeter has about 55,000 electronics channels in total.

Signals from the calorimeters are carried through four ports in the cryostats via 30Ω coaxial cables to charge sensitive preamplifiers (preamps) mounted on top of the cryostats. The preamps are integrating circuits that convert the charges produced by the calorimeter cells to voltages that are proportional to the input integrated charge. Variations in detector capacitance produce some intrinsic deviations in the input charge shape. The preamps are divided into fourteen species as a means to compensate for these differences. To achieve better noise performance, the preamps of Run II use dual low-noise FETs design and enhanced output drivers.

The preamps output pulse is delivered over twist and flat cable to the baseline subtractor (BLS) system located in the platform underneath the detector. The pulse is then differentiated to extract the height of the voltage with two RC circuits in BLS cards. They act as high-pass frequency filters, one to shape (called *shaper*) and one to cancel the decay of the preamp. The shaped signal is sampled at its peak at about 320 ns[9], and the output (voltage) is split in two. The first set of outputs is summed into $\Delta\eta \times \Delta\phi = 0.2 \times 0.2$ trigger towers by trigger summer chips and used as inputs to the Level 1 calorimeter trigger (called *pick-offs*). The second set of outputs are either reduced by $\times 0.5$ (Gain 1 for large signals) or amplified by $\times 4$ (Gain 8 for small signals) to reduce the dynamic range of signals for storage. A bit records which gain is used for later restoration.

The output from the gain path is stored in an analog pipeline called the Switched Capacitor Array (SCA). The pipeline is needed because the Level 1 trigger decision requires $\sim 4\ \mu s$, but samples are taken every 132 ns. The SCA is essentially an analog time delay element which holds samples (48 for each channel) until they are either readout or discarded. It is a silicon integrated circuit chip containing a 12-channel by 48-depth capacitor array which can store analog voltages from 0-5V in level with a precision of about 12 digital bits. A dual-pipeline

[9]Because of the earlier sampling (320 ns) compared to the liquid argon drift time (430 ns), only 2/3 of the charge left in the calorimeter is actually used.

is used to eliminate deadtime and signals are toggled between the two pipelines so that one pipeline is reading out while the other is being filled with data.

When the Level 1 trigger system has fired, indicating an event of interest at Level 1, the signals in the corresponding depth in SCA are read out, a *baseline subtraction* is performed and the results are sent to another similar analog pipeline (L2 SCA) waiting for Level 2 trigger decision. If an event is accepted at Level 2, its signals held in L2 SCA are sent to 24-channel 12-bit ADCs (Analog to Digital Converters) in the moving counting house (MCH), which digitize and zero-suppress the signals, and then send them on to the Data Acquisition System (DAQ).

The idea of baseline subtraction is as follows: At each bunch crossing, the charge received by the preamp produces a step function in the preamp output with a rise time of about 430 ns. The step then decays with a very long time constant of 15 micro sec. The output is therefore, cumulative over successive bunch crossings. To obtain the precise pulse height from a specific bunch crossing, the pulse height sampled 396 ns earlier is used as the *baseline*, and then subtracted from the current pulse height.

The calorimeter electronics is calibrated using Pulser Calibration System. It supplies a precise charge pulse of known value to each preamp input in a repeatable manner. The charge serves as both a calibration signal and an indicator that each channel is functioning.

Calorimeter Performance

The calorimeter was tested and calibrated using test beam in its final stages of assembly [30]. Its response to single electrons and pions, with energies from 10 GeV to 150 GeV, is found to be linear to within 0.5%. The energy resolution is measured to be

$$For\ electrons: \quad (\frac{\sigma_E}{E})^2 = (0.3\%)^2 + \frac{(15\%)^2}{E} \tag{4.4}$$
$$For\ pions: \quad (\frac{\sigma_E}{E})^2 = (4.0\%)^2 + \frac{(45\%)^2}{E} \tag{4.5}$$

In Run II, due to the additional materials between the beam pipe and the calorimeter, the resolutions are expected to become worse. The electron energy resolution is measured by fitting

$$\frac{\sigma_E}{E} = \sqrt{C^2 + \frac{S^2}{E}}$$

to the observed $Z \to ee$ width ($m_Z = 91.2$ GeV) and $\Upsilon \to ee$ width ($m_\Upsilon = 9.5$ GeV) in data [41]. Preliminary results are $C \sim 5.5\%$ and $S \sim 29\%\ GeV^{1/2}$. The resolution is expected to be greatly improved by using information from the preshower detectors and by optimizing the calorimeter response, which are actively

position in EM3	a	b
$z \leq -150\ cm$	0.988	0
$-150\ cm < z \leq 0,\ 90^\circ \leq \phi \leq 270^\circ$	0.996	0
$-150\ cm < z \leq 0,\ \phi < 90^\circ\ or\ \phi > 270^\circ$	1.008	0
$0 < z < 150\ cm,\ 90^\circ \leq \phi \leq 270^\circ$	0.987	0
$0 < z < 150\ cm,\ \phi < 90^\circ\ or\ \phi > 270^\circ$	1.006	0
$z \geq 150\ cm$	1.017	0

Table 4.2: *Electron energy scale for electrons in different parts of the calorimeter.*

being worked on.

The electron energy scale is calibrated by matching the observed Z peak to its precisely known mass. We have [42]

$$E = a \cdot E_{cal} + b \tag{4.6}$$

where E_{cal} is the electron energy measured by the calorimeter, E is the energy after correction, a and b are summarized in Table 4.2.

The jet (e.g. pion) energy resolution and energy scale are measured using direct photon (γ+jet) events and dijet events from data as described in [43]. The correction factor for the jet energy scale is approximately 1.4 . The jet energy resolution is found to be $C \sim 6.4\%$ and $S \sim 94\%\ GeV^{1/2}$ in the CC, $C \sim 8.6\%$ and $S \sim 0.0\%\ GeV^{1/2}$ in the EC, and $C \sim 13.6\%$ and $S \sim 50\%\ GeV^{1/2}$ in the ICD.

4.4.6 The Muon System

Muons are minimum ionizing particles and usually escape the calorimeter without producing an EM or hadronic shower. The DØ muon system [38] consists of a Wide Angle Muon System (WAMUS) for $|\eta| \leq 1$ and two Forward Angle Muon Systems (FAMUS) for $1 < |\eta| < 2$ (Figure 4.5). It uses a toroidal magnet to bend the trajectory of the muon and thus obtains a measurement of its momentum.

In the WAMUS, proportional drift tubes (PDTs) are used in three layers, A, B, and C, corresponding to immediately inside, immediately outside, and about one meter outside the toroid, respectively. Two layers of scintillation counters are added in Run II to provide fast muon triggers. In the FAMUS, three planes of mini-drift tubes (MDTs) are used instead of PDTs and three layers of scintillators are installed for triggering.

4.4.7 The Trigger and Data Acquisition System

The DØ trigger and Data Acquisition System (DAQ) [31] is used to select and record physics events of interest for later analysis. It consists of four main decision levels of increasing sophistication in event selection: three hardware triggers (L0, L1 and L2) and a software trigger (L3). The Level 0 (L0) indicates the presence of an inelastic collision. The Level 1 (L1) and Level 2 (L2) provide a fast decision as to whether keep or discard an event based on fast detector pick-offs. Events that

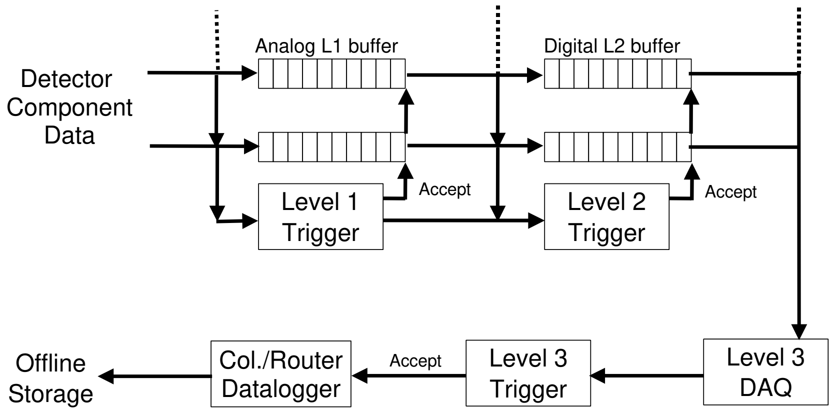

Figure 4.19: *Schematic of the trigger and data acquisition system.*

pass the L2 are fully digitized and transported via the data acquisition system to a farm of computers, where the Level 3 (L3) performs a quick, simple reconstruction of the events and sends accepted events for recording. The L1 makes a decision in $\sim 4\ \mu s$ and L2 in $\sim 100\ \mu s$. The expected trigger accept rates are roughly 1.4 kHz, 700 Hz, and 50 Hz at L1, L2, and L3 respectively. Figure 4.19 shows the schematic of the trigger and data acquisition system.

Level 0 and Luminosity Monitor

The primary purposes of Level 0 are to detect non-diffractive inelastic collisions with high efficiency and to make accurate luminosity measurements [44]. It consists of two arrays of plastic scintillation counters located on the inside faces of the end cryostats and arranged symmetrically about the beam pipe, covering the region $2.7 < |\eta| < 4.4$. The scintillation light is read out using fine-mesh photo-multiplier tubes attached directly to the scintillation pixels.

In addition, the difference in arrival time for particles hitting the two L0 detectors is used to provide fast determinations of the z-coordinate of the event vertex for use in next levels of triggers. It can also provide diagnostic information regarding accelerator performance.

Level 1

The Level 1 trigger [45] is a flexible and programmable hardware system. It collects prompt detector data (*pick-offs*) from sub-detectors and makes a very fast trigger decision after combining and comparing them with its 128 criteria (called *triggers*). The upgraded L1 trigger system includes the calorimeter, the central fiber tracker, the central/forward preshower, and the muon detectors. Electron triggering is provided by the first three in the range $|\eta| < 2.5$.

The L1 trigger devices examine each event and report their findings to the L1 Framework (LlFW) every 132 ns. If any one of the 128 criteria is satisfied, the L1FW issues an accept and the event data is digitized and moved from the pipeline into a series of 16 event buffers to await for L2 trigger decision. The L1 system is synchronized with the beam crossings within the detector and renders decisions within a ~ 4 μs interval. Data rate is reduced to about 1.4 kHz after L1.

The inputs to the Level 1 calorimeter trigger system (L1CAL) are the energy deposited in so-called *trigger towers*. A trigger tower is formed by the sum of all calorimeter cells in a $\Delta\eta \times \Delta\phi = 0.2 \times 0.2$ window. There are 1280 trigger towers in total. Each trigger tower can be further divided into EM trigger tower (sum of cells in EM layers of the calorimeter) and hadronic trigger tower (sum of cells in FH layers). The energy deposited in a trigger tower is provided by the fast pick-off signals from the BLS cards (Section 4.4.5). Each calorimeter trigger requires the energy deposit above a preset threshold (called *reference sets*) in one or more trigger towers. For example, the "2EM_HI" trigger requires two calorimeter EM trigger towers with energy > 10 GeV. A total of sixteen reference sets are available. There are also triggers based on some global quantities, such as total energy and missing E_T, which are computed from the sum of trigger towers.

Level 2

The Level 2 trigger [38], using multi-detector correlations of objects found in the event, reduces the accept rate by a factor of ten within $\sim 100\ \mu s$. Two distinct stages are needed in L2: the preprocessor stage and the global processor stage. A L2 Framework (L2FW) similar to L1FW is used to coordinate the operation of L2 and report trigger decisions to L3.

In the preprocessor phase, each detector system separately builds a list of trigger information. Individual preprocessors exist for the calorimeter, the CFT, the muon and the preshower detectors. For each subsystem, the L1 trigger information is retained and transformed into physical objects such as energy clusters or tracks. The global processor receives preprocessor information and, for the first time, combines L1 trigger objects from different detectors to identify a particle. For example, spatial correlations between track segments, preshower depositions, and calorimeter energy depositions may all be used to select electron candidates. There are 128 L2 triggers available.

The calorimeter preprocessor consists of several sub-units: an EM preprocessor, a jet preprocessor and a missing E_T preprocessor. The preprocessor input is the full array of 1280 trigger tower E_Ts for both EM and EM plus hadronic sums. Clustering algorithms build electron or jet candidates, calculate their position and energy and test them for shape and transverse energy requirements.

Level 3 and Data Acquisition System

The Level 3 system [46] functions as the Data Acquisition system (DAQ) as well as the L3 software trigger. Upon receipt of a L2 accept from the global processor, L3 will initialize full detector readout and collect data through about 70 VME crates for each event. The total event size is about 250 kB, with 1-10 kB in each VME crate.

A single-board computer (SBC) is placed in each VME crate. The SBC reads out the VME modules and sends the data over Ethernet to one of the L3 processor farm nodes for software-filtering and event-building. There are currently 48 farm nodes, but the system is expandable.

Software filtering [47] is accomplished by a series of *filter tools*. Each tool has a specific function related to the identification of a type of particle or event characteristic. Tools exist for jets, muons, EM objects, tracks, scalar E_T, missing E_T, etc. The filter tools are associated in particular combinations and ordered into 128 L3 scripts. If any of the L3 scripts is passed, the event will be sent via the network to a collector machine to be logged and recorded on permanent storage media at a rate of 50 Hz.

Chapter 5

Event Reconstruction and Data Selection

5.1 Offline Event Reconstruction

The raw event data from the detector is in the form of digitized signals such as charges, pulse heights, etc. These quantities will be converted into meaningful data such as EM cluster energy, track position, by a software package known as DØRECO. Event reconstruction can be divided into three main stages:

Hit Finding The raw detector data is unpacked and converted into hits, which consist of energy deposits in calorimeter cells, signals on tracking layers, etc.

Clustering and Tracking Hits whose spatial separation is small are combined to form clusters in the calorimeter and preshowers or tracks in the tracking systems.

Particle Identification Clusters and tracks as well as other information are combined to identify electron, photon, jet, or muon candidates. The identification criteria are quite loose at this stage to guarantee high efficiency so as not to lose any candidates.

DØRECO also computes many selection variables to be used in further analysis, where much tighter selection cuts are usually applied.

5.1.1 Track and Vertex Reconstruction

Hits from the CFT and SMT are used to reconstruct the trajectories of charged particles. Because of the magnetic field in the z-direction, the hits of a charged particle lie along a curve, whose curvature in the x-y plane is used to measure its transverse momentum. The track finding algorithm is road-following with a Kalman filter update implemented using the TRF++ software package [48]: tracking is first done for each individual layer to produce track segments; the track segments are matched between layers and detectors to form global track candidates; a fit of a track and nearby hits is then performed and the track is accepted (rejected) if the fit is good (poor) as determined by the χ^2 value.

The interaction point of an event is called the *vertex*. There are two types of vertices: a *primary vertex* is the original interaction point with the largest number of associated tracks; a *secondary vertex* is a displaced vertex due to long-lived mesons decay (e.g. B or D). The x and y coordinates of the primary vertex are close to zero since the cross sectional extent of the beam is $\approx 40\ \mu m$ [49]. However, the z coordinate has a range of $\sigma_z = 25\ cm$ around $z = 0$. The vertex reconstruction uses LEP's "impact parameters" algorithm [50].

The primary vertex candidates are found as follows: 1. Select global tracks with at least one hit in the SMT (DØRECO Version p13); 2. Fit a vertex position from them; 3. Remove bad tracks with a large contribution to the χ^2 (currently > 500); 4. Repeat the procedure; 5. To handle events having multiple interactions, restart the vertex search using excluded tracks. Finally, the vertex candidate containing at least 3 tracks and with one of those having the greatest p_T is selected as the primary vertex of the event. The secondary vertex search uses the following procedure: 1. Form a good seed from two tracks that do not belong to the primary vertex, and fit the vertex; 2. Add one track and refit the vertex; 3. If the χ^2 becomes smaller, the track is good and saved; 4. Go to 2 and repeat until there is no more good tracks. There could be more than one secondary vertex.

5.1.2 Energy Measurement

The calorimeter readout is in ADC counts, which is proportional to the energy deposited in calorimeter cells (charge). The energy deposited is a fraction of the total energy of the particle since the calorimeter only samples a fraction of the total energy, known as the "sampling fraction". The sampling fractions (~5% on average) are primarily determined from test beam measurements. The conversion from ADC counts to the total physical energy in GeV is approximately 4-5 MeV per ADC count on average [51].

After finding the calorimeter cell energies in GeV, cells with the same η and ϕ are summed together for the EM and hadronic layers of the calorimeter to form readout "towers":

$$E_{tower}^{EM}(\eta, \phi) = \sum_{EMs+FH1} E_{cell}(\eta, \phi, layer) \tag{5.1}$$

$$E_{tower}^{TOTAL}(\eta, \phi) = \sum_{all\ layers} E_{cell}(\eta, \phi, layer) \tag{5.2}$$

These towers serve as the building blocks or *seeds* for the subsequent jet and electron cluster finding algorithm.

5.1.3 Jet, Muon and Neutrino Identifications

Jet

A parton (quark or gluon) will appear as a jet in the detector due to color confinement through a process known as *hadronization*, since the quark produces a large number of colorless hadrons that appear in the detector as a collimated "jet" of hadronic particles. The process of jet identification involves finding these jets within the calorimeter, and measuring their kinematic features in order to relate them to the original parton. The jet reconstruction uses a cone algorithm [52]. It starts by merging adjacent calorimeter towers above threshold (1 GeV) to form preclusters. Then, it uses a fixed cone of radius $\mathcal{R} = \sqrt{\Delta\eta^2 + \Delta\phi^2}$ in the $\eta \times \phi$ space to construct jet clusters from these preclusters (merge/split when there are shared towers). Two cone sizes are available in the algorithm, $\mathcal{R} = 0.5$ or $\mathcal{R} = 0.7$. The first one is often used in electron related studies since the cone size is close to that used in electron reconstruction. The larger cone size is often used in analyses requiring more accurate jet energy.

Muon

The offline muon identification is based on a match between a track detected in the central trackers and a signal in the muon system. To be used as a seed for a muon object, a charged particle is required to have $p_T > 1.5$ GeV. The muon signal can be a track penetrating the toroid, a track segment reconstructed inside the toroid (an A-layer segment), or just a set of hits detected in the muon detectors. The angle between the track in the B and C layers and the track in the A-layer is computed to measure the muon momentum.

Neutrino

Neutrinos (and other weakly interacting neutral particles) are not directly detectable by the DØ detector. Their presence is inferred from an overall momentum imbalance in the event. Since the total momentum is conserved in the transverse plane, a large missing E_T, denoted as $\not\!\!E_T$, indicates the production of high-p_T neutrino(s). The negative of the vector sum of all measured particles is assigned to be the momentum vector of the neutrino(s).

5.2 Electron Reconstruction and Identification

The showers from electrons and photons are very similar: concentrated clusters of energy deposited mainly in the electromagnetic (EM) layers of the calorimeter. Hence, the reconstruction of these objects in the calorimeter uses the same algorithm. The only distinguishing feature between electrons and photons is the association of the electron cluster with a track in the central trackers.

5.2.1 EM Cluster Reconstruction

An electromagnetic tower consists of four EM layers and the first hadronic (FH1) layer of the calorimeter. There are two major clustering algorithms to form EM clusters from these towers: the simple cone (Scone) algorithm and the CellNN algorithm.

Scone

Scone is a simplified version of the fixed cone algorithm in the jet reconstruction (Section 5.1.3) without the merging/splitting part. First, the highest E_T EM towers are selected as the starting points of the preclusters. Adjacent EM towers above 50 MeV are added to a precluster if they are within a window of 0.3×0.3 in $\eta \times \phi$ (for CC) or within a cone of 10 cm radius in EM3 (for EC). Second, all EM towers within a cone of radius $\mathcal{R} = \sqrt{\Delta\eta^2 + \Delta\phi^2} = 0.4$ with respect to the precluster axis are added to the precluster. Then, the axis is recalculated and the second step is repeated until the final cluster does not change. The Scone algorithm is used in this analysis.

CellNN

CellNN is a cell-nearest-neighbor algorithm [53] based on calorimeter cells rather than on towers. In each calorimeter layer, the cell with the highest energy is used as a seed. A precluster is formed in each calorimeter layer by merging the seed cell with their neighboring cells. This procedure repeats with the other cells left outside the existing precluster. Each precluster in EM3 initiates a global cluster and, layer by layer, preclusters matching an angular requirement are added to the global cluster. The CellNN algorithm is good for reconstructing electrons in events involving a lot of jets in the final state, since it better separates the electron with its nearby jet.

5.2.2 Preshower Cluster Reconstruction

Electrons and high-p_T photons will produce EM showers in the preshower detectors. The preshower clusters are reconstructed to help electron identification. In each sublayer of the Forward Preshower, contiguous strips with energy above a threshold are combined into channel clusters. For each crossing of a channel cluster in sublayer u with one in sublayer v, a reconstructed cluster is created. In the Central Preshower, single layer clusters are first formed similarly; 3D clusters are then reconstructed if there are "u-v-axial" three-layer matches.

5.2.3 Offline Electron Candidates

For each calorimeter cluster found, its kinematic properties are calculated. After all possible clusters have been identified, the ones which pass the following cuts are considered as electron candidates:

- The total transverse energy of the cluster $E_T > 1.5$ GeV;
- More than 90% of the total energy of the cluster is deposited in the EM layers of the calorimeter;
- The shower isolation[1] < 0.2.

For each electron or photon candidate, the centroid of the cluster is calculated as a weighted mean of the coordinates of the center of the cluster cells in the third layer of the EM calorimeter:

$$\vec{x}_{clus} = \frac{\sum_i w_i \vec{x}_i}{w_i \vec{x}_i} \tag{5.3}$$

the weights w_i are defined as:

$$w_i = \max\left(0, w_0 + \ln\left(\frac{E_i}{E}\right)\right) \tag{5.4}$$

where E_i is the energy in the i^{th} cell, E is the energy of the cluster. This logarithmic weighing is motivated by the exponential lateral profile of an electromagnetic shower. w_0 is a parameter chosen to optimize the position resolution, and is found to be η and ϕ dependent.

[1] See definition in Section 5.2.4.

At this juncture, a distinction between electrons and photons is made by finding matching tracks in the central tracking system. Since photons have no charge, they do not leave signals in the tracking system. A road, 0.05×0.05 in $\Delta\eta \times \Delta\phi$, is defined between the calorimeter cluster and the primary vertex positions. A search for a track with $p_T > 1.5$ GeV is performed within this road. If one or more tracks are found, the candidate is considered as an electron and assigned an id of ± 11 (the sign is opposite to the charge of the best matched track, i.e. 11 for electrons and -11 for positrons.); otherwise, it is taken as a photon and assigned an id of 10.

In this study, we will use an improved track matching algorithm (Section 5.2.4). Hence, this default track matching result is neglected by requiring id $= 10$ or ± 11.

5.2.4 Standard Electron Identifications

After the reconstruction of electrons and photons there remains a considerable amount of background that contaminates the reconstructed sample. Additional constraints must be applied to reduce these backgrounds. The following is a description of the standard quantities employed for electron identification.

Electromagnetic Energy Fraction

The Electromagnetic Energy Fraction (*EM fraction*) is defined as the fraction of the total energy of the cluster that is deposited in the EM layers of the calorimeter. An electron and photon candidate must have $EM\ fraction > 0.9$. Figure 5.1(a) shows the EM fraction distribution for electrons from $Z \rightarrow e^+e^-$ decays and electrons from multijet events.

Shower isolation

Since the electrons produced by the decay of a Z/Z' boson are not produced in association with other particles, the calorimeter clusters corresponding to these electrons should appear isolated. Electromagnetic clusters are narrow compared with the clusters produced by hadronic particles, and they are usually contained in a cone of radius $\mathcal{R} = 0.2$ in the $\eta - \phi$ space. The variable which allows us to quantify the degree of isolation of an electromagnetic cluster is defined as:

$$isolation \ = \frac{E_{total}(0.4) - E_{EM}(0.2)}{E_{EM}(0.2)} \tag{5.5}$$

where $E_{total}(0.4)$ is the total energy contained in an isolation cone of radius $\mathcal{R} = 0.4$, and $E_{EM}(0.2)$ is the electromagnetic energy in a core cone of radius $\mathcal{R} = 0.2$. Figure 5.1(b) shows the distribution of isolation for electrons from $Z \rightarrow e^+e^-$

decays and electrons from multijet events.

H-Matrix χ^2

The shower shape may be characterized by the fraction of cluster energy that is deposited in each layer of the calorimeter. The "H-Matrix" is used to quantify that shower shape. The fractions are dependent on the energy of the incident particle and are correlated, i.e. a shower which fluctuates and deposits a large fraction of its energy in the first layer of the calorimeter will deposit a smaller fraction in the subsequent layers and vice versa.

To take into account the energy deposited by an electron in a given layer as well as its correlations with the energy deposited in the other layers, we use a covariance matrix (M) of 8 variables x_i to characterize the "*electron-ness*" of the shower. The matrix elements are computed from a reference sample of N Monte Carlo electrons. The matrix elements are defined as:

$$M_{ij} = \frac{1}{N} \sum_{i,j=1}^{8} (x_i^n - \bar{x}_i)(x_j^n - \bar{x}_j) \tag{5.6}$$

where x_i^n is the value of the i^{th} observable for the n^{th} electron and $\bar{x_i}$ is the mean of the i^{th} observable. The observables reflect the fractional energies in layers, shower widths and the logarithm of the cluster energy. Finally, the position of the event vertex along the beam direction is included to take into account the dependence of the electron shower shape on the point from which the electron is originated.

For a shower, characterized by the observables x'_i, the covariance parameter

$$\chi^2 = \sum_{i,j=1}^{8} (x'_i - \bar{x}_i) H_{ij} (x^n_j - \bar{x}_j) \tag{5.7}$$

where $H = M^{-1}$, measures how consistent its shape is with that expected from an EM shower. Comparisons of the χ^2 distribution for electrons from $Z \rightarrow e^+e^-$ decays and electrons from multijet events are shown in Figure 5.1(c).

Improved Track Matching

The track of a genuine electron is expected to be well aligned with the calorimeter cluster. To quantify the quality of the cluster-track matching, the track is extrapolated into the EM3 layer of the calorimeter. The difference between the projection and the cluster is determined in both position (z in CC, r in EC) and transverse direction (ϕ).

We define the track match significance χ^2 for electrons in CC as [2]:

$$\chi^2\ (CC) = (\frac{\Delta\phi}{\sigma_\phi})^2 + (\frac{\Delta z}{\sigma_z})^2 \tag{5.8}$$

[2]Another definition includes the E/p term, $\chi^2 = (\frac{\Delta\phi}{\sigma_\phi})^2 + (\frac{\Delta z}{\sigma_z})^2 + (\frac{E/p-1}{\sigma_{E/p}})^2$, where E is the cluster energy and p is the track momentum. This definition is not used in this analysis since the track momentum measurement has large error for very energetic electrons ($1/p \rightarrow 0$).

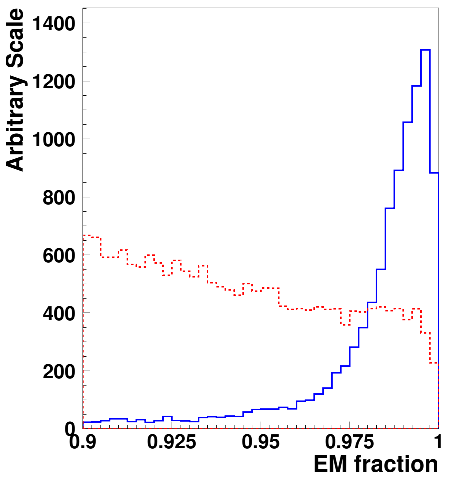

(a)

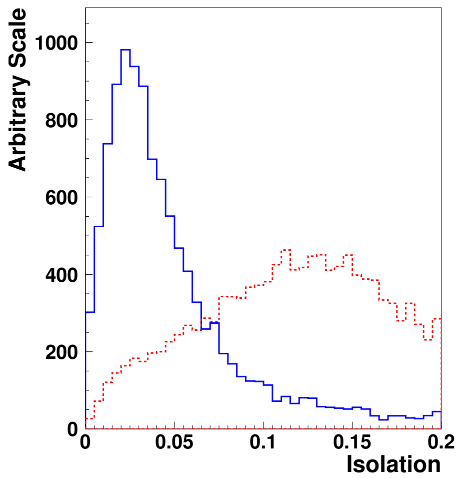

(b)

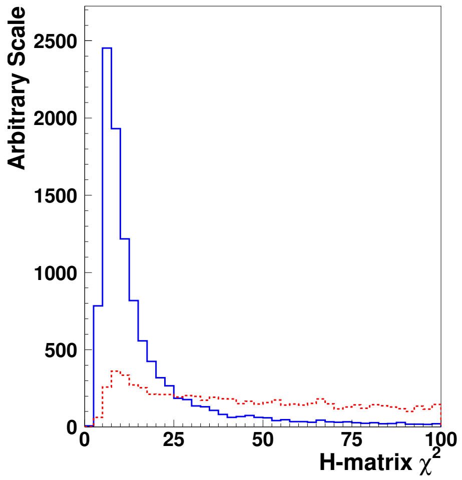

(c)

Figure 5.1: *EM fraction (a), isolation (b) and H-Matrix (×8)* χ^2 *(c) distributions for electrons from* $Z \rightarrow e^+e^-$ *decays (*solid line*) compared with those from multijet triggered events (*dashed line*).*

where $\Delta\phi$ is the angle difference in transverse direction, Δz is the spatial difference in position, σ_ϕ and σ_z are the corresponding resolutions. Figure 5.2(a) shows the distribution of Δz vs. $\Delta\phi$ for electrons from $Z \to e^+e^-$ decays. Similarly, we define the track match significance χ^2 for electrons in EC as:

$$\chi^2\ (EC) = (\frac{\Delta\phi}{\sigma_\phi})^2 + (\frac{\Delta r}{\sigma_r})^2 \tag{5.9}$$

where $\Delta\phi$ is the angle difference in transverse direction, Δr is the spatial difference in radius, σ_ϕ and σ_r are the corresponding resolutions in EC.

We then compute the probability of getting a certain track match significance χ^2 according to the standard χ^2-distribution whose number of degrees of freedom equals 2. Figure 5.2(b) shows the distribution of the probability of track match significance χ^2 for electrons from $Z \to e^+e^-$ decays.

Tracks with a track match significance χ^2 probability > 0.01 are considered good matches. Compared with the road method in Section 5.2.3, this algorithm has a similar efficiency for electrons and 3 times more rejection rate for jet backgrounds.

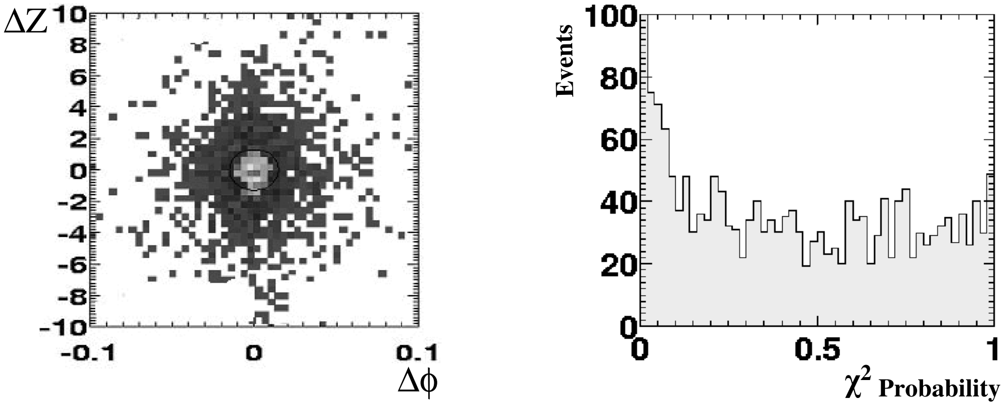

(a) (b)

Figure 5.2: *Distributions of track matching variables (Δz vs. $\Delta\phi$) (a) and distribution of the track match significance χ^2 probability for electrons from $Z \rightarrow e^+e^-$ decays (b).*

5.3 Data Sample and Event Selection

This analysis is based on data collected by the DØ detector, with $p\bar{p}$ collisions at $\sqrt{s} = 1.96$ TeV, from September 2002 to June 2003 during the Tevatron Run II. The data were reconstructed by DØ RECO versions p13.05 and p13.06. Bad detector quality runs (CAL or CFT or SMT) are removed from the sample. This reduces the data sample by ~5%. The integrated luminosity of this sample for the trigger used in this analysis is 122 pb^{-1}. The following criteria are used to select Z' candidates:

Events are required to pass one of the following triggers:

- *EM_HI_SH*

  Level 1: at least one EM trigger tower having $E_T > 10$ GeV;

Level 2: one EM candidate with $E_T > 12$ GeV;

Level 3: a $|\eta| < 3$ electron with $E_T > 20$ GeV meeting loose criteria including a transverse shower shape requirement.

- *EM_MX_SH*

  Level 1: at least one EM trigger tower having $E_T > 15$ GeV;

  Level 3: a $|\eta| < 3$ electron with $E_T > 20$ GeV meeting loose criteria including a transverse shower shape requirement.

- *2EM_HI*

  Level 1: two Calorimeter EM trigger towers with $E_T > 10$ GeV;

  Level 3: one $|\eta| < 3$ electron with $E_T > 20$ GeV meeting loose criteria is found.

After event reconstruction, candidate events are required to have at least two EM objects with transverse energy $E_T > 25$ GeV. For events with more than two EM objects, the two with the highest E_T are used. Both EM objects must be in the fiducial region of the detector, i.e. non-instrumented or poorly instrumented regions of the detector are eliminated. In the central calorimeter (CC), the requirement is $|\eta_{det}| < 1.1$. In the endcap calorimeter (EC), the fiducial region is $1.5 < |\eta_{det}| < 2.4$. Furthermore, we require that at least one of the EM objects be in the CC. Therefore, no EC-EC events are accepted since such a topology is common for QCD dijet processes (a major background to this analysis) but less important in Z' decay. For a Z' with a mass of 700 GeV, this topology cut reduces the total acceptance by about 10%. For QCD events with invariant mass > 400 GeV, about 65% of the events are in the EC-EC topology.

The following electron identification criteria are applied to the two EM candidates to select electrons.

For a "loose" electron:

- EM fraction > 0.9
- isolation < 0.15
- H-Matrix (HMx8): $\chi^2 < 20 + slope \times (E_T - 45\ GeV)$

  The slope is introduced due to the fact that the H-Matrix χ^2 tends to increase as the electron energy increases. The E_T weighted cut compensates this effect and ensures the same efficiency for high energy electrons. The slope (0.023 in CC, 0.043 in EC) is determined from Monte Carlo simulation (Section 6.3.1).

For a "tight" electron:

- All the requirements of a "loose" electron, plus
- A matching global track.

We require that both EM candidates pass loose electron criteria and at least one of them pass tight electron criteria. Therefore, passing events will either have two tight electrons or have one tight electron and one loose electron.

8741 events remain after all these selections. About 97% of these events pass the EM_HI_SH trigger, 98% pass the EM_MX_SH trigger, and 93% pass the 2EM_HI trigger.

In this analysis, we will calculate the ratio of the cross section of $Z' \to ee$ to that of $Z \to ee$. The selection of Z candidates (same sample) is exactly the same as the selection of Z' candidates except that we require the dielectron invariant mass be within 75-105 GeV (mass cut).

Chapter 6

Monte Carlo Simulations

In order to characterize the Z' signals; to model the backgrounds that contaminate the data sample; to calculate the acceptance of detection and the efficiency of data selection; one must rely on computer simulations of the physics processes under study as well as detector effects. The simulations consist of two steps: event generation and detector simulation.

6.1 Event Generator and Full Detector Simulation

The PYTHIA (Version 6.202) event generator is used in this analysis to simulate $p\bar{p}$ interactions at DØ and to simulate particle production and decay. PYTHIA [54] is a program for the generation of high-energy physics events, i.e. for the description of collisions at high energies between elementary particles such as e^+,

e^-, p and $\bar{p}$ in various combinations. Based on theoretical understanding it provides models for a number of the physics aspects of the interactions of interest to us, including hard and soft interactions, parton distributions, initial and final state parton showers, multiple interactions, fragmentation and decay.

The generated events are then processed by detector simulation packages to add detector effects. There are two types of detector simulations in general use at DØ: a Full Detector Simulation and a Fast Monte Carlo.

The Full Detector Simulation [55] is an extremely detailed simulation of the Run II detector based on GEANT [56] modeling of the detector. It consists of two major packages: D0GSTAR as the first phase and D0SIM as the second phase. The D0GSTAR package simulates the behavior of particles passing through the DØ detector. The detector simulation models all aspects of the DØ detector in detail. Detector "hits" are generated during this process just as in the case of real detected collisions. The D0SIM package does the digitization for each subdetector, pileup, overlapping minbias events and adding noise. The output events of the Full Detector Simulation are in the exact same format as those for real data and are reconstructed using the same reconstruction packages as the data.

In brief, the Full Detector Simulation simulates the particles and the interaction of those particles in the detector, including all the details of the detector. However, to run this simulation requires a large amount of computing resources and time, especially for large Monte Carlo samples[1]. For this reason, a faster but less detailed simulation of the detector is necessary.

6.2 Fast Monte Carlo: PMCS

PMCS (Parameterized Monte Carlo Simulation) is a fast simulation of the Run II detector. It is a factor of 2000 times faster than the Full Detector Simulation. PMCS contains several packages to simulate the response of different types of particles. The PMCS_EM package reads Monte Carlo events from generators such as PYTHIA and does the fast simulation for EM particles (electrons, positrons and photons). A brief description of PMCS_EM is provided for completeness, more details can be found at [57].

In PMCS_EM, the following detector effects are simulated: energy scale, energy resolution and angular resolution. Electrons from generators are smeared according to the following formulas:

- For energy smearing:

$$\frac{\sigma_E}{E} = \sqrt{C^2 + \frac{S^2}{E} + \frac{N^2}{E^2}} \tag{6.1}$$

$$E' = a \cdot E + b \tag{6.2}$$

[1]For example, it takes about 1-4 minutes per event on a 2GHz CPU, depending on the physics process.

$$E_{smear} = E' + x \cdot \sigma_E \tag{6.3}$$

where E and E_{smear} are the energy before and after smearing, σ_E is the energy resolution; E' is an intermediate variable, a and b are scale constants; C is the constant term, S the sampling term and N the noise term; x is a random number generated with a standard Gaussian distribution.

- For angular smearing:

$$\eta_{smear} = \eta + x \cdot \sigma_{eta} \tag{6.4}$$

$$\phi_{smear} = \phi + x \cdot \sigma_{phi} \tag{6.5}$$

where η and ϕ are the electron direction at the generator level, and η_{smear} and ϕ_{smear} are the electron direction after smearing. σ_{eta} and σ_{phi} are their resolutions.

In different detector regions, the detector response and effects are also different. As a result, we define nine types of electron according to its position in the detector. Each type has its own set of smearing parameters. The nine types are:

1. In the CC range, but not in the CPS ($1.17 < |\eta| < 1.2$);

2. In the CC range, in the CPS ($|\eta| < 1.17$) and $\phi > 0.02$ radians away from ϕ module boundaries;

3. In the CC range, in the CPS ($|\eta| < 1.17$) and ϕ within 0.02 radians from ϕ module boundaries;

4. Between $1.17 < |\eta| < 1.40$, but not in the FPS;

5. Between $1.40 < |\eta| < 1.45$, where the FPS has only one shower layer;

6. Between $1.45 < |\eta| < 2.46$, where the FPS has two shower layers;

7. Between $2.46 < |\eta| < 4.04$, that are not in the FPS;

8. In the intercryostat region (ICD);

9. In very forward region (with $|\eta| > 4.04$).

Type 4 and type 7 are considered different since for these two regions, the DØ detector has a different tracking system and thus the detector efficiencies are different. Electrons of type 1, 8 and 9 are poorly detected and generally not used in physics analyses. Thus, these three types are not simulated in PMCS_EM package. This analysis also excludes these three types of electrons.

The smearing parameters are tuned with real data (p13) as well as events from the Full Detector Simulation. In Figure 6.1 and Figure 6.2, we compare the invariant mass and p_T distribution of $Z \to ee$ events from PMCS simulation with those observed from data. The agreement is quite good. The parameters for electrons of various types are summarized in Table 6.1.

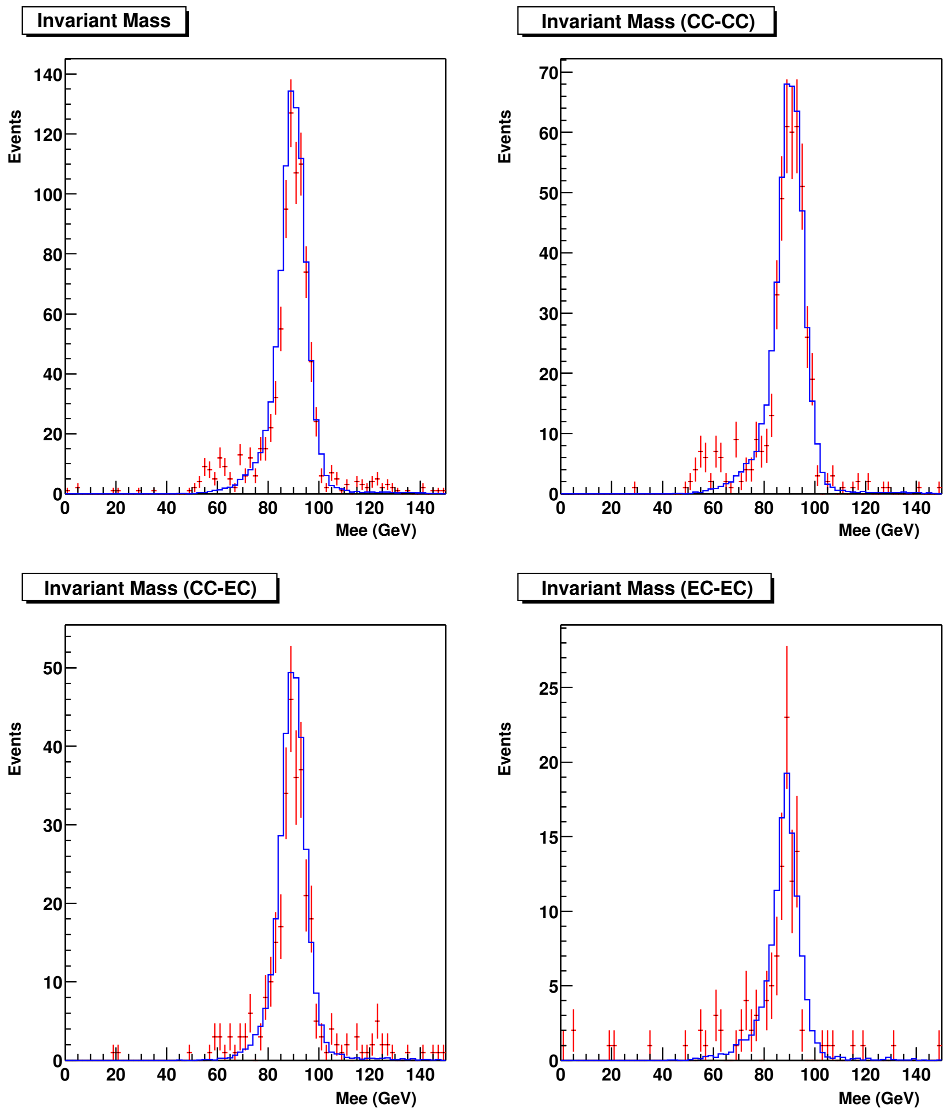

Figure 6.1: *Comparison between PMCS (*line*) and data (*dot*)of the di-electron invariant mass distributions of $Z \rightarrow ee$ events in various topologies: CC-CC (*top right*), CC-EC (*bottom left*), EC-EC (*bottom right*), and all three (*top left*).*

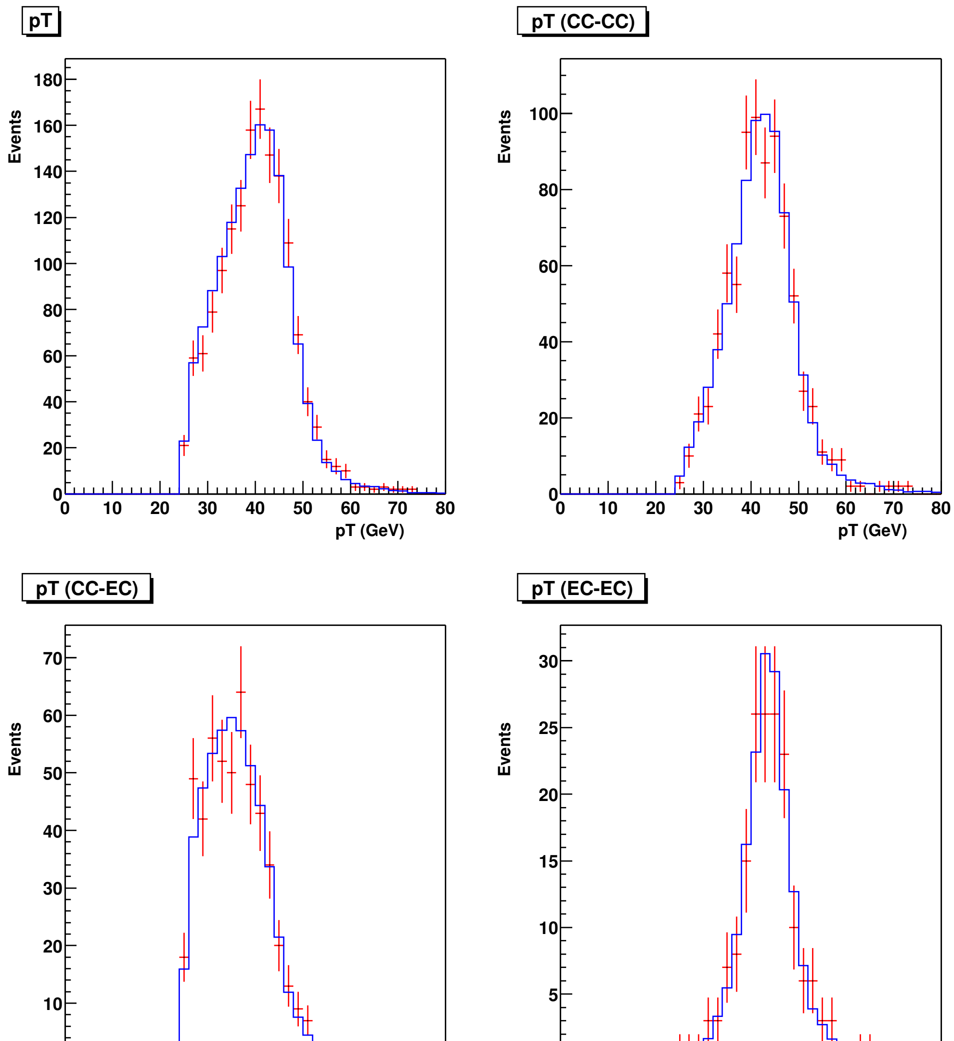

Figure 6.2: *Comparison between PMCS (*line*) and data (*dot*) of the p_T distributions of electrons from $Z \to ee$ events in various topologies: CC-CC (*top right*), CC-EC (*bottom left*), EC-EC (*bottom right*), and all three (*top left*).*

Electron Type	2	3	4	5	6	7
a	1.027	1.018	0.828	0.982	0.997	0.991
b	-1.0	-1.886	-2.82	-0.647	-0.706	0.171
C	0.054	0.054	0.0289	0.005	0.065	0.019
S	0.15	0.342	0.191	0.162	0.206	0.187
N	0.35	0.54	0.036	0.0048	0.125	0.505
σ_η	0.005	0.005	0.004	0.003	0.004	0.006
σ_ϕ	0.003	0.003	0.005	0.005	0.008	0.008

Table 6.1: *Smearing parameters for electrons of various types.*

6.3 Z' Monte Carlo

The shape of Z' signals and the characteristics of electrons from Z' decay are studied using Monte Carlo.

6.3.1 Electrons from Z' decay

$Z' \rightarrow ee$ samples for $m_{Z'}$ = 300 - 900 GeV are generated using PYTHIA, and then go through a full detector simulation (Version mcp13). The same DØ RECO package used for data analysis is used to reconstruct the Monte Carlo events. No electron identification cuts (e.g. EM fraction, isolation, H-Matrix) are used to select electrons since we want an unbiased sample to study these cuts. Instead, a reconstructed EM object is taken as a genuine electron if its position matches the generator-level electron in a window of 0.02×0.02 in $\eta \times \phi$ and its energy matches the generator-level electron within $5\sigma_E$, where σ_E is the electron energy resolution. Finally, the two electrons are also required to pass the same kinematic cut ($E_T > 25$ GeV) and geometric cut (within CC/EC fiducial region and at least one in CC).

The distribution of the electrons' EM fraction, isolation and H-Matrix χ^2 as a function of the electrons' energy for both CC and EC are shown in Fig. 6.3. For the EM fraction and isolation, no significant energy dependency is observed. The distribution of the H-Matrix χ^2 as a function of E_T is fit with a straight line. The slopes are found to be: 0.023 ± 0.002 GeV^{-1} (CC) and 0.043 ± 0.005 GeV^{-1} (EC). An E_T weighted H-Matrix χ^2 cut is used to avoid a bias towards high energy electrons.

Figure 6.4 shows the data/MC comparison of the distribution of electron identification variables between electrons from Monte Carlo and electrons from dielectron events (data), in which both electrons pass the "tight" cuts in Section 5.3. By requiring that both electrons have track match, these dielectron events provide a nearly clean sample of real electrons mainly from $Z/\gamma^* \to ee$ process with little QCD fake background[2]. The distributions of EM fraction and isolation in both CC and EC, and the distribution of HMx8 in EC are quite consistent between the data and the Monte Carlo. However, the HMx8 in CC from data has a slightly higher slope than that from Monte Carlo. The slope in data is found

[2] QCD fake background results from jets being misidentified as electrons (Section 8.3).

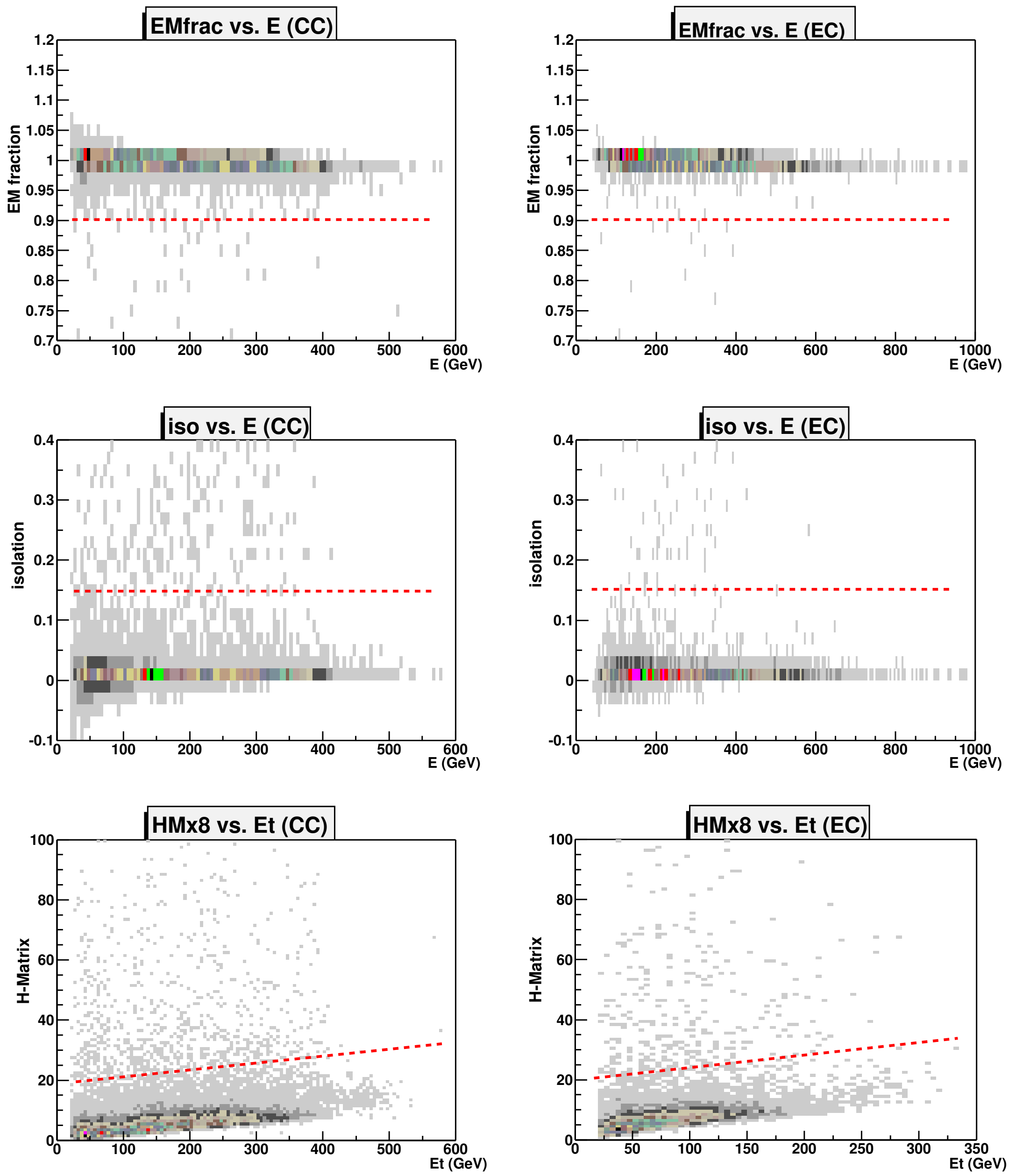

Figure 6.3: *The distribution of electron identification variables* (top to bottom: *EM fraction, isolation and H-Matrix) as a function of electron energy for CC* (left) *and EC* (right)*. The cuts used in this analysis are also shown.*

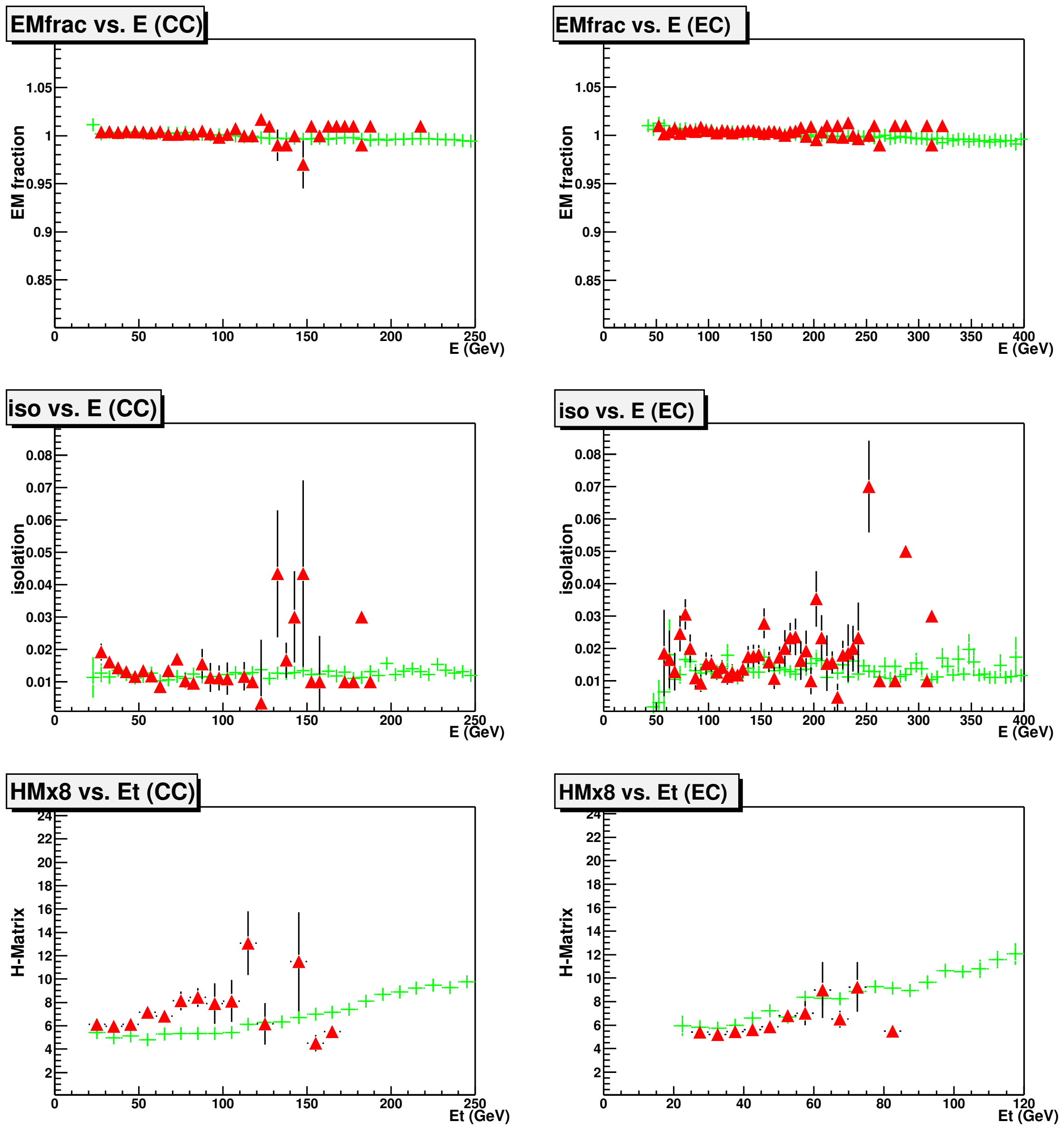

Figure 6.4: *Comparison of the distribution of electron identification variables between electrons from Monte Carlo (*plus sign*) and electrons from data (*triangle*) for CC (*left*) and EC (*right*).* Top to bottom: *EM fraction, isolation and H-Matrix.*

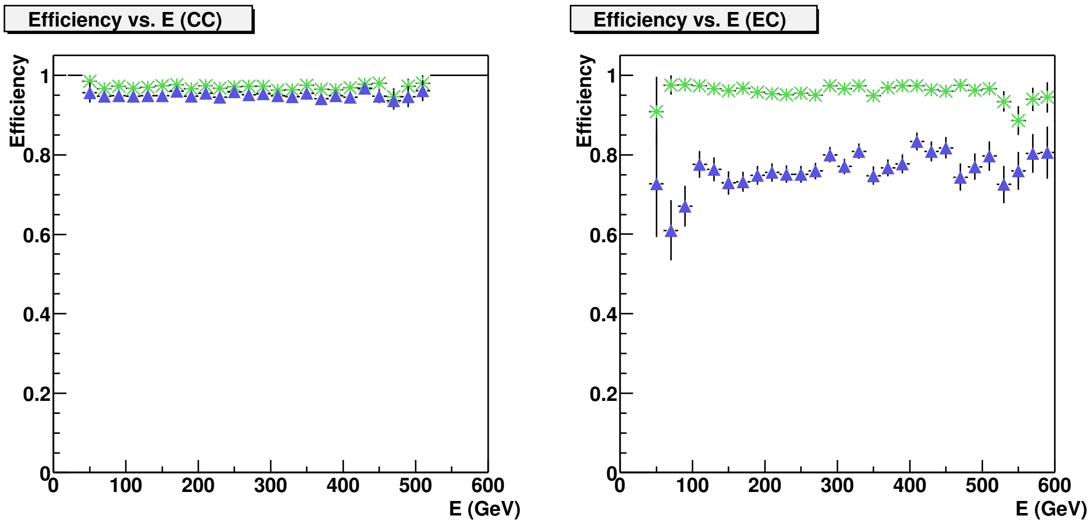

Figure 6.5: *Efficiency (Monte Carlo based) of electron selection cuts as a function of electron energy for loose electrons (*star*) and tight electrons (*triangle*). The left plot is for CC electrons, and the right plot is for EC electrons.*

to be $0.030 \pm 0.006\ \mathrm{GeV}^{-1}$. The effect of this is discussed in details in Appendix A.2, and is found to be negligible.

By counting the fraction of Monte Carlo electrons that could pass the identification cuts used in this analysis (Section 5.3), we obtain the identification efficiencies (Monte Carlo based) as a function of electron energy as shown in Figure 6.5. As shown, these cuts remain efficient for electrons of the whole energy range.

Note that the Monte Carlo based efficiencies are only used to verify that the identification cuts we used have no energy dependency. When calculating cross sections, rather than using the value derived from Monte Carlo, we use the efficiency measured from real data to avoid possible difference between the two numbers.

6.3.2 Interference of Z' with Z and γ^*

The physics underlying $p\bar{p} \to Z' \to ee$ process is exactly the same for Z and Drell-Yan process. Therefore, the actual mechanism is $p\bar{p} \to Z'/Z/\gamma^* \to ee$, i.e. the Z' is not produced independently and there is interference between the Z' and Z,γ^*. However, given current experimental constraints on the Z' mass and Z'-Z mixing (Section 3.2), the effect of the interference is negligible in the direct search of Z' through high energy $p\bar{p}$ collisions.

This is verified by comparing the Z' signals (mass = 500 GeV) with and without the interference effects included, since only the shape of the Z' signal is used in setting the limit (Section 9.3). A combined $Z'/Z/\gamma^*$ sample is generated using PYTHIA with all interference effects included (Figure 6.6(a)). The "interfered" Z' signal is derived by subtracting the Z and Drell-Yan spectrum from the combined spectrum. Another Z' sample is then generated with the interference effects switched off in PYTHIA (Figure 6.6(b)). The two Z' signals are found to be consistent as shown in Figure 6.6(b).

The relative change in the limit using the two Z' signals is found to be less than 0.2%. Thus, we ignore the effect of interference in this analysis.

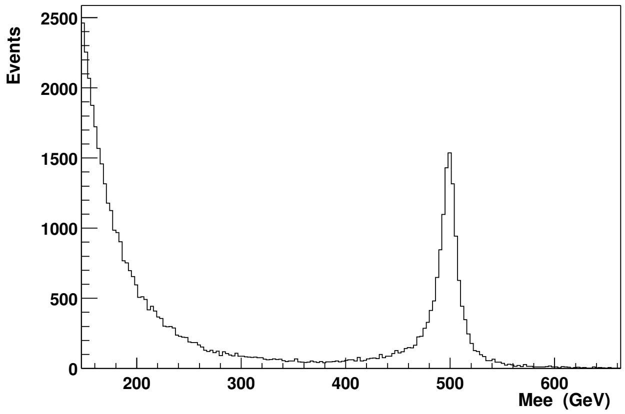

(a)

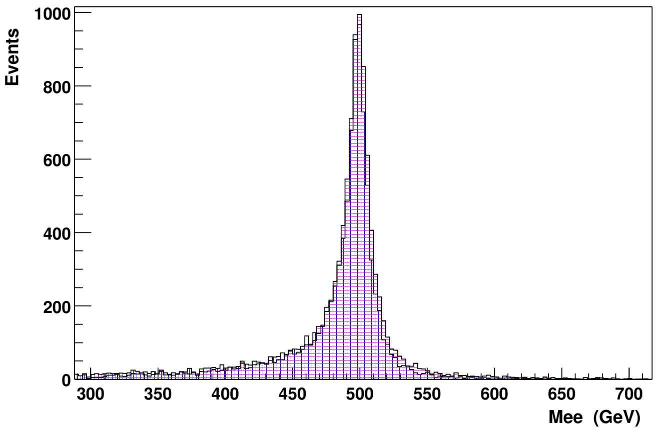

(b)

Figure 6.6: *(a) Invariant mass spectrum of combined $Z'/Z/\gamma^*$ signal. (b) Comparison of Z' signals with interference (*vertical line*) and without interference (*horizontal line*). Signals are normalized to the same luminosity.*

Chapter 7

Efficiencies

The process $p\bar{p} \rightarrow Z' \rightarrow ee$ is identified by the decay electrons. However, only a fraction of the produced events end up being observed and selected. Electrons might escape detection if they are not in the fiducial region of the detector (geometric acceptance) or if their energy is not sufficient to pass the transverse energy E_T cut (kinematic acceptance). The trigger and offline electron identification cuts also cause a fraction of the real signal to be lost (efficiency). In this chapter, we discuss the measurement of these detection efficiencies.

7.1 Acceptance

The acceptance is defined as the ratio of the number of events which pass the kinematic and geometric requirements to the total number of events produced. It is estimated using Monte Carlo simulation.

For the Z' acceptance calculation, $N_{gen} = 50,000$ $p\bar{p} \rightarrow Z' \rightarrow ee$ events with $m_{Z'} = 300, 400, 500, 600, 700, 800, 900$ GeV are generated using PYTHIA and PMCS (Version v01-97-00) fast detector simulation. The Z' width is set to scale with the Z' mass, $\Gamma_{Z'} = (m_{Z'}/m_Z)\Gamma_Z$. The top quark mass is set to the combined DØ and CDF measurement ($m_t = 174.3$ GeV).

The acceptance is then computed as:

$$\mathcal{A} = \frac{N_{pass}}{N_{gen}} \tag{7.1}$$

where N_{pass} is the number of events that pass following cuts as discussed in Section 5.3: both electrons with $E_T > 25$ GeV; both in the detector fiducial region and at least one in CC. The statistical error ($\sim$0.2%) is computed by:

$$\delta_{\mathcal{A}} = \sqrt{\frac{\mathcal{A} \cdot (1 - \mathcal{A})}{N_{gen}}} \tag{7.2}$$

Similarly, 50,000 $p\bar{p} \rightarrow Z \rightarrow ee$ events are generated to calculate the Z acceptance. Note that, in addition to the kinematic and geometric cuts, there is an mass window cut to select Z events: the di-electron invariant mass must satisfy $75 < M_{ee} < 105$ GeV (i.e. within the Z peak window).

The acceptance of Z events and Z' events at various masses are summarized in

	CC-CC	CC-EC	Total
Z	0.199 ± 0.015	0.143 ± 0.010	0.342 ± 0.006
Z' (300 GeV)	0.405 ± 0.016	0.197 ± 0.009	0.602 ± 0.018
Z' (400 GeV)	0.458 ± 0.025	0.158 ± 0.012	0.616 ± 0.016
Z' (500 GeV)	0.497 ± 0.020	0.132 ± 0.008	0.629 ± 0.017
Z' (600 GeV)	0.521 ± 0.022	0.109 ± 0.007	0.630 ± 0.021
Z' (700 GeV)	0.539 ± 0.026	0.092 ± 0.008	0.631 ± 0.020
Z' (800 GeV)	0.548 ± 0.015	0.080 ± 0.007	0.628 ± 0.013
Z' (900 GeV)	0.538 ± 0.015	0.078 ± 0.007	0.616 ± 0.012

Table 7.1: *Acceptances of Z and Z'.*

Table 7.1. The quoted errors are the statistical errors and systematic errors added in quadrature. The systematic errors are estimated below. The Z' acceptances ($\mathcal{A}_{Z'}$) for different masses are also plotted in Figure 7.1.

7.1.1 Systematic Uncertainties

There are four major sources that contribute to the systematic uncertainty on the acceptance, $\delta\mathcal{A}/\mathcal{A}$.

The largest uncertainty is due to the uncertainty in the parton distribution function. It is estimated by using four different distribution functions: CTEQ4L, MRSD-, CTEM3M and GRV94H0 [58]. The uncertainty is found to be 1.5% for Z, and 2.0-3.5% for various Z' masses.

The uncertainty due to the QED radiative corrections is estimated by varying the cone size used in reconstruction ($\mathcal{R} = \sqrt{\Delta\eta^2 + \Delta\phi^2} = 0.4$) to decide whether

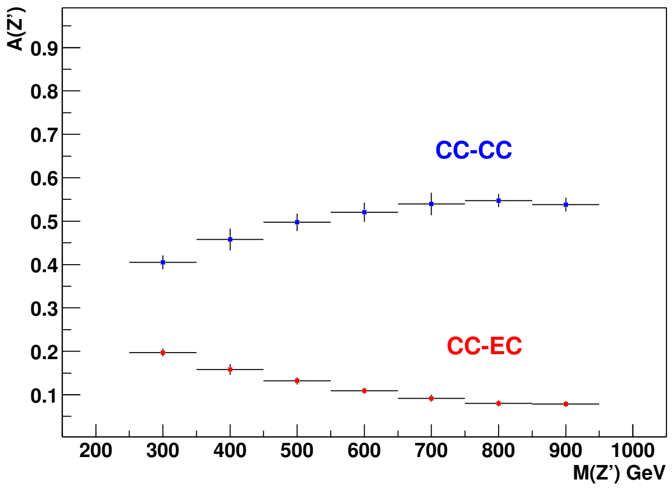

Figure 7.1: *Acceptance $\mathcal{A}_{Z'}$ for Z' of various masses.*

the radiated photon's energy should be merged with its associated electron. The cone variation of $\delta\mathcal{R} = \pm 0.1$ [59] leads to a 0.3% change in Z acceptance and a 0.5% change in Z' acceptance.

The EM energy scale is varied within its measured error ($\pm 1\%$), and the change in the acceptance is used to estimate its contribution to the uncertainty. The uncertainty due to the EM energy scale is found to be 0.7% for Z. Similarly, the uncertainty due to the EM energy smearing is found to be 0.4% for Z events. The last two sources have negligible effect on the Z' acceptance.

The systematic uncertainty in the acceptance ratio $\mathcal{A}_{Z'}/\mathcal{A}_Z$ due to these four sources (pdf, QED, EM energy scale and smearing) are found to be $\sim$3%, 0.3%, 0.7% and 0.4% respectively. All values are relative percentage, i.e. $\delta\frac{\mathcal{A}_{Z'}}{\mathcal{A}_Z}/\frac{\mathcal{A}_{Z'}}{\mathcal{A}_Z}$.

7.2 Efficiencies

The trigger and offline selection cuts used in identifying genuine electrons and reducing the background cause a fraction of real signal events to be lost. This section concerns the measurement of the efficiencies of these cuts using data.

$Z \to ee$ events are well suited for this task: by requiring the invariant mass to be close to M_Z, and by imposing a tight electron identification criteria on one of the electrons (*tag*), the other electron (*probe*) serves as an ideal sample of unbiased electrons with little background [60].

7.2.1 Trigger Efficiency

The trigger efficiency for EM triggers is derived from $Z \to ee$ candidates using the tag/probe method. We start with events having two EM objects with $E_T > 15\ GeV, EMfraction > 0.9, isolation < 0.15, HMx8 < 20\ (weighted)$ and with both EM objects in the fiducial region. The highest E_T one is used as the "tag" electron and is required to have $E_T > 25$ GeV, a matched track, and pass the EM_HI_SH or EM_MX_SH triggers. Here the definition of an offline electron passing a specific trigger means that: 1. The electron's energy and position pass the trigger's threshold; 2. It has a matched trigger object at all trigger levels. The matching between the electron and the trigger object must satisfy:

- Level 1: $\Delta\phi < 0.4$
- Level 2: $\Delta\mathcal{R} = \sqrt{\Delta\eta^2 + \Delta\phi^2} < 0.4$
- Level 3: $\Delta\mathcal{R} = \sqrt{\Delta\eta^2 + \Delta\phi^2} < 0.4$

At Level 1, we use $\Delta\phi$ because only ϕ information is available in the reconstructed p13 data. 5714 events remain after the tagging requirements.

Now we apply the two trigger-passing criteria to the "probe" electrons, i.e. passing the trigger's threshold and having a matched trigger object. By counting the fraction of probe electrons that could pass these criteria, we can get the efficiency for that specific trigger. Figure 7.2 shows the trigger efficiency as a function of electron p_T for EM_HI_SH or EM_MX_SH triggers.

For electrons from Z decay, the average trigger efficiency is found to be

$$\epsilon_{trig} = 0.966 \pm 0.010$$

The total efficiency for a dielectron event to pass the trigger is then computed as:

$$1 - (1 - \epsilon_{trig})^2$$

For $Z \to ee$ events, this gives 0.999. For $Z' \to ee$ events, this efficiency is close to 1.

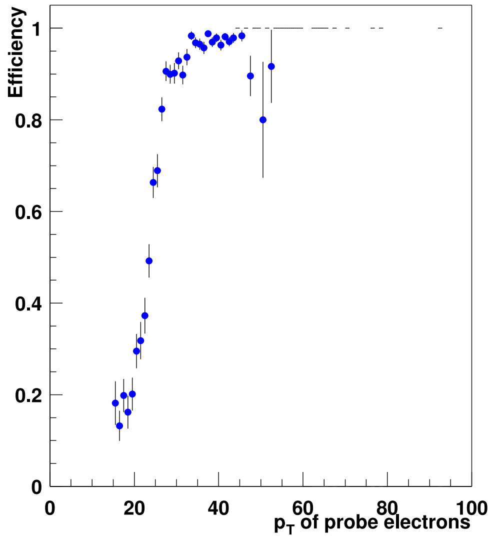

Figure 7.2: *Trigger turn-on curve for EM_HI_SH or EM_MX_SH triggers.*

7.2.2 Electron Identification (EMID) Efficiency

The EMID efficiency is also measured using events from Z decays. However, the algorithm is different from the simple tag/probe method used for the trigger efficiency calculation.

We start with events with two "probe" electrons satisfying the following criteria: 1. Both probes have $E_T > 25$ GeV and are in the fiducial region; 2. At least one of the probes passes tight cuts ("tag") of $EMfraction > 0.9, isolation < 0.15, HMx8 < 20$ $(weighted)$ and has a matched track. The tight cuts used for the tag electrons must be tighter than the cuts under study.

The EMID efficiency can then be computed by:

$$\epsilon_{cut} = \frac{2(tt) + (tp)}{2(tt) + (tp) + (tf)} \tag{7.3}$$

where

- tt = numbers of events where both electrons pass the tight cuts (therefore pass the cuts under study);
- tp = number of events where one electron passes the tight cuts and the other passes the cuts under study but fails the tight cuts;
- tf = number of events where one electron passes the tight cuts and the other electron fails the cuts under study (and therefore fails the tight cuts as well).

Note that events with two tag electrons are counted twice. Here the cuts under study are the selection cuts for a "loose" electron (Section 5.3): $EMfraction > 0.9, isolation < 0.15, HMx8 < 20\ (weighted)$.

Equation 7.3 can be verified as follows. The total number of probe electrons N can be divided into N_{pass} and N_{fail}, with N_{tag} a subset of N_{pass}, as illustrated in Figure 7.3. With these definitions, the following relations hold:

- $\epsilon_{tag} = N_{tag}/N$

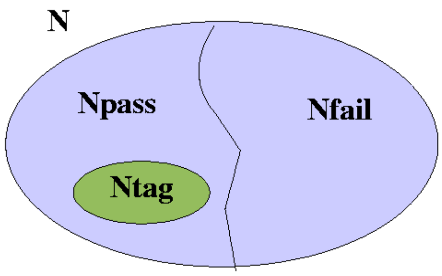

Figure 7.3: *Illustration of sample sets used to measure the EMID efficiency.*

- $\epsilon_{pass} = N_{pass}/N$
- $\epsilon_{fail} = N_{fail}/N = (N - N_{pass})/N = 1 - \epsilon_{pass}$
- $\epsilon_{pass(but-fail-tag)} = (N_{pass} - N_{tag})/N = \epsilon_{pass} - \epsilon_{tag}$

Assuming there are no correlations between the electrons, we can use the above relations to calculate following efficiencies:

- $\epsilon_{tt} = \epsilon_{tag}^2$
- $\epsilon_{tp} = 2\epsilon_{tag}(\epsilon_{pass} - \epsilon_{tag})$
- $\epsilon_{tf} = 2\epsilon_{tag}(1 - \epsilon_{pass})$

Therefore, Equation 7.3 reduces to:

$$\begin{aligned}
\epsilon_{cut} &= \frac{2(tt) + (tp)}{2(tt) + (tp) + (tf)} = \frac{2\epsilon_{tag}^2 + 2\epsilon_{tag}(\epsilon_{pass} - \epsilon_{tag})}{2\epsilon_{tag}^2 + 2\epsilon_{tag}(\epsilon_{pass} - \epsilon_{tag}) + 2\epsilon_{tag}(1 - \epsilon_{pass})} \\
&= \frac{2\epsilon_{tag}\epsilon_{pass}}{2\epsilon_{tag}\epsilon_{pass} + 2\epsilon_{tag} - 2\epsilon_{tag}\epsilon_{pass}} = \epsilon_{pass}
\end{aligned}$$

where ϵ_{pass} is indeed the efficiency of our cut, i.e. the number of electrons passing the cuts under study divided by the total number of probe electrons.

The advantage of this algorithm is that it counts the number of events rather than the number of electrons. Therefore, it allows us to subtract non-Z backgrounds from the sample and use nearly pure Z events.

Figure 7.4 shows the invariant mass distribution of events satisfying the $2(tt)+(tp)$ criteria and events satisfying the $2(tt)+(tp)+(tf)$ criteria for the CCCC topology. Figure 7.5 shows similar distributions for the ECEC topology. Recall that some events may be plotted twice. The expected non-Z backgrounds are also shown in the plots. The background spectrum is obtained by using events with two EM objects that both have $HMx8 > 35$ ("reversing" the EMID cut). The normalization of the background is obtained by fitting it to the data in the non-Z region, i.e. the two sideband regions ([50, 75] and [105, 130] GeV) on either side of the Z peak[1].

The numerator in Equation 7.3 is then the number of entries between 80 and 100 GeV after subtracting background in the $2(tt)+(tp)$ plot. Similarly, the

[1]The fit in EC-EC topology has larger errors because of events with mis-reconstructed invariant mass. Due to the low tracking efficiency in EC, most electrons' directions are determined by the calorimeter only, which gives larger errors than the tracking system, especially for low energy clusters.

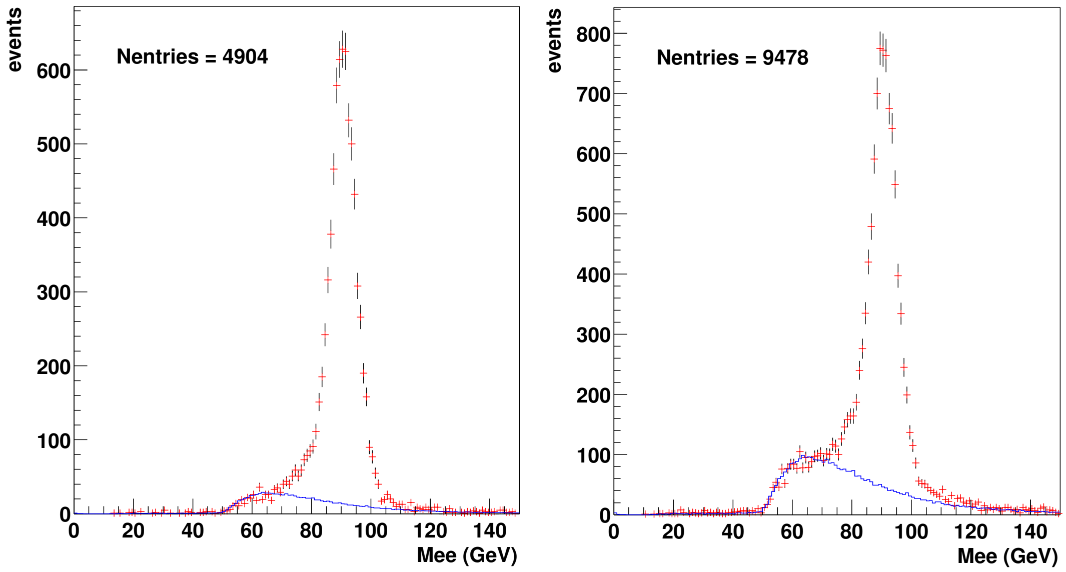

Figure 7.4: *The 2(tt)+(tp) (*left*) and 2(tt)+(tp)+(tf) (*right*) distributions for CCCC events. The points are data. The line is the expected non-Z background.*

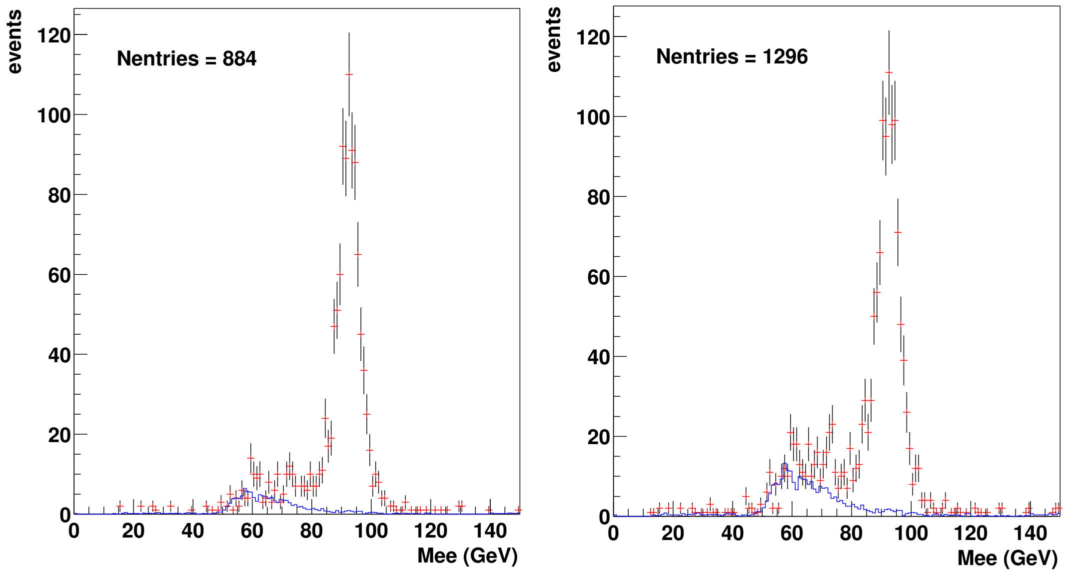

Figure 7.5: *The 2(tt)+(tp) (*left*) and 2(tt)+(tp)+(tf) (*right*) distributions for ECEC events. The points are data. The line is the expected non-Z background.*

denominator in Equation 7.3 is then the number of entries between 80 and 100 GeV after subtracting background in the $2(tt)+(tp)+(tf)$ plot. Here we have applied a mass window cut (80-100 GeV) to further purify the Z events. The measured EMID efficiencies are:

$$\epsilon^{CC} = 0.826 \pm 0.016 \qquad \text{(for CC)}$$

$$\epsilon^{EC} = 0.900 \pm 0.042 \qquad \text{(for EC)}$$

The quoted error includes both statistical and systematic errors (added in quadrature). The statistical errors are 0.5% for CC and 0.9% for EC. The systematic errors are estimated by varying the number of background subtracted within their normalization errors (from fit). The systematic errors are found to be 1.9% for CC and 4.6% for EC.

7.2.3 Tracking Efficiency

The track matching efficiency ϵ_{trk} is computed using events with two *good* electrons ($E_T > 25\,GeV, EMfraction > 0.9, isolation < 0.15, HMx8 < 20\,(weighted)$ and in fiducial region). The efficiency is calculated as the ratio of the number of electrons in the Z peak (80-100 GeV) that have track match to the total number of electrons in the Z peak (twice the number of Z events).

Let N_0, N_1 and N_2 denote the numbers of Z events (background subtracted) in which none, one or both electron(s) are matched to a track respectively, the efficiency is then:

$$\epsilon_{trk} = \frac{N_1 + 2N_2}{2(N_0 + N_1 + N_2)} \tag{7.4}$$

We plot the combined distribution of $N_1 + 2N_2$ and $N_0 + N_1 + N_2$ for CCCC events (Figure 7.6) and ECEC events (Figure 7.7) respectively. This is similar to what was done in the previous section. Same background estimation and subtraction methods are also applied here. By counting the number of background subtracted entries from 80 to 100 GeV in the $N_1 + 2N_2$ and $N_0 + N_1 + N_2$ plots, the track matching efficiency is computed to be:

$$\epsilon_{trk}^{CC} = 0.897 \pm 0.023 \qquad \text{(for CC)}$$

$$\epsilon_{trk}^{EC} = 0.512 \pm 0.032 \qquad \text{(for EC)}$$

The efficiency for EC is much smaller because the central tracking system (CFT and SMT) is less instrumented in this region. The quoted error includes both statistical and systematic errors (added in quadrature). The statistical errors are 0.3% for CC and 0.7% for EC. The systematic errors are estimated by varying the number of subtracted background within their normalization errors (from fit). The systematic errors are found to be 2.5% for CC and 6.2% for EC.

7.3 Overall Efficiency

The measured efficiencies are summarized in Table 7.2.

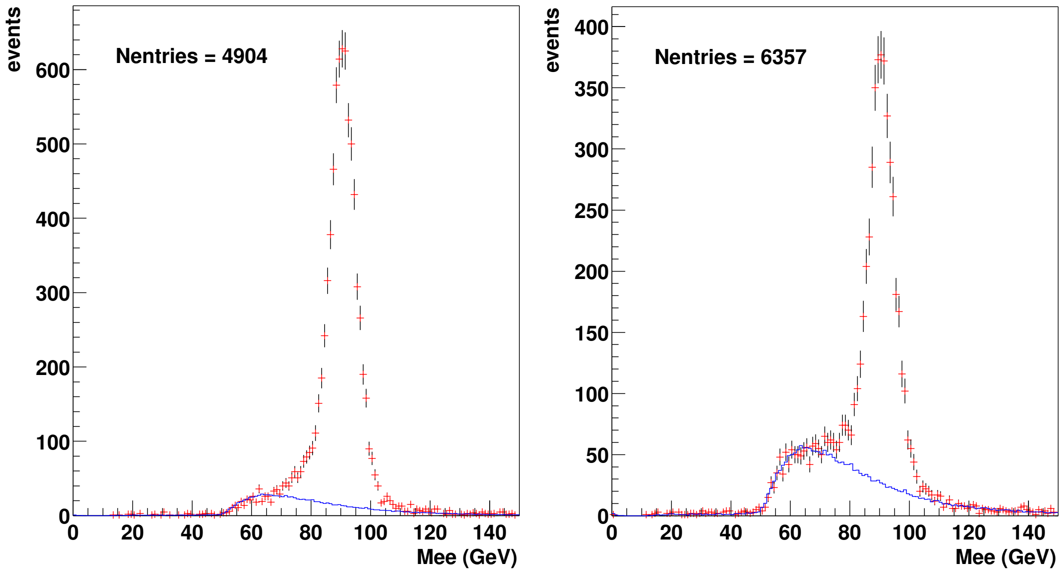

Figure 7.6: *The* $N_1 + 2N_2$ *(*left*) and* $N_0 + N_1 + N_2$ *(*right*) distributions for CCCC events. The points are data. The line is the expected non-Z background.*

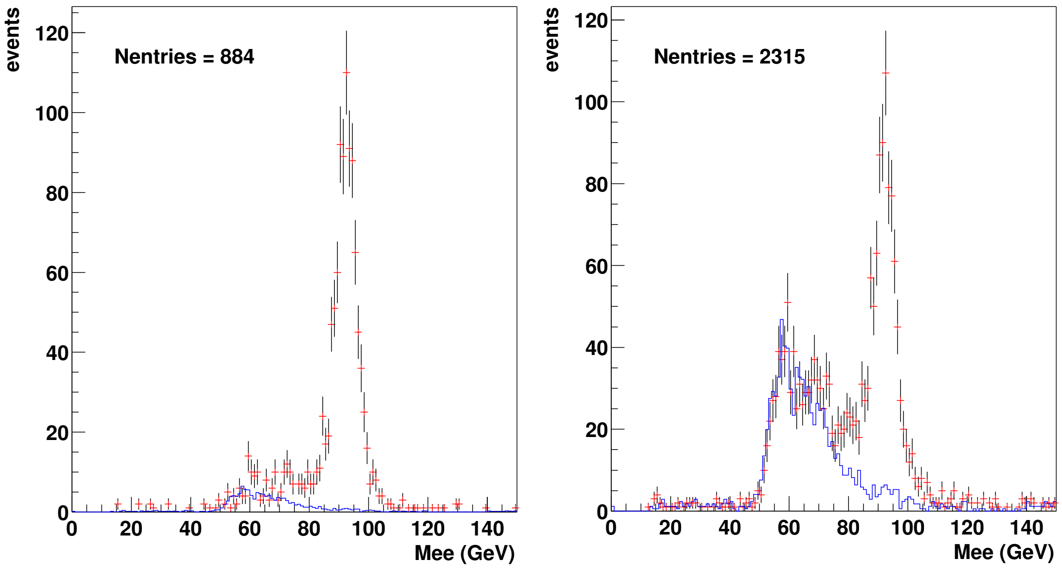

Figure 7.7: *The* $N_1 + 2N_2$ *(*left*) and* $N_0 + N_1 + N_2$ *(*right*) distributions for ECEC events. The points are data. The line is the expected non-Z background.*

	CC	EC
EMID efficiency	0.826 ± 0.016	0.900 ± 0.042
spatial track matching	0.897 ± 0.023	0.512 ± 0.032
trigger efficiency	0.966 ± 0.010	

Table 7.2: *Summary of selection efficiencies.*

Having measured the acceptance and selection efficiencies, we can now go ahead and calculate the overall efficiency, i.e. the fraction of all the events produced from $p\bar{p} \to Z/Z' \to ee$ that end up in our final data sample.

The overall efficiency is given by:

$$\begin{aligned} \epsilon = \quad & A_{CCCC} \cdot (1-(1-\epsilon_{trig})^2) \cdot \epsilon^{CC} \cdot \epsilon^{CC} \cdot (1-(1-\epsilon_{trk}^{CC})^2) \\ & + A_{CCEC} \cdot (1-(1-\epsilon_{trig})^2) \cdot \epsilon^{CC} \cdot \epsilon^{EC} \cdot (1-(1-\epsilon_{trk}^{CC})(1-\epsilon_{trk}^{EC})) \end{aligned} \tag{7.5}$$

where A_{CCCC} and A_{CCEC} are the acceptances for the different topologies, ϵ_{trig} is the trigger efficiency, ϵ^{CC} and ϵ^{EC} are the electron identification efficiencies for CC and EC respectively, ϵ_{trk}^{CC} and ϵ_{trk}^{EC} are the spatial track matching efficiencies for CC and EC respectively.

For $Z \to ee$ events, the overall efficiency is:

$$\epsilon_Z = 0.235 \pm 0.014$$

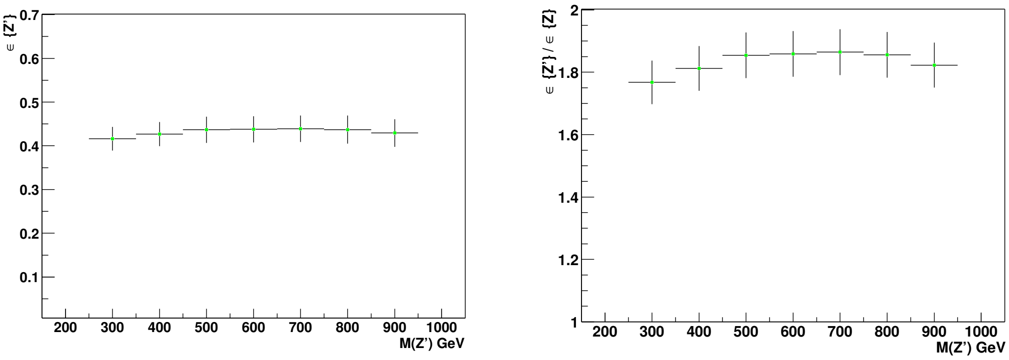

Figure 7.8: *Overall efficiency* $\epsilon_{Z'}$ *(*left*) and efficiency ratio* $\epsilon_{Z'}/\epsilon_Z$ *(*right*) for* Z' *of various masses.*

For the CC-CC topology, it is $\epsilon_Z^{CCCC} = 0.134 \pm 0.006$. For the CC-EC topology, it is $\epsilon_Z^{CCEC} = 0.101 \pm 0.006$.

The overall efficiency for Z' events ($\epsilon_{Z'}$) and the efficiency ratio ($\epsilon_{Z'}/\epsilon_Z$) for various Z' masses are plotted in Figure 7.8.

A large part of the uncertainty in the overall efficiency cancels in the ratio $\epsilon_{Z'}/\epsilon_Z$. The un-cancelled part is due to the difference in CCCC/CCEC mixture between Z' and Z events. This part is estimated, by varying measured efficiencies by $\pm 1\sigma$, to be 2.4% (largest difference). Another major source of the uncertainty in $\epsilon_{Z'}/\epsilon_Z$ comes from the uncertainty in the acceptance ratio $\mathcal{A}_{Z'}/\mathcal{A}_Z$ as discussed in Section 7.1.

Chapter 8

Backgrounds

The major backgrounds in the Z' sample are dielectron events from physics processes, such as Z/Drell-Yan production, and from QCD events in which jets are misidentified as isolated electrons.

8.1 Z/Drell-Yan Background

The principal physics background to the Z' sample is the Z/Drell-Yan production and decay:

$$q\bar{q} \rightarrow Z/\gamma^{*} \rightarrow ee \quad (+jet)$$

This process is simulated using PMCS. 200k events were generated with PYTHIA using the CTEQ4L parton distribution function. To ensure enough statistics in the high mass region, samples are generated in different mass ranges and then joined together based on their cross sections. The same kinematic and geometric cuts are applied to this Monte Carlo sample.

The cross section produced by PYTHIA is only to leading order (LO). A K-factor is applied as a function of the dielectron mass to account for next to leading order (NLO) and next to next to leading order (NNLO) calculations as described in [61]. The K-factor is calculated using a program provided by the author of [61], and the results are shown in Figure 8.1. The uncertainty of the K-factor, mainly due to the uncertainty in parton distribution functions, is found to be 5% [62].

8.2 Other Physics Backgrounds

Other physics processes besides $Z/\gamma^* \to ee$ also produce dielectron events, or have a photon and an electron in their final state, where the photon can be identified as a "loose" electron.

Processes producing dielectrons are $t\bar{t}$ production with the Ws decaying into electrons ($t\bar{t} \to ee$) and boson pair production ($WW \to ee$, $WZ \to ee$, $ZZ \to ee$). Processes involving a photon plus an electron include $W\gamma \to e$"e" and $Z\gamma \to e$"e".

These processes are generated using PYTHIA with the CTEQ4L parton distribution function. Detector effects are simulated using PMCS. Kinematic and geometric cuts are applied. Figure 8.2 shows the "dielectron" invariant mass dis-

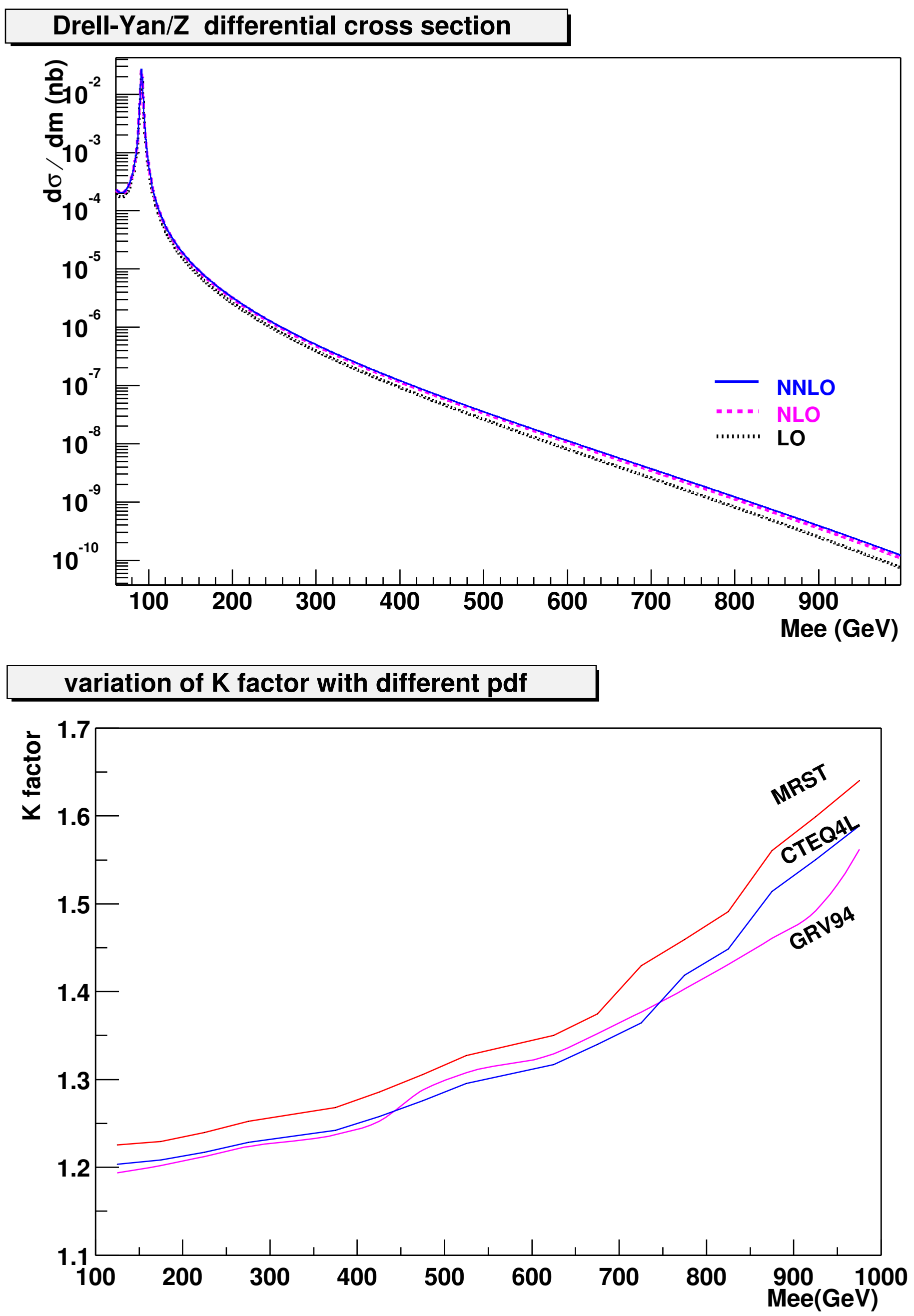

Figure 8.1: (upper) *Z/Drell-Yan differential cross section at* $\sqrt{s} = 1.96$ *GeV;* (lower) *K-factor as a function of dielectron mass for various parton distribution functions: CTEQ4L, MRST, GRV94.*

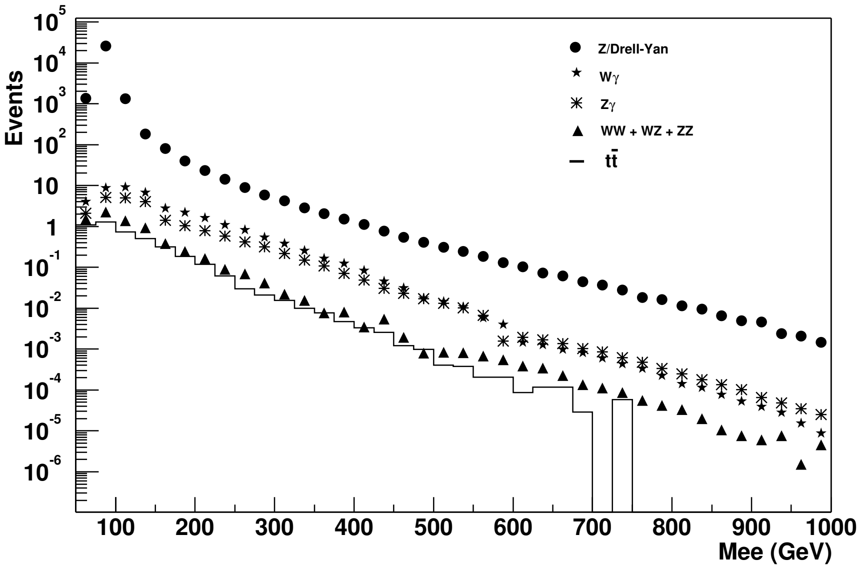

Figure 8.2: *The invariant mass distribution from various physics processes.*

tribution from various physics processes. The number of events is normalized to the same luminosity. The difference in selection efficiency between dielectron events and electron plus photon events are also taken into account[1].

The invariant mass spectrum expected from all physics processes is shown in Figure 8.3.

[1]Dielectron events will pass our selection cuts if either electron has a track match. Electron plus photon events will be selected when the electron has a track match.

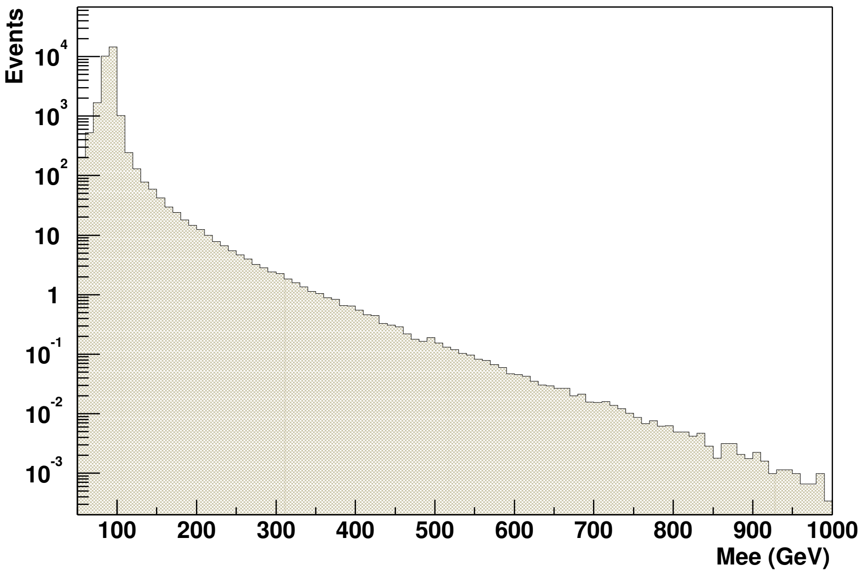

Figure 8.3: *Expected dielectron mass spectrum from all physics processes.*

8.3 Background due to Misidentification of Jets

A "fake" background results from jets being misidentified as electrons. A jet can be formed with most of its energy carried by an isolated π^0 or η which subsequently decays into a pair of spatially close photons. The photon pair will be unresolved in the EM section of the calorimeter and will be reconstructed as a single photon. This photon will pass the "loose" electron identification cuts, since these cuts do not require an associated track. Tracks can be associated with the EM object formed by the photon pair by two mechanisms. If one of the photons converts to e^+e^-, these electrons will form tracks which could be directly associated with the EM object. The other process is due to charged hadrons from the jet forming tracks which overlap with the EM object. As a result, this photon is also possible to pass the "tight" electron identification cuts.

Two sources of QCD fake backgrounds are considered in this analysis. The dominant source of the fake background is due to multijet events, in which one of the jets is misidentified as a "loose" electron and another jet is misidentified as a "tight" electron. Another source is due to direct photon (γ+jet) events, in which the photon satisfies the "loose" electron cuts and the jet is misidentified as a "tight" electron.

We use a di-EM data sample to estimate the expected backgrounds from these two sources. The criteria applied in the EM object reconstruction are very loose. Thus, the EM objects are dominated by electromagnetic jets since the QCD multijet cross section greatly exceeds the cross section of real electrons.

The probability that an electromagnetic jet is misidentified as an electron is called the *fake rate*. The fake rate is measured using a completely uncorrelated sample of single-EM data.

8.3.1 Fake Rate

The following criteria are used to select single-EM events for the fake rate calculation. The events must:

- Pass the 2EM_HI trigger
- Have only one EM object
- The EM object must have $E_T > 25$ GeV and be in the detector fiducial region
- Have a small missing E_T: $\not\!\!E_T < 15$ GeV (to remove $W \to e\nu$ events)

Most physics processes producing real electrons and photons are removed by these requirements.

To first order, the probability that an EM object passes the electron identification cuts, i.e. fake rate, is given by:

$$P_{em \to e_l} = N_{e_l}/N_{em}$$

$$P_{em \to e_t} = N_{e_t}/N_{em}$$

where N_{em} is the total number of EM objects in the sample, N_{e_l} and N_{e_t} are the number of fake electrons passing "loose" and "tight" cuts respectively. These numbers are listed in Table 8.1. We have $P_{em \to e_l} \approx 21\%$ in CC and 25% in EC, and $P_{em \to e_t} \approx 3\%$ in CC and 2% in EC.

The majority of the events in the single-EM sample are from QCD multijet production where one jet is reconstructed as an EM object. A small number of

	N_{em}	N_{e_l}	N_{e_t}
CC	79139	17081	2314
EC	76621	19342	1336

Table 8.1: *Total number of EM objects in the sample and number of EM objects passing "loose" and "tight" cuts.*

the events are from the γ+jet process where the EM object is actually the direct photon. The direct photon contamination is on the order of

$$\frac{N_\gamma}{N_{jet}} = \frac{\sigma_{\gamma jet}}{\sigma_{dijet} \cdot 2P_{j\to em}}$$

where σ_{dijet} and $\sigma_{\gamma jet}$ are the cross section of multijet and γ+jet processes; $P_{j\to em}$ is the probability that a jet may be reconstructed as an EM object, and is estimated[2] to be ~2.5% in CC and ~ 6.0% in EC. The fraction of direct photon contamination, f_γ, at different E_T ranges is shown in Table 8.2.

E_T(GeV) Range		20-40	40-80	80-160	160-320	320-
$\sigma_{dijet}/\sigma_{\gamma jet}$		2576	1516	807	359	155
f_γ (single-EM)	CC	0.8%	1.3%	2.4%	5.3%	11%
	EC	0.3%	0.5%	1.0%	2.3%	5.1%
$f_{\gamma jet}$ (di-EM)	CC-CC	1.5%	2.6%	4.7%	10%	21%
	CC-EC	1.0%	1.6%	3.0%	6.5%	14%

Table 8.2: *The fraction of direct photon events, f_γ, in the single-EM sample and the fraction of γ+jet events, $f_{\gamma jet}$, in the di-EM sample.*

[2]From [63], the probability of a jet passing the same identification cuts ($P_{j\to e_l}$) is roughly 0.5% in CC and 1.5% in EC. We can estimate this probability as $P_{j\to em} \sim P_{j\to e_l}/P_{em\to e_l}$.

The fake rate is then calculated as:

$$P_{em \to e_l} = (N_{e_l} - N_{em} f_\gamma)/(N_{em} - N_{em} f_\gamma) \tag{8.1}$$

$$P_{em \to e_t} = N_{e_t}/N_{em} \tag{8.2}$$

The four types of fake rates as a function of EM object's E_T are:

$$P^{CC}_{em \to e_l}(E_T) = (0.230 \pm 0.006) + (0.00040 \pm 0.00017) \cdot E_T \tag{8.3}$$

$$P^{EC}_{em \to e_l}(E_T) = (0.251 \pm 0.007) + (0.00088 \pm 0.00022) \cdot E_T \tag{8.4}$$

$$P^{CC}_{em \to e_t}(E_T) = (0.021 \pm 0.002) + (0.00019 \pm 0.00007) \cdot E_T \tag{8.5}$$

$$P^{EC}_{em \to e_t}(E_T) = (0.016 \pm 0.002) + (0.00003 \pm 0.00007) \cdot E_T \tag{8.6}$$

The results are also shown in Figure 8.4.

Figure 8.5 shows the effect of triggers on the value of the fake rate. The EM_HI trigger requires a 30 GeV EM object at Level 3. The EM_HI_SH trigger has a tighter requirement on shower shape at Level 3. These requirements will bias the fake rate. As a result, the 2EM_HI trigger is used both for measuring fake rate and for calculating background spectrum.

Due to the lack of statistics (Figure 8.4), the value of fake rate at high E_T (e.g. $E_T > 120$ GeV) is determined by the extrapolation given by Equation 8.3-

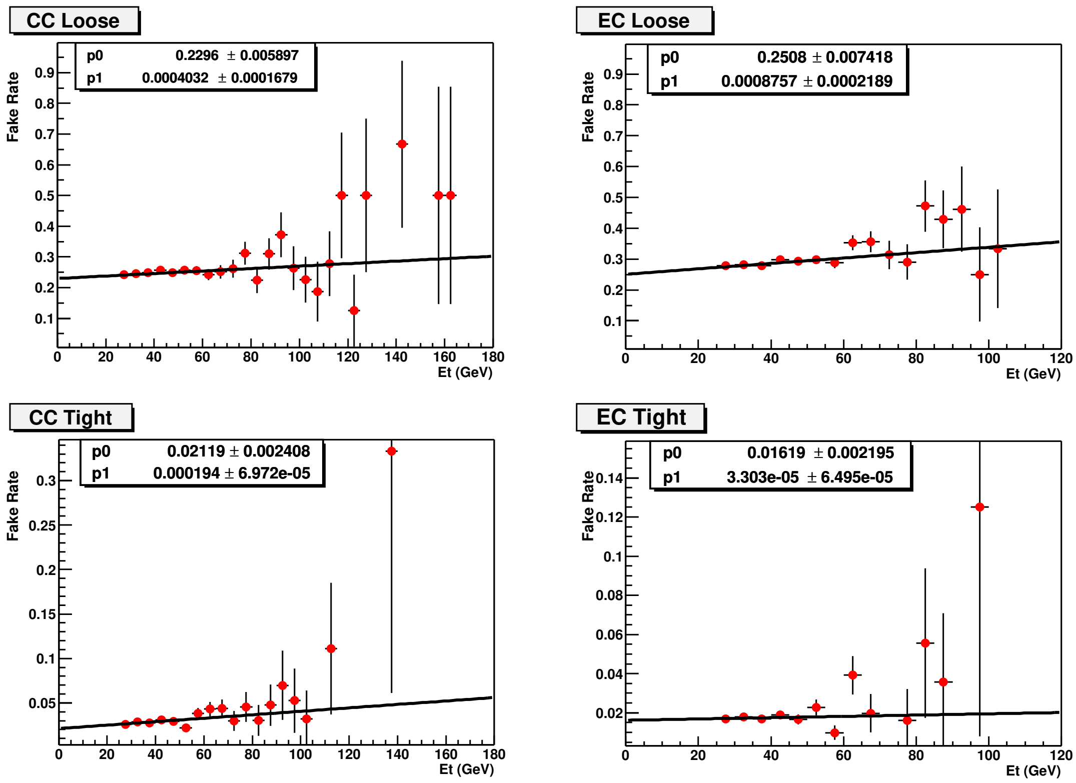

Figure 8.4: *Fake rate as a function of EM object's E_T for passing "loose" cuts in CC (*top left*), "loose" cuts in EC (*top right*), "tight" cuts in CC (*bottom left*), and "tight" cuts in EC (*bottom right*).*

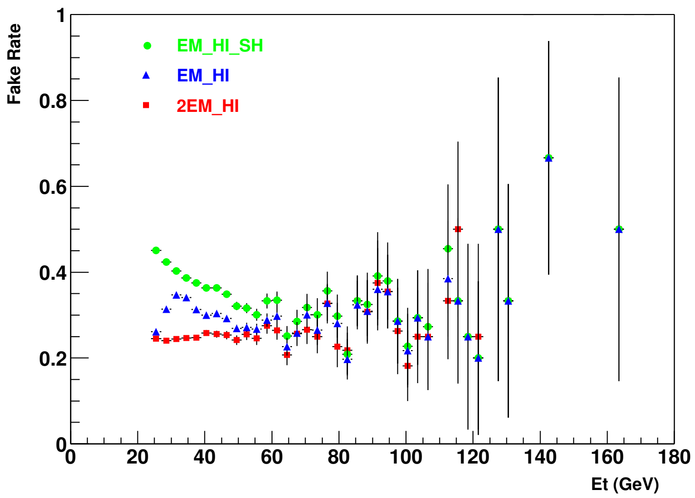

Figure 8.5: *Fake rate using different triggers: EM_HI_SH (*top*), EM_HI (*middle*) and 2EM_HI (*bottom*)*

8.6. This effect is discussed in Appendix A.3, and is found to be negligible.

8.3.2 QCD Fake Background Spectrum

The QCD fake background spectrum is determined using a di-EM sample. Events passing the 2EM_HI trigger are used. We select events having at least two EM objects with $E_T > 25$ GeV, located in either the CC or the EC fiducial region, and at least one in CC. If in one event more than two EM objects pass above kinematic and geometric cuts, all possible combination pairs are used.

Since the cross section for multijet processes is several orders of magnitude larger than processes involving real electrons, this very loose di-EM sample is dominated by EM objects mis-reconstructed from jets. The contamination of real electrons is found to be 5% near the Z peak and negligible in the high mass range. The contribution of these real electrons to the spectrum is removed using the sideband technique[3] to re-estimate the number of events within the Z peak window.

The γ+jet contamination in this di-EM sample is roughly (using a method similar to the calculation of the direct photon contamination in the single-EM sample):

$$\frac{N_{\gamma jet}}{N_{dijet}} = \frac{\sigma_{\gamma jet} \cdot P_{j\rightarrow em}}{\sigma_{dijet} \cdot P_{j\rightarrow em}^2}$$

The results are also listed in Table 8.2.

The spectrum expected from QCD fakes is obtained by plotting the distribution of invariant mass from this di-EM sample, with the contribution of an event equal to the probability that the event passes our selection cuts:

$$N_{QCD}\ (m) = \sum_{i=0}^{events\ (m)} W(i) \tag{8.7}$$

where $N_{QCD}\ (m)$ is the number of events in mass bin m (GeV) of the QCD fake background spectrum, the sum is over all events with invariant mass that falls in

[3]The number of QCD background in the 75-105 GeV window is approximately the number of QCD backgrounds in the windows of 60-75 GeV and 105-120 GeV. This is because the QCD background shape is nearly linear in this mass range.

mass bin m, and $W(i)$ is the probability that the ith event passes our selection cuts.

The probability can be computed as

$$W = (1 - f_{\gamma jet})P(dijet \to e_l e_t) + f_{\gamma jet}P(\gamma jet \to e_l e_t) \tag{8.8}$$

where $f_{\gamma jet}$ is the fraction of γ+jet events, $P(dijet \to e_l e_t)$ is the probability that a dijet event passes our selection cuts, and $P(\gamma jet \to e_l e_t)$ is the probability that a γ+jet event passes our selection cuts. For dijet events, the probability is:

$$P(dijet \to e_l e_t) = P^1_{em\to e_l}\ P^2_{em\to e_t} + P^1_{em\to e_t}\ P^2_{em\to e_l} - P^1_{em\to e_t}\ P^2_{em\to e_t} \tag{8.9}$$

For γ+jet events, the probability is:

$$P(\gamma jet \to e_l e_t) = 0.5 \times \epsilon\ P^2_{em\to e_t} + 0.5 \times \epsilon\ P^1_{em\to e_t} \tag{8.10}$$

where $P^1_{em\to e_l(e_t)}$ and $P^2_{em\to e_l(e_t)}$ are the "loose" ("tight") fake rates for the first and the second EM objects respectively; ϵ are the identification efficiency for the direct photon. The 50% weight in Equation 8.10 is due to the fact that either EM object can be the direct photon. The fake rates are calculated by Equation 8.3-8.6. The identification efficiencies are measured in Section 7.2.2.

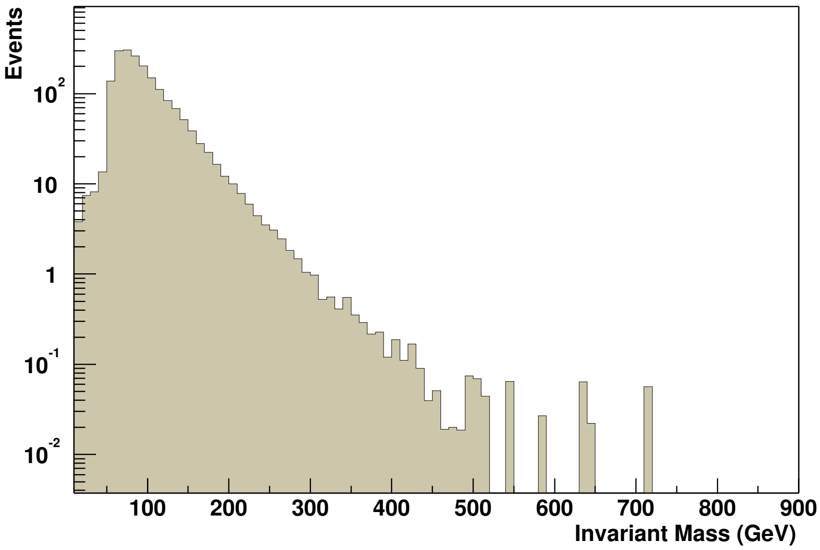

Figure 8.6: *Invariant mass spectrum of QCD fake background.*

Figure 8.6 shows the spectrum expected from the QCD fake background. Errors in the fake background are estimated to be 11.7% for the CCCC topology and 12.8% for the CCEC topology, obtained by varying the fake rates within their errors.

Chapter 9

Results

9.1 Observed Data vs. Expected Background

The mass range we are interested in is $M_{ee} > 150$ GeV. To calculate the amount of physics background and the amount of QCD fake background, we use a fit method in the Z peak region, where other backgrounds are negligible.

The mass distribution of the data, $N_{data}(m)$, is fit to the sum of the spectrum from physics processes, $N_{Phys}(m)$, and the spectrum from QCD fake, $N_{QCD}(m)$, within the Z peak region:

$$N_{data}(m) = c_1 \cdot N_{Phys}(m) + c_2 \cdot N_{QCD}(m)$$

where c_1 and c_2 are the normalization factors of the physics and QCD fake background spectrum respectively. These two factors are not independent since they must satisfy the constraint that, when integrated over the fit window, the total number of events in the data equals to the total number of events in the sum. This leaves us only one free parameter.

A binned χ^2 minimization fit is performed using the MINUIT package provided by the CERN ROOT library [64]. Since the QCD contamination in the CC-CC topology is different from that in the CC-EC topology, the fit is performed for the CC-CC and CC-EC types separately. The fit is performed in the mass window 60-130 GeV. The agreement is quite good, and the χ^2 per degree of freedom (χ^2/ndf) is 1.36 and 1.55 for CC-CC and CC-EC types respectively. Another fit in the 65-115 GeV mass window is also performed, and the difference is used to estimate the systematic error.

The result, expressed as the fraction of QCD fake background (f_{QCD}) in the data (60-130 GeV), is summarized in Table 9.1.

Event Type	f_{QCD}	fit error (relative)	systematic error (relative)
CC-CC	0.056	14.7%	4.4%
CC-EC	0.091	10.2%	10.5%

Table 9.1: *Summary of fit results*

Figure 9.1 shows a comparison of the data and the expected background for

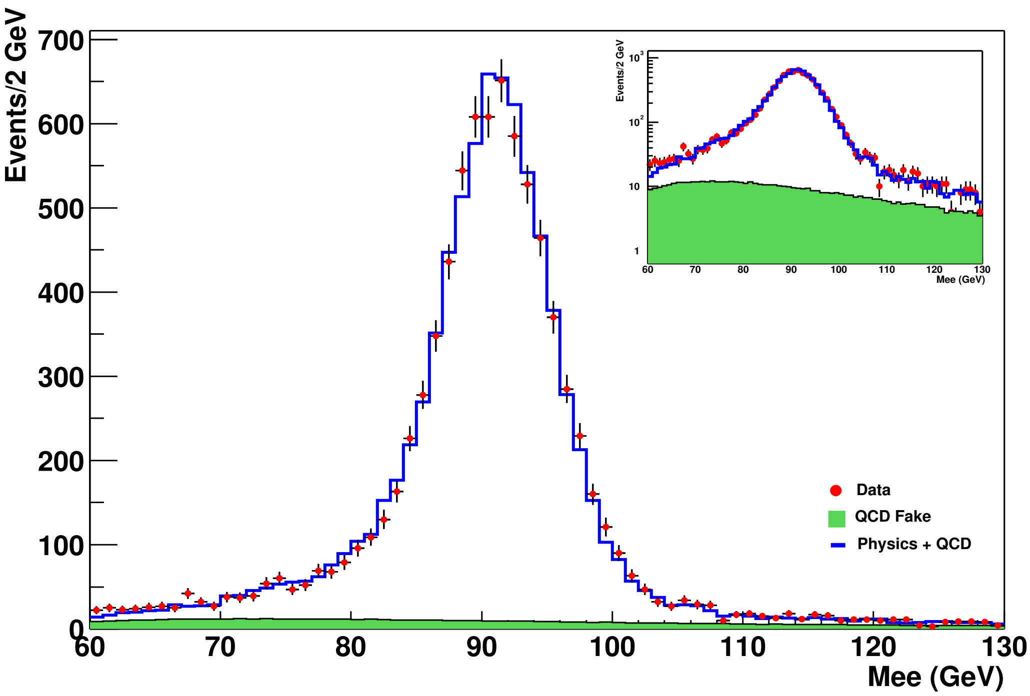

Figure 9.1: *The invariant mass distribution of data (*points*) and expected background (*line*) for the Z peak region. The shading represents the QCD fake background. The insert is the same plot in log scale.*

the Z peak region. Figure 9.2 shows a comparison of the data and the expected background for the entire mass range. Figure 9.3 shows the integrated mass spectrum of the data and that of the expected background, i.e. at each mass value, the vertical axis corresponds to the total number of events with M_{ee} above that mass. In Table 9.2, we compare the observed number of events with Standard Model expectations for different mass regions. The data agree well with the background expectations from the Standard Model.

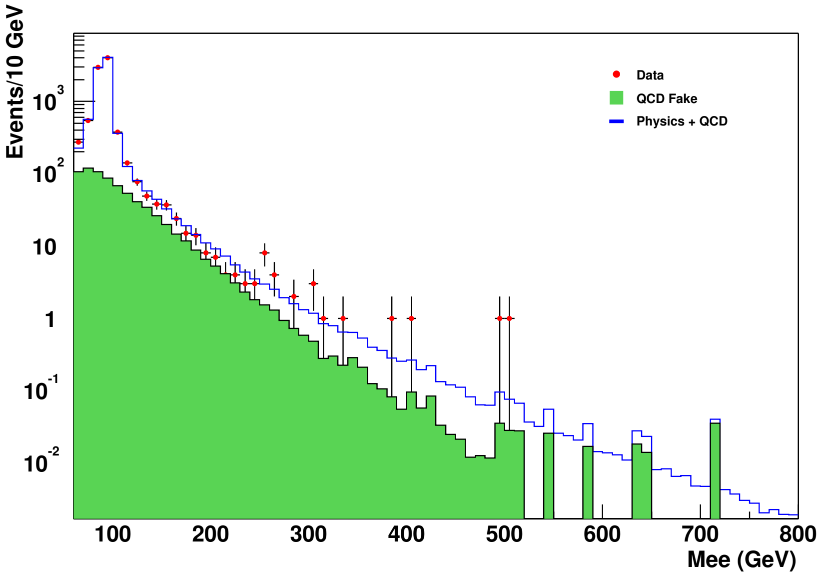

Figure 9.2: *The invariant mass distribution of data* (points) *and expected background (the line is the Physics+QCD background, whereas the shaded region is for the QCD fake background alone).*

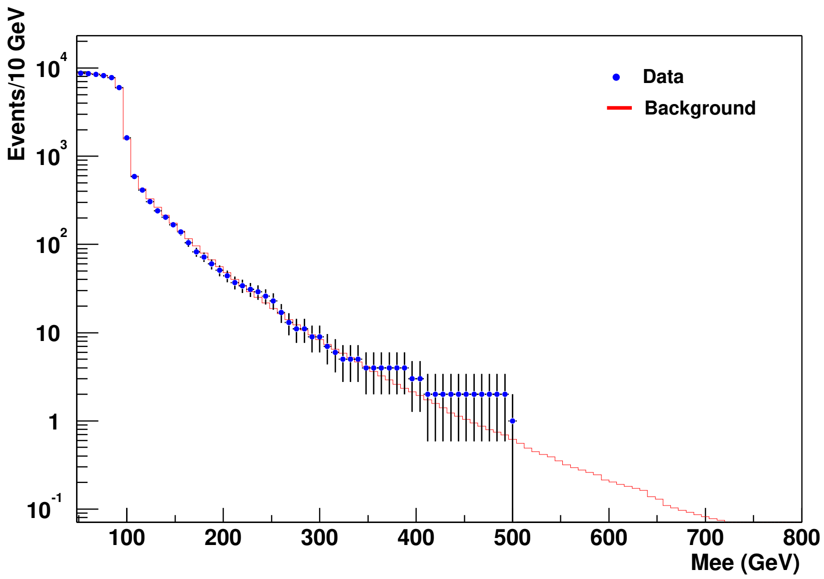

Figure 9.3: *The integrated spectrum of data* (points) *and the expected background* (line)*. At each mass value, the vertical axis corresponds to the total number of events with M_{ee} above that mass.*

mass (GeV)	expected	observed
150-200	101 ± 11	98
200-300	40 ± 4	35
300-400	5.9 ± 0.4	6
400-500	1.3 ± 0.1	2
500-700	0.51 ± 0.04	1
700-1000	0.08 ± 0.01	0

Table 9.2: *Comparison of observed and expected number of events.*

9.2 Z Cross Section Measurement

The number of Z events is obtained by subtracting the QCD fake background and the contribution from other physics processes from the data in a mass window of 75-105 GeV. However, this number also includes the contribution of events from the Drell-Yan ($|\mathcal{M}_{\gamma^*}|^2$) and interference ($|\mathcal{M}_{z-\gamma^*}|^2$) terms. The fraction of events contributed by those terms is estimated using PYTHIA to be $1.2\% \pm 0.1\%$ [59].

After removing contributions from the Drell-Yan and interference terms, the total number of pure Z events observed is

$$N_Z = 7133 \ \pm 76 \ (stat) \ \pm 39 \ (sys) \tag{9.1}$$

As a cross check, we estimate the cross section times branching ratio for the $Z \to ee$ process:

$$(\sigma B)_Z = \frac{N_Z}{\mathcal{L} \cdot \epsilon_{\mathcal{Z}}} \tag{9.2}$$

where $\mathcal{L}$ is the total luminosity and ϵ_Z is the overall efficiency calculated in Section 7.3.

The measured cross section is

$$(\sigma B)_Z = 249 \ \pm 28 \ pb$$

The error arises from errors in luminosity (10%), the measured efficiency and acceptance (5.5%), and errors in N_Z (1.2%).

The number of Z events and the cross section for the two different topologies is

CCCC:	$N_Z = 4059 \ \pm 23 \ (sys) \ \pm 57 \ (stat)$	$(\sigma B)_Z = 248 \ \pm 27 \ pb$
CCEC:	$N_Z = 3074 \ \pm 32 \ (sys) \ \pm 49 \ (stat)$	$(\sigma B)_Z = 249 \ \pm 29 \ pb$

The measured cross section is consistent with the theoretical expectation (252 ± 9 pb) [65].

9.3 Extracting A Limit

We do not see any significant excess of events in the dielectron mass spectrum, which would be expected from the decay of a narrow resonance like the Z'. In the absence of a Z' signal, we set an upper limit on the product of the cross section times branching ratio as a function of Z' mass.

9.3.1 Uncertainties

Instead of calculating $(\sigma B)_{Z'}$, we set an upper limit on the ratio $(\sigma B)_{Z'}/(\sigma B)_Z$ at the 95% confidence level (CL). By placing an upper limit on the ratio, many systematic uncertainties in the efficiency and luminosity measurements cancel. The systematic uncertainty on the luminosity completely cancels.

The following uncertainties are taken into account in the limit calculation by assuming a Gaussian smearing in the probability function.

- δN_Z: The systematic and statistical uncertainties (added in quadrature) in the observed number of Z events.

- δb: The uncertainty in the number of the expected background. For both the QCD fake background and the physics background, this includes the fit error and systematic error in the fit (Section 9.1). The uncertainty on the QCD background also includes the uncertainty due to the fake rate error (see the end of Section 8.3.2). The uncertainty on the Z/Drell-Yan background also includes the uncertainty due to the uncertainty in the K-factor (Section 8.1).

- $\delta\frac{\epsilon_{Z'}}{\epsilon_Z}$: The uncertainty in the ratio of overall efficiency for Z' and Z events. It includes the errors in the selection efficiencies and uncertainties in the acceptances from various sources (Section 7.3).

9.3.2 Binned Likelihood Method

A binned likelihood approach using Poisson statistics was applied to calculate the limit. The procedure is the same as described in [66].

The probability that n_i events will be experimentally observed in the ith bin is given by:

$$P_i = \frac{(\mu_i)^{n_i} e^{-\mu_i}}{n_i!}$$

where μ_i is the number of predicted events in ith bin. The total probability is then given by:

$$P = \prod_{i=1}^{N} \frac{(\mu_i)^{n_i} e^{-\mu_i}}{n_i!} \tag{9.3}$$

where N is the total number of bins. If we define:

$$\rho \equiv \frac{(\sigma B)_{Z'}}{(\sigma B)_Z} = \frac{\epsilon_Z}{\epsilon_{Z'} N_Z} N_{Z'}$$

then the predicted number of events in ith bin can be expressed as:

$$\mu_i = f_i \cdot (\frac{\epsilon_{Z'}}{\epsilon_Z}) \cdot N_Z \cdot \rho + b_i \tag{9.4}$$

where

f_i: fraction of total Z' events in ith bin

$\epsilon_{Z'}/\epsilon_Z$: efficiency ratio of $Z' \to ee$ and $Z \to ee$ events

N_Z: number of Z events observed

b_i: number of background expected in ith bin

The uncertainty in $\epsilon_{Z'}/\epsilon_Z$, N_Z and b_i can be incorporated into the probability distribution by assuming a Gaussian distribution. The final probability distribution is then given by:

$$P(\rho) = \frac{1}{A}\int_0^\infty d(\frac{\epsilon_{Z'}}{\epsilon_Z})' \int_0^\infty dN'_Z \int_0^\infty db'_i \prod_{i=1}^{N} \left[\frac{(\mu'_i)^{n_i} e^{-\mu'_i}}{n_i!}\; Gaus(b_i, \delta b_i)\right] Gaus(N_Z, \delta N_Z)\; Gaus(\frac{\epsilon_{Z'}}{\epsilon_Z}, \delta\frac{\epsilon_{Z'}}{\epsilon_Z}) \quad (9.5)$$

where

$$\begin{aligned} \mu'_i &= f_i \cdot (\frac{\epsilon_{Z'}}{\epsilon_Z})' \cdot N'_Z \cdot \rho + b'_i \\ Gaus(b_i, \delta b_i) &= e^{-\frac{1}{2}\left[\frac{b'_i - b_i}{\delta b_i}\right]^2} \\ Gaus(N_Z, \delta N_Z) &= e^{-\frac{1}{2}\left[\frac{N'_Z - N_Z}{\delta N_Z}\right]^2} \\ Gaus(\frac{\epsilon_{Z'}}{\epsilon_Z}, \delta\frac{\epsilon_{Z'}}{\epsilon_Z}) &= e^{-\frac{1}{2}\left[\frac{(\frac{\epsilon_{Z'}}{\epsilon_Z})' - (\frac{\epsilon_{Z'}}{\epsilon_Z})}{\delta\frac{\epsilon_{Z'}}{\epsilon_Z}}\right]^2} \end{aligned}$$

and A is the normalization constant such that:

$$\int_0^\infty P(\rho) = 1$$

The 95% CL limit on the $(\sigma B)_{Z'}/(\sigma B)_Z$, $\rho_{0.95}$, is obtained by solving:

$$\int_0^{\rho_{0.95}} P(\rho) = 0.95 \tag{9.6}$$

The program to calculate the limit can be found in [67]. Ten bins are used for the mass range 150-1000 GeV. The binning is chosen so that the number of expected Z' events is approximately equal in each bin [66].

9.3.3 Bayesian Technique

As an alternative limit calculation method, we use the Bayesian approach. The Bayesian technique is described in detail in [68]. The program used to perform the calculation can be found in [69].

The probability of observing k events in the 5σ mass window around the Z' peak is:

$$P(k|\mu) = \frac{(\mu)^k e^{-\mu}}{k!} \tag{9.7}$$

with

$$\mu = f \cdot (\frac{\epsilon_{Z'}}{\epsilon_Z}) \cdot N_Z \cdot \rho + b \tag{9.8}$$

where f, $\epsilon_{Z'}/\epsilon_Z$, N_Z, ρ and b are defined as before. The σ is the Z' peak width after detector smearing. Table 9.3 summarizes the 5σ mass window for Z' of various masses as well as the fraction of Z' events that lie within the window (f), the number of observed events and the expected background (b) in the window.

The inputs to the program are $f \cdot (\frac{\epsilon_{Z'}}{\epsilon_Z}) \cdot N_Z$, b and number of observed events for each Z' mass. Uncertainties are included in the limit calculation with Gaussian distributions.

$M_{Z'}$ (GeV)	5σ window (GeV)	f	#observed	#expected
300	220 - 380	0.933	29	30 ± 2.6
400	292 - 508	0.921	9	8.5 ± 0.65
500	364 - 636	0.906	4	3.0 ± 0.21
600	434 - 766	0.895	2	1.2 ± 0.088
700	510 - 890	0.865	0	0.51 ± 0.039
750	544 - 956	0.832	0	0.37 ± 0.028
800	581 - 1019	0.812	0	0.25 ± 0.019
900	652 - 1148	0.737	0	0.11 ± 0.010

Table 9.3: *The 5σ mass window for Z' of various masses, the fraction of Z' events that lie within the window (f), the number of observed events and the expected background (b) in the window.*

9.3.4 Limits

The 95% CL upper limit on the ratio $(\sigma B)_{Z'}/(\sigma B)_Z$ obtained by the two methods are summarized in Table 9.4 , together with the theoretical value of this ratio assuming standard model couplings. The theoretical cross section ratio is determined using Born level cross sections from PYTHIA, and is corrected for NNLO calculations using the K-factor. The cross sections reported by PYTHIA (with CTEQ4L pdf) and the K-factors used are also listed in Table 9.4. We use the same K-factors for the Drell-Yan process (Section 8.1) since we assume that Z' has the same couplings as the standard model Z. There is a 5% uncertainty in the K-factor due to parton distribution function.

Z' mass (GeV)	σB (pb) (PYTHIA)	K-factor	$(\sigma B)_{Z'}/(\sigma B)_Z$ theoretical	95% CL Binned Likelihood	95% CL Bayesian
300	3.442E+00	1.237	0.01991	0.000865	0.000972
400	1.061E+00	1.270	0.006301	0.000510	0.000538
500	3.632E-01	1.308	0.002221	0.000548	0.000394
600	1.354E-01	1.352	0.0008560	0.000323	0.000284
700	5.179E-02	1.403	0.0003398	0.000266	0.000262
750	3.146E-02	1.431	0.0002514	0.000273	0.000272
800	1.995E-02	1.461	0.0001363	0.000277	0.000280
900	7.798E-03	1.527	5.568e-05	0.000289	0.000314
Z	1.791E+02	1.194	—	—	—

Table 9.4: *Theoretical cross sections from PYTHIA, K-factors, and measured cross section upper limit at 95% CL.*

The 95% CL upper limit on the ratio $(\sigma B)_{Z'}/(\sigma B)_Z$ obtained by the two methods are also plotted as a function of the Z' mass in Figure 9.4, together with the theoretical value of this ratio assuming standard model couplings. The theoretical values with the Z' K-factors varying by $\pm 5\%$ are also plotted.

The two limit calculation methods give very similar results at the sensitive mass range. The "bump" at 500 GeV in the binned likelihood limit (Figure 9.4) is due to the 2 observed events around 500 GeV (mass is 495.0 GeV and 502.0 GeV respectively). 10 bins are used in the binned likelihood limit, so the bin size is very small. In the two bins around 500 GeV, $\sim$0.1 events are expected but 1 event is observed in each bin. This excess increases the upper limit. In the Bayesian limit, one large bin is used. The expected number of events is $\sim$3.0 and 4 events observed including the 2 events around 500 GeV. The binned likelihood method reflects every bin's agreement or excess. Its limit is, generally, more conservative. The limit from the Bayesian technique at very high mass (800 and 900 GeV) tends to increase slightly because the fraction of Z' events that lie within the 5σ window (i.e. f in Table 9.4) decreases due to non-Gaussian smearing from final state radiation.

The binned likelihood method excludes a Z' of mass $< 724\ ^{+5}_{-5}$ GeV. The Bayesian technique excludes a Z' of mass $< 725\ ^{+5}_{-5}$ GeV. As a conservative approach, a Z' with the same couplings to quarks and leptons as the standard model Z is excluded at the 95% CL for $m_{Z'} < 719$ GeV.

The upper limit on $\sigma B(Z' \to ee)/\sigma B(Z \to ee)$ is model independent. However, for any realistic Z' models, the mass limit would be less, because their cross sections are generally smaller [70].

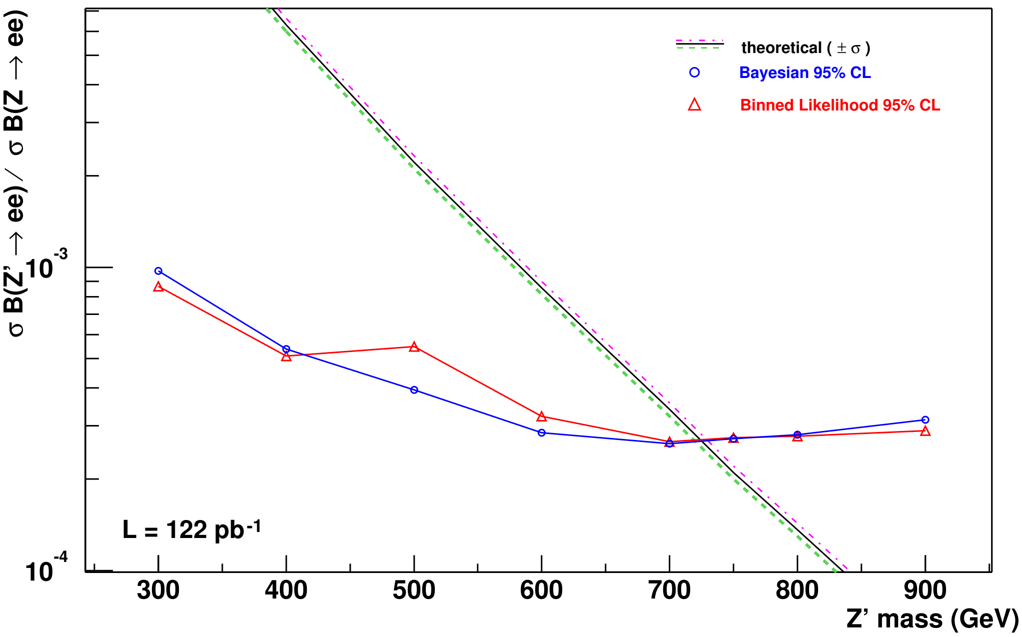

Figure 9.4: *95% CL limit as a function of $m_{Z'}$ for $(\sigma B)_{Z'}/(\sigma B)_Z$ as well as the theoretical value.*

Chapter 10

Conclusion

We have searched for evidence of $p\bar{p} \to Z' \to ee$ using data collected with the DØ detector in the Tevatron $p\bar{p}$ collisions at $\sqrt{s} = 1.96$ TeV during 2002-2003. We find that the observed number of events is consistent with the Standard Model prediction. We see no evidence of a Z' signal. We set an upper limit on the ratio $\sigma B(Z' \to ee)/\sigma B(Z \to ee)$ to be $\approx 3 \times 10^{-4}$, independent of theoretical models. We exclude the existence of a Z' of mass less than 719 GeV at the 95% confidence level, assuming it has same couplings to quarks and leptons as the Standard Model Z.

Appendix A

A.1 Brief History on the Direct Search for Z'

In Table A.1, we summarizes the brief history of Z' limits through direct searches including most recent conference results. Searches are based on the Tevatron $p\bar{p}$ collisions at $\sqrt{s} = 1.8$ TeV (Run 0 and Run I) and 1.96 TeV (Run II).

Year and Run	Exp.	Luminosity	Limit	Channel	Reference
1988-89 (Run 0)	CDF	3.5 pb^{-1}	412 GeV	ee+$\mu\mu$	PRL (1992) [20]
1992-93 (Run Ia)	CDF	19.7 pb^{-1}	505 GeV	ee	PR (1995) [21]
1992-93 (Run Ia)	DØ	15 pb^{-1}	490 GeV	ee	PL (1996) [18]
1992-95 (Run I)	CDF	110 pb^{-1}	690 GeV	ee+$\mu\mu$	PRL (1997) [22]
1992-96 (Run I)	DØ	124.8 pb^{-1}	670 GeV	ee	PRL (2001) [19]
2002-03 (RunIIa)	DØ	50 pb^{-1}	620 GeV	ee	Moriond 2003 [71]
2002-03 (RunIIa)	CDF	72 pb^{-1}	650 GeV	ee	Moriond 2003 [72]
2002-03 (RunIIa)	DØ	122 pb^{-1}	719 GeV	ee	LP 2003 [73]
2002-03 (RunIIa)	CDF	126 pb^{-1}	730 GeV	ee+$\mu\mu$	LP 2003 [73]

Table A.1: *Brief history on the Z' limits (95% CL) through direct searches*

A.2 Effect of a Higher Slope in HMx8

As discussed in Section 6.3.1, for CC electrons, the distribution of HMx8 as a function of electron's energy from data has a slightly higher slope than that from Monte Carlo. The slope in data is found to be 0.030 ± 0.006 GeV^{-1}, whereas the slope from Monte Carlo is 0.023 ± 0.002 GeV^{-1}.

To estimate the effect of a higher slope in HMx8 for CC. We now use 0.030 instead of 0.023 as the slope in the HMx8 cut for CC electron selection:

$$\text{HMx8 } \chi^2 < 20 + slope \times (E_T - 45\ GeV)$$

The slope for EC electron selection does not change.

Its effect on the efficiency of Z' signals is found to be negligible. For a Z' of 700 GeV, the difference in the efficiency between using this new cut and using the previous cut is found to be 0.7% (relative).

Further, the analysis is redone with this new cut from the event selection stage. This has two consequences.

On the background side, the fake rate for a "loose" CC electron changes from

$$P^{CC}_{em \to e_l}\ (E_T) = (0.230\ \pm\ 0.006) + (0.00040\ \pm\ 0.00017) \cdot E_T$$

to

$$P^{CC}_{em \to e_l}\ (E_T) = (0.230\ \pm\ 0.006) + (0.00045\ \pm\ 0.00017) \cdot E_T$$

There is a 12% increase in the slope. No significant changes are observed in the

	Cut used in the analysis		Cut with a higher slope	
mass (GeV)	expected	observed	expected	observed
150-200	101 ± 11	98	101 ± 11	99
200-300	39.9 ± 3.8	35	39.7 ± 3.8	36
300-400	5.90 ± 0.45	6	5.78 ± 0.44	7
400-500	1.301 ± 0.098	2	1.285 ± 0.093	2
500-700	0.508 ± 0.037	1	0.466 ± 0.035	1
700-1000	0.080 ± 0.008	0	0.058 ± 0.005	0

Table A.2: *Observed and expected number of events using the two cuts.*

fake rate for a "tight" CC electron. As a result, the QCD background slightly changes.

On the observed data side, the total number of events that pass the selection cuts is now 8735. There are 3 more events with mass $>$ 150 GeV (183 GeV, 294 GeV and 329 GeV). However, the number of events with mass $<$ 150 GeV decreases by 9 events[1].

In Table A.2, we summarized the number of observed events and expected background using this relaxed cut as well as numbers using previous cut. The measured 95% CL upper limit on $(\sigma B)_{Z'}/(\sigma B)_Z$ changes from 0.00266 to 0.00268, and the 95% CL mass limit changes less than 1 GeV.

[1]This is because the new cut is looser for $E_T > 45$ GeV electrons but tighter for $E_T < 45$ GeV electrons. In fact, the removed events are from QCD fake since the number of Z events is found to be the same as before.

A.3 Effect of Fake Rate Extrapolation

Due to the lack of statistics (Figure 8.4), the value of fake rate at high E_T (e.g. $E_T > 120$ GeV) is determined by the extrapolation given by Equation 8.3-8.6. If the real fake rate at high E_T is not as we determined, the number of background events in the limit sensitive mass range (550-850 GeV) will be different. This effect is estimated in the following 2 cases:

Case 1: if the fake rate at the interesting mass range is higher than extrapolated. Then, we expect more background in that range. Given that no events are observed, we will set a higher mass limit, which makes our current result more conservative.

Case 2: if the fake rate at the interesting mass range is smaller. We estimate this case by assuming the fake rate is flat after 100 GeV. The analysis is redone with this new QCD background. The mass limit changes about 0.4 GeV. The reason is that, at high mass range, the expected background is dominated by the physics background.

Bibliography

[1] National Research Council, *Physics through the 1990s: Elementary-Particle Physics,* Washington D.C., 1986.

[2] M.Y. Han, *Quarks and Gluons: a century of Particle Charges,* World Scientific, 1999.

[3] Donarld H. Perkins, *Introduction to High Energy Physics (3rd edition),* Addison-Wesley, 1986.

[4] Particle data Group, *Review of Particle Physics,* Springer, 2000.

[5] E. Abers and B.W. Lee, *Phys. Rep.* **C9**, 1 (1973);

C.N.Yang and T.D.Lee, *Phys. Rev.* **96**, 191 (1954).

[6] D. Griffiths, *Introduction to Elementary Particle Physics, pp.213-256,* John Wiley & Sons, 1987.

[7] S. Glashow, *Nucl. Phys.* **22**, 579 (1967);
S. Weinberg, *Phys. Lett.* **12**, 132 (1967);
A. Salam, *Elementary Particle Physics,* N. Svartholm ed., 367 (1968).

[8] H. Fritzsch and M. Gell-Mann, *in the Proceedings of the Sixteenth international Conference on High Energy Physics,* **Vol.2**, p.135, Chicago, 1972;
S. Weinberg, *Phys. Rev. Lett.* **31**, 494 (1973);
D.J. Gross and F. Wilczek, *Phys. Rev.* **D8**, 3633 (1973);
H. Fritzsch, M. Gell-Mann and H. Leutwyler, *Phys.Lett.* **47B**, 365 (1973).

[9] T. Hambye and K. Riesselmann, *Phys. Rev.* **D55**, 7255 (1997).

[10] P. Langacker, R.W. Robinett and J.L. Rosner, *Phys. Rev.* **D30**, 1470 (1984).

[11] J. C. Pati and A. Salam, *Phys. Rev. Lett.* **31**, 661 (1973);
R. N. Mohapatra, *Phys. Rev.* **D11**, 2558 (1975);
G. Senjanovic and R. N. Mohapatra, *Phys. Rev.* **D12**, 1502 (1975).

[12] G. Ross, *Grand Unified Theories,* Benjamin-Cummings Pub.Co., 1995.

[13] J.L. Hewett and T.G. Rizzo, *Phys. Rep.* **183**, 193 (1989).

[14] R.N. Mohapatra, *Unification and Supersymmetry,* Springer, 1992.

[15] Y.A. Gol'fand and E.P. Likhtam, *JETP Lett.* **13**, 323 (1971);
D.V. Volkov and V.P. Akulov, *Phys. Lett.* **B46**, 109 (1973);
J. Wess and B. Zumino, *Nucl. Phys.* **B70**, 39 (1974).

[16] G. Veneziano, *Nuovo Cim.* **A57**, 190 (1968);
J. Scherk and J. H. Schwarz, *Nucl. Phys.* **B81**, 118 (1974); *Phys. Lett.* **B57**, 463 (1975);
F. Gliozzi, J. Scherk and D. Olive, *Phys. Lett.* **B65**, 282 (1976).

[17] M. Cvetiĉ and S. Godfrey, *Discovery and Identification of Extra Gauge Bosons,* hep-ph/9504216, 1995.

[18] DØ Collaboration, *Phys. Lett.* **B385***,* 471 (1996).

[19] DØ Collaboration, *Phys. Rev. Lett.* **87***,* 061802 (2001).

[20] CDF Collaboration, *Phys. Rev. Lett.* **68***,* 1463 (1992).

[21] CDF Collaboration, *Phys. Rev.* **D51***,* 949 (1995).

[22] CDF Collaboration, *Phys. Rev. Lett.* **79***,* 2191 (1997).

[23] E. Ma, *Phys. Rev.* **D36***,* 274 (1987);
K.S. Babu *et al.*, *Phys. Rev.* **D36***,* 878 (1987).

[24] H.Georgi, E.Jenkins, and E.H.Simmons, *Phys. Rev. Lett.* **62**, 2789 (1989); *ibid* **63**, 1540 (1989)**E**; *Nucl. Phys.* **B331**, 541 (1990).

[25] R. Casalbuoni, S. de Curtis, D. Dominici, and R. Gatto, *Phys. Lett.* **B155**, 95 (1985); *Nucl. Phys.* **B282**, 235 (1987); *Nucl. Phys.* **B310**, 181 (1988).

[26] B. Schrempp, *Proceedings of the 23rd International Conference on High Energy Physics,Berkley,* World Scientific, 1987;
U. Baur *et al.*, *Phys. Rev.* **D35**, 297 (1987);
M. Kuroda *et al.*, *Nucl. Phys.* **B261**, 432 (1985).

[27] J. Erler, P. Langacker, *Phys. Lett.* **B456**, 68 (1999).

[28] For the review and original papers of these limits, see:
Particle Data Group, *"Review of Particle Physics", page 328, Phys. Rev.* **D66**, 010001 (2002).

[29] J. Thompson, *"Introduction to Colliding Beams at Fermilab",* Fermilab-TM-1909 (1994);
Fermilab Beam Division, *Run II Handbook,* http://www-bd.fnal.gov/runII .

[30] DØ Collaboration, *Nucl. Instr. Meth.* **A338**, 185 (1994).

[31] DØ Collaboration, *"DØ Upgrade: the Detector and its Physics",* Fermilab Pub-96/357-E.

[32] *"Conceptual Design of a 2 Tesla Superconducting Solenoid for the Fermilab DØ Detector Upgrade",* Fermilab TM-1886/DØ Note 2167.

[33] DØ Collaboration, *"The assembly and testing of the DØ silicon detector", 9th International Workshop on Vertex Detectors,* Michigan, Sep. 2000; *"DØ Silicon Tracker Technical Design Report",* DØ Note 2169.

[34] M. Narain (DØ Collaboration) *"A silicon track trigger for the DØ experiment", Nucl. Instrum. Mech.* **A447** *(pp. 223-234),* 2000.

[35] *"Central Fiber Tracker Technical Design Report",* DØ Note 4164.

[36] D. Adams *et al.*, *Nucl. Phys.* **B44**, 332 (1995); *IEEE Trans. Nucl. Sci., Vol 43, No.3,* 1146 (1996).

[37] *"Design Report of the Central Preshower Detector for the DØ Upgrade",* DØ Note 3014.

[38] *"The DØ Upgrade: Forward Preshower, Muon System and Level 2 Trigger",* DØ Note 2894.

[39] *"Technical Design Report for the Upgrade of the ICD for DØ Run II",* DØ Note 2686.

[40] *"Calorimeter Electronics Upgrade for Run 2",* http://www-d0.fnal.gov/~d0upgrad/calelec/intro/tdr/tdrformat.htm .

[41] Y. Arnoud, http://www-d0.fnal.gov/phys_id/emid/d0_private/minutes/20030409yannick.pdf .

[42] A. Cothenet, http://www-d0.fnal.gov/phys_id/emid/d0_private/minutes/20030129alexis.ps .

[43] S. Fatakia *et al.*, *"Jet Energy Scale and Resolution for p13 Data and Monte Carlo"*, http://www-d0.fnal.gov/phys_id/jes/d0_private/certified/v4.2/links.html

[44] A. Lo, C. Miao, R. Partridge, *"Luminosity Monitor Technical Design Report"*, DØ Note 3320.

[45] *"DØ Run II Level 1 Trigger Framework Technical Design Report"*, http://www.pa.msu.edu/hep/d0/ftp/l1/framework/l1fw_tdr_05june98.txt .

[46] *"Ethernet-based Data Acquisition for the DØ Experiment at Fermilab"*, http://d0.phys.washington.edu/~haas/d0/l3/sci2002.pdf .

[47] *"Description of DØ L3 Trigger Software"*, DØ Note 3266.

[48] D. Adams, *"Finding Tracks"*, DØ Note 2958-2.

[49] http://wwwd0.fnal.gov/trigger/stt/doc/svtstat_970307/svtbeam.html .

[50] M. Narain and F. Stichelbaut, *"Vertex Reconstruction using the Impact Parameters Technique"*, DØ Note 3560 (1999).

[51] Private communication, Dean Schamberger, State University of New York, Stony Brook.

[52] N. Hadley, *"Cone Algorithm for Jet Finding"*, DØ Note 904 (1989).

[53] L. Duflot and M. Ridel, *"The CellNN algorithm: cell level clustering in the DØ calorimeter"*, DØ Note 3923 (2001).

[54] T. Sjőstrand, L. Lőnnblad, S. Mrenna and P. Skands, *PYTHIA 6.206,* hep-ph/0108264.

[55] http://www-d0.fnal.gov/d0dist/dist/releases/test/d0gstar/docs/html /d0gstar.html;
http://www-d0.fnal.gov/computing/MonteCarlo/simulation/d0sim.html .

[56] F. Carminati et al, *"GEANT Users Guide"*, CERN Program Library, 1991.

[57] Junjie Zhu, *"Status of PMCS_EM"*, DØ Note 4062 (2002).

[58] http://consult.cern.ch/writeup/pdflib/ .

[59] J.N. Tarazi, *A Measurement of the Cross Section Ratio of the W and Z Electronic Decays and the Total Width of the W with the Dzero Detector (thesis),* http://www-d0.fnal.gov/results/publications_talks/thesis/tarazi/thesis_final _2side.ps .

[60] Junjie Zhu, *"EM Certification Tools" (Version 2.0),* DØ Note 4171 (2003).

[61] R. Hamberg, W.L. Van Neerven and T. Matsuura, *Nucl. Phys.* **B359**, 343 (1991).

[62] A.Gupta, N.K. Mondal, A.Kotwal, *Search for Quark and Lepton Compositeness using the Drell-Yan Cross Section at High Dielectron Invariant Mass,* DØ Note 3285 (1998).

[63] http://www-d0.fnal.gov/phys_id/emid/d0_private/minutes/20030312tuan.ppt .

[64] http://root.cern.ch/root/html/TMinuit.html .

[65] T. Wyatt, *"Electroweak Measurements from Run II at the Tevatron",* http://conferences .fnal.gov/lp2003/program/S1/wyatt_s01_updated.ppt .

[66] DØ Collaboration, *Phys. Lett.* **B358**, 405 (1995);
G. Eppley and P. Yepes, DØ Note 2540 (1995).

[67] http://www-d0.fnal.gov/~mcgao/limit_calculate/ .

[68] I. Bertram, G. Landsberg, J. Linnemann, R. Partridge, M. Paterno and H.B. Prosper, *"A Recipe for the Construction of Confidence Limits",* DØ Note 2775, 1995.

[69] Code from Greg Landsberg.

[70] P. Langacker and M. Luo, *Phys. Rev.* **D45**, 278 (1992).

[71] *The XXXVIII Rencontres de Moriond, Electroweak Interactions and Unified Theories, Les Arcs, March 15-22 2003.*

http://moriond.in2p3.fr/EW/2003/Transparencies/6_Friday/6_1_morning/6_1_6_Diehl/T_Diehl.pdf .

[72] http://moriond.in2p3.fr/EW/2003/Transparencies/3_Tuesday/3_1_morning/3_1_7_Rolli/S_Rolli.pdf .

[73] *The XXI International Symposium on Lepton and Photon Interactions at High Energies, Fermilab, IL, August 11-16 2003,* http://conferences.fnal.gov/lp2003/program/S2/perez_s02.pdf .